



universität
wien

DISSERTATION

Titel der Dissertation

PDE Models of Field-Effect Sensors

Verfasser

Mag. Stefan Andreas Baumgartner

angestrebter akademischer Grad

Doktor der Naturwissenschaften (Dr. rer. nat.)

Wien, im September 2012

Studienkennzahl lt. Studienblatt: A 791 405

Dissertationsgebiet lt. Studienblatt: Mathematik

Betreuer: Privatdoz. DI Dr. Clemens Heitzinger

Kurzfassung

Die Verwendung von Nanodrähten als biologisch sensitive Feldeffekttransistoren und somit als markierungsfreie Sensoren birgt eine Reihe von vielversprechenden Anwendungen wie zum Beispiel die Detektion von DNA oder, wie kürzlich in Blut nachgewiesen, von Krankheitsmarkern. Doch trotz des enormen experimentellen Entwicklungsfortschrittes und dem Versuch diese Technologie massenproduktionstauglich zu machen, fehlt ein umfassendes quantitatives Verständnis, welches nur durch mathematische Modellierung und durch Simulationen erreicht werden kann. Das mathematische Modell muss dabei zweierlei Dinge berücksichtigen: Den Aufbau solcher Sensoren und das Detektionsprinzip.

Der Aufbau besteht grundlegend aus einer nichtleitenden Schicht auf der der halbleitende Nanodraht aufgelegt ist. Der Nanodraht selbst ist wiederum mit einer nichtleitenden Schicht überzogen und der ganze Sensor ist einer wässrigen Lösung ausgesetzt, welche die zu detektierenden Moleküle enthält. Um alle geometrischen Eigenheiten des Sensors zu berücksichtigen muss das Modellierungsgebiet als dreidimensional angenommen werden. Die vorkommenden Materialien können dann mit einem System von partiellen Differentialgleichungen beschrieben werden. Dieses System ist auf der Poisson Gleichung aufgebaut und beinhaltet die Poisson-Boltzmann Gleichung und das Drift-Diffusion-Poisson System. Mit diesen Gleichungen können das elektrostatische Potential und die Ladungsträgerkonzentrationen selbstkonsistent berechnet und somit der Strom durch den Sensor bestimmt werden.

Das Detektionsprinzip und somit auch die Sensitivität des Sensors ist von dem, durch den Wechsel der Ladung in einer Grenzschicht, welcher durch die Bindung der zu detektierenden Moleküle an die an der Oberfläche befindlichen Moleküle zu Stande kommt, induzierten, Feldeffekt abhängig. Da diese Moleküle um einige Größenordnungen kleiner sind als die Gesamtgröße des Sensors würde eine herkömmliche Methode zur Lösung des Gleichungssystems, zum Beispiel die finite Volumen Methode, eine sehr feine Auflösung brauchen. Daher ist eine Multiskalenmethode angeraten welche nicht nur das Auflösungsproblem löst sondern gleichzeitig auch den Vorteil mit sich bringt, dass verschiedene Methoden zur Berechnung der Gegenionen in der Grenzschicht

verwendet werden können.

Nichtsdestotrotz ist das zu lösende lineare System, welches aus der finiten Volumen Methode resultiert, nach wie vor groß. Daher wurde eine Parallelisierungsmethode entwickelt. Parallelisierungsmethoden die auf dem FETI Algorithmus aufbauen haben den Vorteil, dass das Schnittstellenproblem durch Lagrange Multiplikatoren gelöst wird und somit die Sprungbedingungen der Multiskalenmethode in einer intuitiven Art implementiert werden können.

Abschließend kann dieses Model dazu benutzt werden, die Sensitivität in Abhängigkeit von geometrischen und physischen Eigenschaften zu optimieren. Um all diese Resultate zu zeigen wurden sie in die folgenden Kapitel gegliedert.

Diese Arbeit startet mit einer Einführung in Feldeffekttransistoren und der Modellierung von selbigen wobei vor allem auf Feldeffekttransistoren basierend auf Nanodrähten eingegangen wird. Das Modell trennt mithilfe einer Homogenisierungsmethode das für die Berechnung des Potentials und der Ladungsträger zu Grunde liegende Gebiet in die Grenzschicht und den übrigen Sensor auf. Weiters werden die drei am häufigsten benutzten Grenzschichtmodelle, das Drift-Diffusion-Poisson System und die Poisson-Boltzmann Gleichung für Flüssigkeiten besprochen. Am Ende des Kapitels wird das gesamte Modell zusammengefasst. Dieses einführende Kapitel basiert auf (Baumgartner et al., 2012b).

Im zweiten Kapitel ist die Existenz und lokale Eindeutigkeit einer Lösung des Modellsystems bewiesen. Dafür werden ein Satz von Rellich-Kondrachov über Kompaktheit, der Schauder Fixpunktsatz und ein Maximumprinzip verwendet. Dieses Kapitel basiert auf (Baumgartner and Heitzinger, 2012a).

Wie schon zuvor erwähnt wurde ein paralleler Simulator basierend auf der FETI Methode entwickelt. Der Algorithmus dieser Methode und dessen Herleitung sind im dritten Kapitel beschrieben. Weiters sind verschiedene Beispiele zur Verifizierung dieses Algorithmus gegeben. Dieses dritte Kapitel basiert auf (Baumgartner and Heitzinger, 2012b; Baumgartner et al., 2012a).

Das vierte Kapitel behandelt die optimale Sensitivität von zwei verschiedenen Sensoren. Dabei wird der Simulator mittels publizierten, gemessenen Strom-Spannungs Charakteristiken kalibriert und anschließend werden geometrische und physische Eigenschaften mit Rücksicht auf die Sensitivität optimiert. Dieses Kapitel basiert auf (Baumgartner et al., 2011a,b).

Das letzte Kapitel fasst diese Doktorarbeit zusammen.

Abstract

NANOWIRES used as biologically sensitive field-effect transistors (BioFETs) are promising label-free sensing devices with a wide range of applications, e.g., the detection of DNA or disease markers, recently even in whole blood. Despite the experimental progress in recent years and the push towards mass fabrication, quantitative understanding of the devices has been missing and hence mathematical modeling and simulation are crucial for physical understanding and optimal sensing. Therefore, a mathematical model has to include two major parts, the structure of such devices and the sensing mechanism.

The structure is based on a dielectric bulk layer carrying the semiconducting nanowire. The nanowire itself is covered by a second, thin dielectric layer. The whole dielectric surface is functionalized with probe molecules and is exposed to an aqueous solution containing the target molecules. To capture all geometry properties the model domain needs to be in 3d. The different materials are simulated by a system of partial differential equations based on the Poisson equation consisting of the Poisson-Boltzmann equation and the drift-diffusion-Poisson system. A solution of these equations exists and is locally unique around thermal equilibrium. The electrostatic potential and the charge densities are self-consistently computed and hence the current through the device is obtained.

The sensing mechanism and hence the sensitivity of the sensor is based on a field effect induced by a change of the boundary layer charge due to binding of target molecules to probe molecules. Since these molecules are some orders of magnitude smaller than the structure of the nanowire, a usual approach, such as the finite volume method, would need a very fine resolution. Hence a multiscale method is recommended which has the advantage that not only the resolution problem is avoided, it also makes it possible to use various methods for the computation of the concentration of counter ions in the boundary layer.

Nonetheless, the resulting linear problem, after discretization with the finite volume scheme, is still large and hence a parallelization technique has been developed. Parallelization techniques based on the FETI method have the advantage that the interface problem is solved by Lagrange

multipliers and hence the implementation of the jump conditions from the multiscale method is straightforward.

In the end, this model can be used to determine the optimal point of sensitivity regarding the geometry as well as the physical properties of such devices. To show all these results, they are arranged in chapters as follows.

This thesis starts with an introduction to field-effect transistors, especially nanowire field-effect transistors, and the modeling of these devices. The model splits the computation domain of the potential and the charges in the boundary layer and the remaining device using a homogenization method. Three main types of boundary layer models, the drift-diffusion-Poisson system, and the Poisson-Boltzmann equation for liquids are discussed. At the end of the introduction, the whole model is stated. This introductory chapter is based on (Baumgartner et al., 2012b).

In the second chapter, an existence and local uniqueness theorem for the model equations is proved. Therefore the Rellich-Kondrachov compactness theorem, the Schauder fixed-point theorem, and a maximum principle are used. This chapter is based on (Baumgartner and Heitzinger, 2012a).

As aforementioned, a parallelization simulator based on the FETI method has been developed. The algorithm of this method and its derivation is stated in chapter 3. Different examples are shown for the validation of this technique. This third chapter is based on (Baumgartner and Heitzinger, 2012b; Baumgartner et al., 2012a).

Optimal sensitivity for two different devices is shown in the fourth chapter. Therefore, the simulator is calibrated by published, measured current-voltage characteristics. After calibration, geometric properties as well as physical properties are optimized with respect to sensitivity. This chapter is based on (Baumgartner et al., 2011a,b).

The last chapter concludes this thesis.

Acknowledgment

FIRST AND FOREMOST I want to express my gratitude to my adviser *Dr. Clemens Heitzinger* for giving me the opportunity to work in his research group, to visit him and work with him at the University of Cambridge, and the chance to attend several scientific conferences. He delivered me insight into how research in applied mathematics work, how international publications should be written, and how things in the scientific world are handled. For me, he personates the role model of a researcher in the field of applied mathematics.

As I started with my PhD thesis, which is a continuation of my master thesis, I already worked 6 month together with *Alena Bulyha* on the simulation of BioFETs. With her I discussed the working principle of such sensors, how the mathematical model of such sensors should look, and about many programming issues. Our collaboration resulted in a publication in *Nanotechnology* which is one of the main results of this thesis. I want to thank her for our discussions and our collaboration.

After a year in my PhD thesis *Martin Vasicek* joined our research group who deeply influenced my scientific work. He proofread nearly all of my publications as well as conference contributions and was never parsimonious with critique which was sometimes hard to stand but improved my writing skills immensely. I want to thank him for the many hours proofreading my articles and to be a real friend.

In the last year of my PhD thesis *Gerhard Tulzer* joined our research group working on a differential equations model for the chemical reactions at the surface of a nanowire gas sensor. The working principle of nanowire gas sensors and nanowire BioFETs is similar and thus I enjoined to discuss with him the research regarding nanowire technologies and I hope I helped him with my understanding of these sensors. Thank you Gerhard for our discussions and our collaboration.

Every scientific work needs to have an environment where it can grow and hence I want to thank all people of the Wolfgang Pauli Institute and the Austrian Institute of Technology for giving me this place. To work at these institutions funding is needed and hence I also thank the

ACKNOWLEDGMENT

funding organizations. This work has been funded by the PhD program (Wissenschaftskolleg) "Differential Equation Models in Science and Engineering" from the Austrian Science Fund (FWF), by the project no. P20871-N13 from the Austrian Science Fund (FWF) and by the project no. MA09-028 by the Viennese Science and Technology Fund (WWTF).

Above all, I want to thank my family. My parents *Anton Baumgartner* and *Gertrude Baumgartner* made all of my studies possible by their continuous support.

Contents

Kurzfassung	i
Abstract	iii
Acknowledgment	v
Contents	vii
List of Symbols	xi
Notation	xi
Physical Quantities	xii
Constants	xii
List of Figures	xiii
1 Introduction	1
1.1 The Nanowire	3
1.2 The Sensing Mechanism	4
1.3 Homogenization	5
1.4 The Biofunctionalized Boundary Layer	8
1.4.1 The Site-Dissociation Model	9

1.4.2	Screening and Biomolecules	10
1.4.2.1	The Metropolis-Monte-Carlo Method	10
1.4.2.2	The Poisson-Boltzmann Equation	12
1.4.2.3	PROPKA	13
1.4.3	Gas Sensors	14
1.4.4	Comparison of Boundary-Layer Models	15
1.5	The Charge Transport in the Nanowire	15
1.5.1	The Drift-Diffusion-Poisson System	15
1.5.2	The Liquid	16
1.5.3	Self-Consistent Simulation of Sensor Systems	17
1.6	Summary	19
2	Analysis of the Model Equations Existence and Local Uniqueness	21
2.1	Slotboom Variables	22
2.2	Existence Theorem	23
2.3	Semilinear problems including interface conditions	24
2.4	Proof of the Existence Theorem 2.2.2	29
2.5	Local Uniqueness Theorem	32
2.6	Summary	36
3	A One Level FETI Method	39
3.1	Self-Consistent Loop	40
3.2	The FETI algorithm	41
3.3	The Algorithm	42
3.3.1	The Case of Two Subdomains	42
3.3.2	Schur Complement	43
3.3.3	A One-Level FETI Algorithm for the Drift-Diffusion-Poisson System with Discontinuities	45
3.4	Numerical Results	47
3.4.1	A Two-Dimensional Example	47
3.4.2	Two 3D Examples	50
3.4.2.1	A 3D Example – One Half of a Symmetric Device	50
3.4.2.2	A 3D Example – Whole Device	53

3.4.2.3	Condition Number Estimate	55
3.5	Summary	55
4	Simulation Results	57
4.1	DNA Sensor	57
4.1.1	The Boundary Layer Model	58
4.1.2	The Self-Consistent Loop	60
4.1.3	Simulator Calibration	61
4.1.4	Optimization of Device Parameters	62
4.2	PSA Sensor	65
4.2.1	Boundary Layer Model	65
4.2.1.1	Screening	65
4.2.2	Simulator Calibration	66
4.2.3	Sensitivity	69
4.3	Summary	73
5	Conclusion	75
A	Sobolev Spaces	77
B	Results from Functional Analysis	79
	Curriculum Vitae	91

List of Symbols

Notation

$\Omega, \Omega', \Omega''$...	Domain in \mathbb{R}^3
$\partial\Omega$...	Boundary of domain Ω
Γ	...	Hypersurface in \mathbb{R}^3
$S_r(\cdot)$...	Sphere with radius r and center \cdot
∂_ν	...	Partial derivative with respect to ν
∇	...	Nabla operator
$\nabla \cdot$...	Divergence operator
$D.$...	<i>Fréchet</i> derivative
$\text{meas}(\cdot)$...	<i>Lebesgue</i> measure
C^k	...	Set of functions having all derivatives of order $\leq k$ continuous
L^p	...	Set of equivalence classes of measurable functions that are p -integrable
H^k	...	Set of functions in L^2 having all weak derivatives up to order k in L^2
L^∞	...	Set of equivalence classes of measurable functions that are a.e. bounded
$H^{1/2}$...	Sobolev space of order $1/2$ (see Appendix A)
$\ \cdot\ _{L^p}$...	$(\int u ^p dx)^{1/p}$
$\ \cdot\ _{H^k}$...	$(\sum_{ \alpha =k} \int D^\alpha u ^2 dx)^{1/2}$
$\ \cdot\ _{L^\infty}$...	$\text{ess sup} u $
$\ \cdot\ _{H^{1/2}}$...	$(\ u\ _{L^2(\Omega)}^2 + \int_\Omega \int_\Omega \frac{ u(x)-u(y) ^2}{ x-y ^4} dx dy)^{1/2}$

LIST OF SYMBOLS

ker	...	Kernel of a matrix
†	...	Pseudoinverse of a matrix
⊥	...	Orthogonality

Physical Quantities

Symbol	Unit	Description
V	V	Electric potential
n	$\text{q} \cdot \text{cm}^{-3}$	Electron density
p	$\text{q} \cdot \text{cm}^{-3}$	Hole density
ε	$\text{F} \cdot \text{cm}^{-1}$	Permittivity
ζ	$\text{q} \cdot \text{cm}^{-1}$	Dipole-moment density
γ	$\text{q} \cdot \text{cm}^{-2}$	Surface-charge density
T	K	Temperature
C_{dop}	$\text{q} \cdot \text{cm}^{-3}$	Doping concentration
J_n	$\text{q} \cdot \text{cm}^2 \cdot \text{s}^{-1}$	Electron-current density
J_p	$\text{q} \cdot \text{cm}^2 \cdot \text{s}^{-1}$	Hole-current density
μ_n	$\text{V}^{-1} \cdot \text{cm}^2 \cdot \text{s}^{-1}$	Electron mobility
μ_p	$\text{V}^{-1} \cdot \text{cm}^2 \cdot \text{s}^{-1}$	Hole mobility
R	$\text{q} \cdot \text{cm}^3 \cdot \text{s}^{-1}$	Recombination rate
U_T	V	Thermal voltage
n_i	$\text{q} \cdot \text{cm}^{-3}$	Intrinsic charge concentration
τ_n	s	Electron lifetime
τ_p	s	Hole lifetime
ε_{liq}	$\text{F} \cdot \text{cm}^{-1}$	Permittivity of liquid
ε_{Si}	$\text{F} \cdot \text{cm}^{-1}$	Permittivity of Silicon
ε_{ox}	$\text{F} \cdot \text{cm}^{-1}$	Permittivity of Silicon Dioxide
η	$\text{mol} \cdot \text{cm}^{-3}$	Ionic concentration
ϕ	V	Fermi level

Constants

k_B	...	<i>Boltzmann's constant</i> ,	$1.3806503 \times 10^{-23} \text{ JK}^{-1}$
q	...	Elementary charge,	$1.6021892 \times 10^{-19} \text{ C}$
ε_0	...	Vacuum permittivity,	$8.8541878 \times 10^{-12} \text{ Fm}^{-1}$

List of Figures

1.1	Schematic diagram of an NWFET device.	3
1.2	Working principle of a conventional FET (top) and a nanowire field-effect sensor (bottom). In both cases, negative charge at the gate contact or at the nanowire surface leads to an increase of conductance due to accumulation of charge carriers in the semiconductor near the negative charges.	5
1.3	Schematic diagram of an NWFET, true to scale, with functionalized surface. The grid spacing on the left-hand side is $10\text{ nm} \times 10\text{ nm}$ and the detail on the right-hand side is 20 nm wide, 30 nm high, and is also true to scale. The depicted DNA is bound to the surface by a 1 nm long linker, is 5 nm high, and has a radius of 1 nm . The ions in the aqueous solution are modeled as charged hard spheres with a diameter of 0.3 nm	6
1.4	Schematic diagram of the electric potential V at the interface Γ in a cross section. The jump of size α of the electric potential is shown, while the jump of size β in the electric displacement results in a difference in the normal derivatives of the potential in Ω^- and Ω^+	7
1.5	The simulation domain of a constant-voltage Metropolis-Monte-Carlo simulation. Here it contains 2×2 biomolecules at the bottom of the cell. The molecules can be rotated with respect to the surface (Bulyha and Heitzinger, 2011).	11
1.6	Schematic diagram of the nanowire sensor; the different materials and the corresponding equations, used in the simulations, are indicated.	17

LIST OF FIGURES

1.7	On the left-hand side the boundary conditions for the electric potential are indicated. The potential satisfies Dirichlet conditions for Ohmic contacts at the source and at the drain as well as Dirichlet conditions for the applied voltage at the back-gate. Everywhere else, the potential at the boundary is described by Neumann conditions. For the drift-diffusion-Poisson system we need additional boundary conditions at the nanowire. The electron and hole concentrations satisfy Dirichlet conditions at the source and the drain. Everywhere else Neumann conditions hold.	18
3.1	2d simulation domain divided into 8 subdomains. In $\Omega_1, \Omega_2, \Omega_3,$ and $\Omega_4,$ the drift-diffusion-Poisson system holds and in $\Omega_5, \Omega_6, \Omega_7,$ and $\Omega_8,$ the Poisson equation holds. The interface is situated between the subdomains Ω_3 and Ω_4 on the one side and Ω_5 and Ω_6 on the other side. At the interface, jumps in the electric potential and the electric displacement occur. The boundary conditions are Dirichlet conditions.	48
3.2	(a) Electric potential in all 8 subdomains. (b) Electron density in the 4 subdomains where the drift-diffusion-Poisson system holds.	49
3.3	A cross section of the simulation domain with the 12 blocks of the FETI algorithm in the x - and y -directions. The interface is indicated as well.	50
3.4	Non-redundant connection of 8 blocks at the vertex $(20, 30, 10)$.	51
3.5	Electric potential V in the cross section $z = 10$ nm.	52
3.6	(a) Electric potential V in the cross section at $x = 5$. (b) Corresponding electron concentration n in the same cross section.	53
3.7	Actual speedup vs. ideal speedup of a 3d simulation.	53
3.8	Schematic diagram of the NWFET device. The different equations used in the simulations and the cross section $x = 15$ used in the remaining figures are indicated. The blocks for parallelization have a size of $10 \times 10 \times 10$ nm ³ (Fig. 2, 3) or $10 \times 10 \times 5$ nm ³ (Fig. 4, 5, 6).	54
3.9	Cross section of the electrostatic potential at $z = 10$.	54
3.10	Left: Cross section of the electrostatic potential at $y = 15$. Right: Cross section of the electrostatic potential at $x = 15$.	55
4.1	The simulation domain of a Monte-Carlo simulation. Here it contains 2×2 biomolecules.	58
4.2	Concentration profiles for a 1:1 electrolyte for no molecules, PNA, ssDNA, and dsDNA on a logarithmic scale as a function of distance from the surface (Baumgartner et al., 2011a).	59

4.3	Surface-charge density γ and dipole-moment density ζ as a function of applied voltage for no molecules and for 10-mers of PNA, ssDNA, and dsDNA. The angle of the oligomer is $\alpha = 45^\circ$ with respect to the surface, the surface-charge density is $\rho = -0.2 \text{ q/nm}^2$, the ionic bulk concentration is 0.01 M, and the applied potentials varies between -250 mV to 250 mV . The surface-charge and dipole-moment densities are of the same order of magnitude.	60
4.4	Current-voltage characteristics for an n-doped non-functionalized nanowire field-effect biosensor. The solid line corresponds to a back-gate voltage of 5 V, the dashed line to 4 V, and the dotted line to 3 V. The crosses are the corresponding measurements for a back-gate voltage of 5 V, the triangles for 4 V, and the circles for 3 V (Li et al., 2006).	62
4.5	Top left: The current change ΔI_{SD} is shown as a function of the length of the nanowire for three situations: the change from non-functionalized to dsDNA (top), the change from non-functionalized to ssDNA (middle), and the change from ssDNA to dsDNA (bottom). The back-gate voltages are 4 V and 5 V and the source/drain voltage is 0.5 V. Top right: The current change ΔI_{SD} is shown as a function of the gate voltage with the scale on the left-hand side for the same three situations as in Fig. 4.5. The source/drain current I_{SDG} (black, solid line) is shown as a function of the gate voltage as well with the scale on the right-hand side. The threshold voltage is indicated by a vertical black line. The source/drain voltage is 0.1 V. Bottom left: Current change ΔI_{SD} for gate voltages of 4 V and 5 V for the three situations non-functionalized/dsDNA, non-functionalized/ssDNA, and ssDNA/dsDNA as a function of the nanowire thickness. The source/drain voltage is 0.1 V. Bottom right: Current change from non-functionalized surface to dsDNA for gate voltages of 4 V and 5 V at a source/drain voltage of 0.5 V as a function of the doping concentration.	63
4.6	Electric potential and electron density in a cross section of the silicon nanowire at $z = 250 \text{ nm}$. The figures at the top correspond to a back-gate voltage of 4 V and the figures at the bottom correspond to a back-gate voltage of 5 V. The source/drain voltage is 0.1 V.	64
4.7	Left: Structure of protein 1EZK from the protein database (http://www.pdb.org/pdb/explore/explore.do?pdbId=1ezk) with primary citation (Huntington et al., 2000). Right: Charge of protein 1EZK calculated by PROPKA (http://propka.ki.ku.dk/) (see Section 1.4.2.3).	66
4.8	Schematic diagram of the NWFET-PSA sensor.	67

4.9	<p>Top left: Current-Voltage characteristic for an NWFET device with a 60 nm and a 100 nm wide nanowire with 8 nm top oxide and 50 nm high silicon. The hole mobility is $100 \text{ cm}^2\text{V}^{-1}\text{s}^{-1}$ and the thermal voltage is 0.021 V.</p> <p>Top right: Current-Voltage characteristic for an NWFET device with a 60 nm and a 100 nm wide nanowire with 14 nm top oxide and 50 nm high silicon. The hole mobility is $50 \text{ cm}^2\text{V}^{-1}\text{s}^{-1}$ and the thermal voltage is 0.023 V.</p> <p>Bottom left: Current-Voltage characteristic for an NWFET device with a 60 nm and a 100 nm wide nanowire with 8 nm top oxide and 40 nm high silicon. The hole mobility is $220 \text{ cm}^2\text{V}^{-1}\text{s}^{-1}$ and the thermal voltage is 0.021 V.</p> <p>Bottom right: Current-Voltage characteristic for an NWFET device with a 60 nm and a 100 nm wide nanowire with 14 nm top oxide and 40 nm high silicon. The hole mobility is $50 \text{ cm}^2\text{V}^{-1}\text{s}^{-1}$ and the thermal voltage is 0.023 V.</p>	68
4.10	<p>All subfigures: The sensitivity is shown for 60 nm, 80 nm, and 100 nm wide nanowires with surface charge $\gamma = -0.4 \text{ q} \cdot \text{nm}^{-2}$, $\gamma = -0.6 \text{ q} \cdot \text{nm}^{-2}$, and $\gamma = -0.8 \text{ q} \cdot \text{nm}^{-2}$. Measured values from an experiment are shown as well.</p> <p>Top left: Sensitivity of a sensor with the same configuration used in the top left of Fig. 4.9.</p> <p>Top right: Sensitivity of a sensor with the same configuration used in the top right of Fig. 4.9.</p> <p>Bottom left: Sensitivity of a sensor with the same configuration used in the bottom left of Fig. 4.9.</p> <p>Bottom right: Sensitivity of a sensor with the same configuration used in the bottom right of Fig. 4.9.</p>	70
4.11	<p>Top left: Sensitivity as a function of nanowire thickness for a 60 nm and 100 nm wide nanowire and gate voltages $V_G = -1 \text{ V}$, $V_G = -2 \text{ V}$, and $V_G = -3 \text{ V}$.</p> <p>Top right: Sensitivity as a function of nanowire width for a sensor with gate voltages of $V_G = -1 \text{ V}$, $V_G = -2 \text{ V}$, and $V_G = -3 \text{ V}$.</p> <p>Bottom left: Sensitivity as a function of nanowire length for a 60 nm and 100 nm wide nanowire and gate voltages $V_G = -1 \text{ V}$, $V_G = -2 \text{ V}$, and $V_G = -3 \text{ V}$.</p> <p>Bottom right: Sensitivity as a function of doping concentration for a 60 nm and 100 nm wide nanowire and gate voltages $V_G = -1 \text{ V}$, $V_G = -2 \text{ V}$, and $V_G = -3 \text{ V}$.</p>	71
4.12	<p>Top left: Sensitivity as a function of top oxide for a 60 nm and 100 nm wide nanowire and gate voltages $V_G = -1 \text{ V}$, $V_G = -2 \text{ V}$, and $V_G = -3 \text{ V}$.</p> <p>Top right: Sensitivity as a function of bulk oxide for a 60 nm and 100 nm wide nanowire and gate voltages $V_G = -1 \text{ V}$, $V_G = -2 \text{ V}$, and $V_G = -3 \text{ V}$.</p> <p>Bottom left: Sensitivity as a function of gate voltage for a 60 nm and 100 nm wide nanowire.</p> <p>Bottom right: Sensitivity as a function of drain-source voltage for a 60 nm and 100 nm wide nanowire and gate voltages $V_G = -1 \text{ V}$, $V_G = -2 \text{ V}$, and $V_G = -3 \text{ V}$.</p>	72

Chapter 1

Introduction

THE FIELD EFFECT and its use for the sensing of biomolecules has a long and exciting history. At the beginning of this history stands, as for every technology, an idea and so it was for the field-effect transistor (FET) as *Lilienfeld* applied for a patent in 1926. This patent describes that a poorly conducting material changes conductivity when a voltage is applied which is – in some sense – the main idea of today’s FET (Brinkman et al., 1997). Many ideas never become real but fortunately over a decade later, in the late 1940s, the digital revolution was initiated by the development of the first field-effect transistor in the Bell Labs, for which *Shockley*, *Bardeen*, and *Brattain* were jointly awarded the 1956 *Nobel Prize* in Physics. From this time onwards semiconductor transistors and microchips have deeply influenced human society and today we even could not imagine how a world without this versatile technology should look.

While the transistor became more and more popular another innovation came to life as *Clark* and *Lyons* invented the first biosensor for blood analysis in 1962 (Clark and Lyons, 1962). Probably due to the popularity of the FET it took only eight years till these two technologies merged to the first biosensors based on the field effect, the ion-sensitive field-effect transistors (ISFETs), introduced by *Bergveld* (Bergveld, 1970; Schöning and Poghossian, 2006). Therefore the classical FET configuration was only changed by replacing the upper electrode, which is responsible for the field-effect, by an aqueous solution containing charge carriers. The detailed description of the field-effect is given in Section 1.2.

The first property of such ISFET is that changes in pH value at the solution-insulator interface changes the conductance in the FET. Hence an ISFET can be used as a pH sensor which was first established in 1971 by *Matsuo* et al. (Janata, 2004). Also other ion species can be detected with ISFETs. Those ISFET are called chemically-sensitive field effect transistors (ChemFETs) (Janata, 1994). Moreover, every other electrical interaction at this interface leads to a change in the electrical response of the underlying semiconductor which makes the ISFET a versatile tool for the

detection of, e.g., ion concentrations, enzymatic reactions, cellular metabolism, action potentials of living cells, or other bioreceptors (Poghossian et al., 2007; Schöning and Poghossian, 2002).

The ISFETs using a bio-recognition element are termed biologically-modified field-effect transistors (BioFETs) which are, e.g., the enzyme-modified FET (EnFET) first realized in 1980, the immunologically modified FET (ImmunoFET) or the DNA-modified FET (DNAFET) (Schöning and Poghossian, 2002). It should be noted that these examples of sensors using the field effect have one thing in common which is crucial for the mathematical model – they are all based on a change of charges in a boundary layer near an interface.

Since the invention of the first ISFET, biosensor technologies flourished and are still of paramount interest today (Stern et al., 2010; Tian et al., 2010; Timko et al., 2010). Despite this huge experimental progress the theoretical understanding is still incomplete and hence mathematical and physical modeling is as important as it was for the transistor - the theoretical model from Shockley had an immense impact on its success.

The last ingredient for today's sensing devices which became very popular in the last decades is the nanotechnology and hence nanostructures. A nanostructure is a system where at least one dimension is smaller than 100 nm. These can be 2d layers, 1d nanowires, or 0d nanoclusters (Lieber, 1998). Using nanostructures, more than 40 years the transistors followed Moore's Law which states that every 24 month the number of transistors on a chip doubles (Chau et al., 2005). To reach this ambitious aim, the length of the transistor gate went down to less than 30 nm in the last years (Iwai, 2009; Palacios, 2012). However, it is quite doubtful that this trend can be maintained in future (Bohr et al., 2007). The transducers used in field-effect sensors have been influenced by this development, although the downsizing has not been done as much as for the transistor, and now many promising bio-sensing devices for medical and biotechnological applications are based on nanotechnology (Patolsky et al., 2006a,c; Stern et al., 2008).

Nowadays, we even have the choice which nanotechnology we want to use. The most promising sensing devices are based on nanowires and carbon nanotubes due to their high sensitivity, fast response, and direct electrical readout (Patolsky et al., 2006b). Still, questions of characterization, uniformity and manufacturability need to be addressed before nanoscale biosensors can be mass-produced and used in daily life. In the following we will look on some of these issues of carbon nanotubes and nanowires separately.

In the case of carbon-nanotube sensors, it has been reported that the adsorption of biomolecules, e.g., proteins, on a SWNT (single-walled carbon nanotube) results in a sufficient change of conductance for detection due to the field effect (Chen et al., 2003, 2004; Sorgenfrei et al., 2011). Nonetheless, some problems must be overcome before SWNTs can be used commercially as sensors. For example, the non-specific binding of molecules to the SWNT must be avoided due to the possible change of the dielectric constant of the electric double layer in the aqueous solution, which would cause an unwanted sensor response (Chen et al., 2004). However, for mass production silicon nanowires are more promising due to the dominant use of CMOS technology (Iwai, 2009). Hence we will restrict ourselves to devices based on nanowires in this thesis.

Much research on producing silicon nanowire based sensors has been conducted in recent years (Cui et al., 2000, 2001, 2003; Elfström et al., 2008; Gao et al., 2010; Hahm and Lieber, 2004; Li et al., 2006; Patolsky and Lieber, 2005; Patolsky et al., 2007; Stern et al., 2007a,b; Wang et al., 2005; Zheng et al., 2010, 2005) and today devices based on nanowires are the most likely future tool for the electrical detection of biological and chemical species ranging from proteins, DNA,

drug molecules, and viruses to single molecules (Patolsky et al., 2006c). Furthermore they are highly sensitive due to their high surface to volume ratio, are, as stated before, CMOS compatible due to their fabrication out of silicon, and sense without labeling. To get a better understanding of these devices, how they look, and which parts we need to cover with our simulations we give an overview on the fabrication of nanowires in the following.

1.1 The Nanowire

The production of nanowires and hence the production of nanowire devices can be classified in two categories, bottom up and top down. The most popular bottom-up technique is the vapour-liquid-solid (VLS) growth method (Cui et al., 2001; Hahn and Lieber, 2004; Lieber, 1998; Patolsky et al., 2006a; Wagner and Ellis, 1964). This process uses a catalyst nanoparticle to grow nanowires through absorption of a gas phase. The advantage of bottom-up methods over top-down methods is that incorporation of heterogeneities and dopings is easily done and that the size of the nanowire can be defined by the size of the catalyst nanoparticle.

When growing nanowires by the bottom-up technique, we usually get a lot of nanowires located somewhere at a substrate from which we have to pick a single nanowire. Then this nanowire is deposited on another substrate contacted by electrodes. This process is difficult to achieve with mass production techniques and each device has its unique properties. Hence reproducibility of devices produced by this method is hard to achieve, by now (Ginet et al., 2011; Stern et al., 2011).

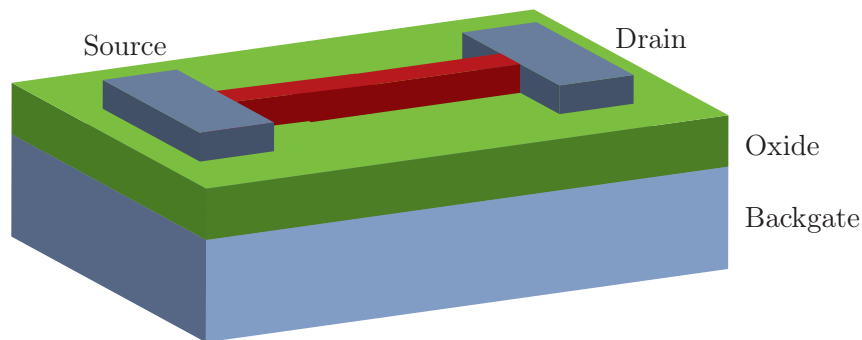


Figure 1.1: Schematic diagram of an NWFET device.

Using top-down methods, the placement step is not needed and hence reproducibility is improved. Currently the most used tools are the electron-beam (EBL), the focused ion beam (FIB) or the deep ultraviolet (DUV) lithography followed by anisotropic, dry or wet reactive ion etching (RIE). Recently, for the use of nanowires in sensor applications an anisotropic wet etch of silicon with tetramethylammonium hydroxide has been used (TMAH) (Ginet et al., 2011; Stern et al., 2007a, 2011). However, both methods have their applications and can be used for nanowire sensors with a design depicted in Fig. 1.1.

In this thesis we consider a general design. Here a silicon nanowire lies on an silicon dioxide substrate and has two electrical contacts at the source and the drain of the nanowire. A third

electric contact rests under the silicon dioxide. The nanowire is separated from the aqueous solution by a thin silicon dioxide layer. This layer is functionalized with receptor molecules, e.g., proteins or antibodies, on which a corresponding ligand, if present in the aqueous solution, binds. How this binding is measured by the nanowire BioFET is explained in the following section.

1.2 The Sensing Mechanism

In this section we discuss the state of the art of the quantitative understanding of the sensing mechanism in nanowire-based field-effect biosensors. The quantitative understanding is important for predictive simulations, leads to a rational design, and the optimization of the nanowire sensors. Therefore we have to identify the crucial parts for modeling. The response of the sensor is dependent on the charge changes in the boundary layer. Hence we take now a look at this component of the sensor.

A p-doped silicon nanowire together with two contacts, a source and a drain contact, is shown in the lower half of Fig. 1.2. The nanowire transducer is usually located on top of a dielectric material and covered by a second dielectric material, which is exposed to the ionic solution. A conventional FET structure is shown in the upper half of Fig. 1.2: In this device, a gate contact is located on the top of the dielectric and a negative gate voltage V_G induces an accumulation of positive charge carriers near the silicon surface, which in turn induces an increase of conductance, while a positive gate voltage decreases the conductance. Vice-versa, when using an n-doped silicon nanowire, a negative gate voltage decreases the conductance and a positive gate voltage increases the conductance.

In field-effect biosensors, the gate contact is replaced by a functionalized boundary layer and an ionic solution containing target molecules. The dielectric covering the transducer is functionalized with receptor molecules: in the case of DNA sensors, the receptors are complementary single-stranded DNA; in the case of antigen sensors, the receptors are the corresponding antibodies. As target molecules in the liquid bind to the receptors, their presence and their partial charges change the charge concentration in the boundary layer, which in turn modulates the conductance of the nanowire transducer. In Fig. 1.2, the target molecules carry negative charges and act as a negative gate voltage. Hence accumulation of charge carriers again increases the conductance.

Additional control of the nanowire can be provided by the implementation of a backgate contact, which plays an important role for the sensitivity of such sensors (see Chapter 4). Furthermore, it is well-known that the nanowire surface is charged when in contact with water due to chemical reactions, and the surface charge depends on the material and the pH value. Therefore a double layer of ions forms at the surface.

The sensor signal is the measured current through the nanowire, which is modulated due to the gate effect as target molecules bind. In order to calculate the sensor response, it is therefore crucial to consider the boundary layer and the screening of the partial charges of the biomolecules by free ions. The charged boundary layer acts as the gate contact, so that electron and hole transport in the semiconductor must be calculated as a function of the boundary layer, the applied voltages, the geometry of the nanowire, and so forth.

These considerations imply that physically sound modeling and simulation must include firstly the charge concentration in the biofunctionalized boundary layer that gives rise to the field effect

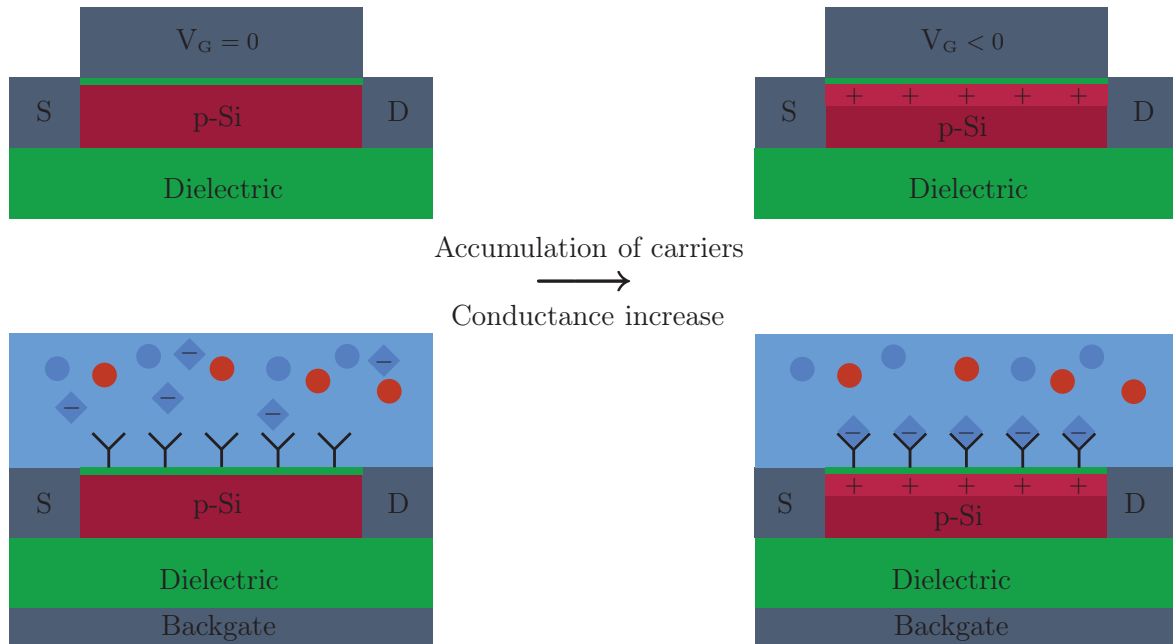


Figure 1.2: Working principle of a conventional FET (top) and a nanowire field-effect sensor (bottom). In both cases, negative charge at the gate contact or at the nanowire surface leads to an increase of conductance due to accumulation of charge carriers in the semiconductor near the negative charges.

and secondly the charge transport in the semiconducting transducer that translates the difference in charge in the boundary layer to the electrical signal. Clearly, the modeling and simulation of field-effect sensors is more complicated than the simulation of conventional FETs due to the additional boundary layer. In the best case, the sensor model is self-consistent meaning that the influences of all charges onto all charges are taken into account while including all applied potentials; this is usually achieved by solving the Poisson equation.

In summary, field-effect biosensors consist of two parts – namely the biofunctionalized boundary layer and the nanowire transducer – that shall be considered self-consistently. Models for the boundary layer, i.e., screening models, are discussed in Section 1.4. The sensor signal is measured as the current (or change in current) through the nanowire and cannot be explained by the surface models alone; hence suitable charge-transport models are discussed in Section 1.5. In order to connect these two parts and to solve the multiscale problem inherent in these sensors, a homogenization method is advantageous, which is presented in the following Section 1.3.

1.3 Homogenization

As mentioned above, the characteristic length scale of the biomolecules in the boundary layer is smaller than the dimensions of the nanowire by some orders of magnitude. This circumstance becomes obvious when we look at the, true to scale, schematic diagram of a DNA sensor in Fig. 1.3 where the right-hand side is a detailed view of the nanowire surface on the nanowire device on the left-hand side. Problems of this type are called multiscale problems (Bensoussan et al., 1978;

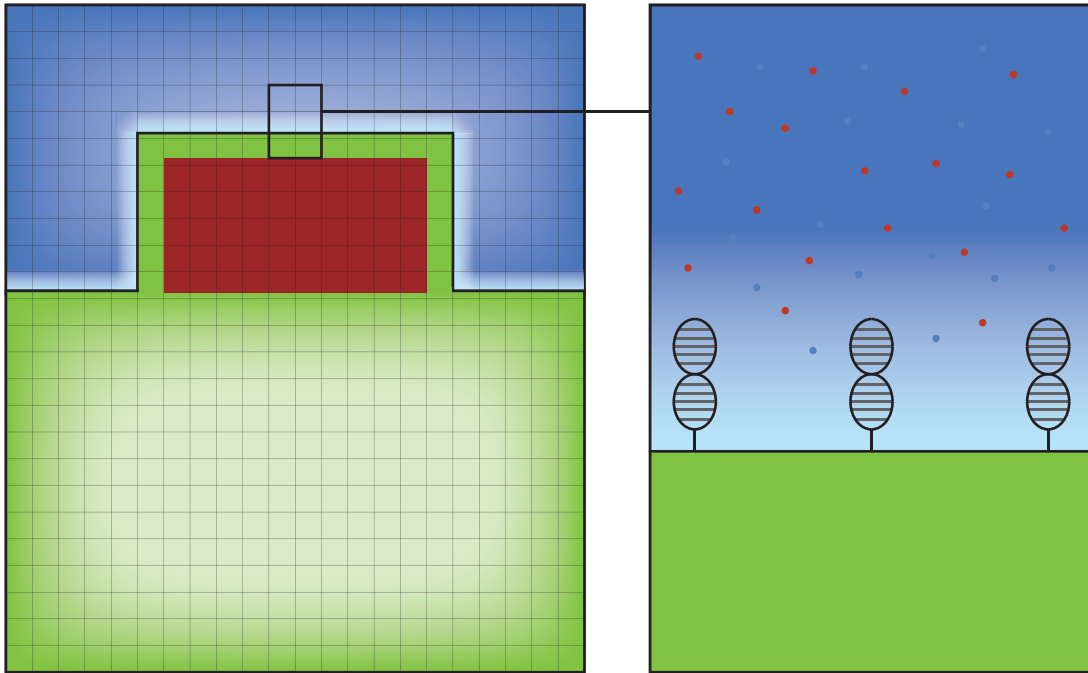


Figure 1.3: Schematic diagram of an NWFET, true to scale, with functionalized surface. The grid spacing on the left-hand side is $10 \text{ nm} \times 10 \text{ nm}$ and the detail on the right-hand side is 20 nm wide, 30 nm high, and is also true to scale. The depicted DNA is bound to the surface by a 1 nm long linker, is 5 nm high, and has a radius of 1 nm . The ions in the aqueous solution are modeled as charged hard spheres with a diameter of 0.3 nm .

Pavliotis and Stuart, 2007). A main motivation to study them is the fact that problems with a microscopic structure are extremely time consuming to solve numerically, since the microscopic structure must be resolved by the numerical grid. Homogenization generally yields equations of similar type, but with homogenized coefficients so that the numerical grids do not have to resolve the microscopic structure anymore. Then previously computationally intractable problems can be solved numerically with reasonable effort.

To obtain the sensor response in terms of the nanowire current, the electrostatic potential V must be computed everywhere in the simulation domain. Therefore, we usually solve the Poisson equation

$$-\nabla \cdot (\varepsilon(x, y, z) \nabla V(x, y, z)) = \rho(x, y, z) \quad \text{in } \Omega, \quad (1.1a)$$

$$V(0+, y, z) = V(0-, y, z) \quad \text{on } \Gamma, \quad (1.1b)$$

$$\varepsilon(0+, y, z) \partial_x V(0+, y, z) = \varepsilon(0-, y, z) \partial_x V(0-, y, z) \quad \text{on } \Gamma \quad (1.1c)$$

as the basic equation for the electrostatic potential, where V is the electrostatic potential and ε is the permittivity. Furthermore, ρ is the charge concentration in the different materials and will depend on the electrostatic potential itself in the drift-diffusion-Poisson system in Section 1.5. In the liquid, ρ describes the charge concentration in the ionic solution and hence also in the boundary layer. The interface Γ splits the domain $\Omega \subset \mathbb{R}^3$ into two parts Ω^+ and Ω^- . For the sake of notational simplicity, we assume that the normal vector of the interface Γ points in

the positive x -direction and is located at $x = 0$. The conditions (1.1b) and (1.1c) ensure the continuity of the electric potential and dielectric displacement in the presence of the discontinuity in the permittivity ε at the material boundaries.

The idea of the homogenization procedure is to compare the weak formulations of two problems: the first problem is the original problem above and the second, the homogenized problem, contains general interface conditions, but not the fast varying charge concentration, i.e., we replace the Poisson equation and the fast varying charge concentration ρ in the boundary layer by a simpler problem that does not exhibit a microscopic structure and oscillations.

At the end of the procedure, the interface conditions are derived by comparing the coefficients of the test function and its normal derivative with respect to the interface. Indeed it is found that the complicated, oscillating three-dimensional structure of the biomolecules, their partial charges and screening ions can be replaced by two interface conditions involving only two integral values of the charges in the boundary layer after the cell size in the boundary layer goes to zero (Heitzinger et al., 2010b).

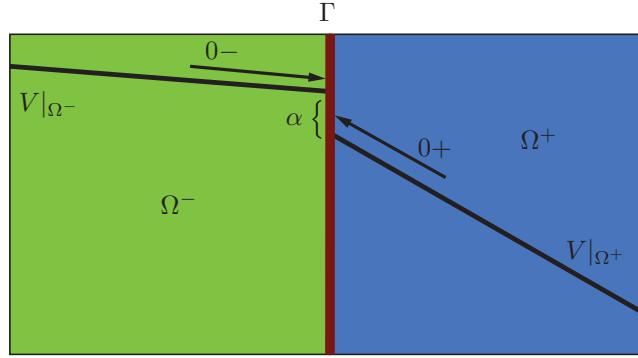


Figure 1.4: Schematic diagram of the electric potential V at the interface Γ in a cross section. The jump of size α of the electric potential is shown, while the jump of size β in the electric displacement results in a difference in the normal derivatives of the potential in Ω^- and Ω^+ .

After homogenization, the original problem (1.1) becomes the homogenized problem

$$-\nabla \cdot (\varepsilon(x, y, z) \nabla V(x, y, z)) = \begin{cases} \rho(x, y, z) & \text{in } \Omega^-, \\ 0 & \text{in } \Omega^+, \end{cases} \quad (1.2a)$$

$$V(0+, y, z) - V(0-, y, z) = \alpha \quad \text{on } \Gamma, \quad (1.2b)$$

$$\varepsilon(0+, y, z) \partial_x V(0+, y, z) - \varepsilon(0-, y, z) \partial_x V(0-, y, z) = \beta \quad \text{on } \Gamma, \quad (1.2c)$$

where V is now the homogenized potential and $0+$ denotes the limit at the interface Γ on the side of the liquid, while $0-$ is the limit on the side of the transducer as depicted in Fig. 1.4. The fast varying charge concentration in the surface layer is now, as stated before, subsumed in the macroscopic dipole-moment density ζ and the macroscopic surface-charge density γ of the boundary layer and

$$\alpha = \frac{\zeta(y, z)}{\varepsilon(0+, y, z)}, \quad \beta = -\gamma(y, z). \quad (1.3)$$

are just, for the sake of simplicity, abbreviations for the modified charges. Both ζ and γ may depend on y and z , the coordinates parallel to the surface, to allow for slow variations of the boundary layer along the interface.

The two interface conditions have the following interpretation (see also Fig. 1.4): the condition (1.2b) is a jump in the electrostatic potential and is given by the dipole-moment density of the boundary layer, whereas condition (1.2c) is a jump in the electrostatic field (or more precisely, in the electrostatic displacement) and is given by the surface-charge density (Cherstvy, 2011).

The values of ζ and γ are immediately obtained from the charge concentration in a cell of the boundary layer and can be obtained from any of the boundary-layer models in Section 1.4 (Heitzinger et al., 2010b).

In summary, the homogenization result decouples the microscopic and macroscopic length scales via the two interface conditions in (1.2). Details on the efficient implementation of the interface conditions are given in Chapter 2.

1.4 The Biofunctionalized Boundary Layer

The biofunctionalized boundary layer is the part of the sensor that provides selectivity. It also translates the presence of biomolecules into a change in the electrostatic potential in the semiconducting transducer due to a redistribution of charge in the boundary layer, when target molecules are present and bound to receptors. Since the sensing concept is based on the field effect, the charge concentration in the boundary layer is crucial for the quantitative understanding of the sensing mechanism.

An accurate model for the boundary layer has to incorporate several effects. In the simplest case, a non-functionalized nanowire is exposed to an electrolyte. Here the charge of the dielectric, e.g., SiO_2 or Si_3N_4 , which covers the transducer, depends on the pH value of the electrolyte due to reactions of the electrolyte with hydroxyl groups at the dielectric surface. This is a well-known effect for ISFETs and can be modeled by the site-dissociation model (Bergveld and Sibbald, 1988; Schöning and Poghossian, 2002; Xu et al., 2005) discussed in Section 1.4.1. This model together with the homogenization result in Section 1.3 and a charge-transport model for the nanowire can be used for the simulation of pH sensors.

Due to the surface charge of the dielectric, an electric double layer of free ions forms on the transducer. This is a well-known effect that is commonly simulated using Metropolis-Monte-Carlo simulations (Allen and Tildesley, 1987) in order to take the finite size of the ions into account. In addition to the electric double layer, receptor and target molecules with their partial charges are present at the surface, together with a cloud of screening, free ions. Furthermore, the charge state of biomolecules depends on the pH value and the biomolecules and their screening charges interact with the electric double layer.

These questions are – despite recent progress – still an area of active research (Alexov et al., 2011). Hence we describe the three main types of models for these effects in the following: the atomistic approach, i.e., Monte-Carlo simulations, the continuum approach, i.e., the Poisson-Boltzmann equation (Heitzinger et al., 2010a), and the empirical PROPKA model (Li et al., 2005) are discussed. Compact screening models, such as (Sørensen et al., 2007) have also been

developed for the simulation of nanowire sensors (De Vico et al., 2011, 2010; Vacic et al., 2011).

1.4.1 The Site-Dissociation Model

The surface of dielectric materials such as SiO_2 , Si_3N_4 , Al_2O_3 , and Ta_2O_5 is charged when in contact with an electrolyte and it is neutral only at the isoelectric point, a specific pH value. This surface charge provides an important baseline value, also regarding the operating regime of the sensor. Since the surface charge is a function of pH value, it was already investigated in ISFET theory. In the following, we give an overview on the site-dissociation model from Bergveld (Bergveld and Sibbald, 1988).

The site-dissociation model assumes that there is an interaction of the electrolyte with discrete surface sites which are amphoteric, i.e., the surface sites can be neutral, a proton donor, or a proton acceptor.

The reactions of the hydroxyl groups (AOH groups, where A is, for example, Si or Al in the case of an SiO_2 or Al_2O_3 surface) at the surface with the H^+ ions in their vicinity relate the equilibrium potential ψ_0 and the H^+ ions. These reactions are expressed in the equilibrium equations



where the dissociation constants K_a and K_b are

$$K_a = \frac{[\text{AO}^-][\text{H}^+]_s}{[\text{AOH}]}, \quad K_b = \frac{[\text{AOH}_2^+]}{[\text{AOH}][\text{H}^+]_s} \quad (1.5)$$

and where AO^- , AOH_2^+ and AOH represent the negative (deprotonated), positive (protonated), and neutral surface sites respectively and $[\cdot]$ denotes site concentration.

Furthermore, the concentration of the H^+ ions at the surface is related to the bulk concentration via Boltzmann statistics by

$$[\text{H}^+]_s = [\text{H}^+]_b \exp(-q\psi_0/(kT)), \quad (1.6)$$

where q is the elementary charge, k is the Boltzmann constant, and T is the temperature. Using the net surface charge

$$\sigma_0 := q([\text{AOH}_2^+] - [\text{AO}^-]) \quad (1.7)$$

and the total number of surface sites per unit area

$$N_s := [\text{AOH}] + [\text{AOH}_2^+] + [\text{AO}^-] \quad (1.8)$$

together with (1.5) and the assumption that $2(K_a K_b)^{1/2} \ll 1$ yields the equation (see also (Bousse et al., 1983))

$$\ln[\text{H}^+] - \ln(K_a/K_b)^{1/2} = \frac{q\psi_0}{kT} + \sinh^{-1} \left(\frac{\sigma_0}{2qN_s(K_a K_b)^{1/2}} \right) - \ln \left(1 - \frac{\sigma_0}{qN_s} \right). \quad (1.9)$$

From this equation and the assumption that $\sigma_0 \ll qN_s$, we obtain the relation between the isoelectric point pI (i.e., the pH value where the surface is charge neutral) and the surface potential ψ_0 as the equation

$$2.303(\text{pI} - \text{pH}) = \frac{q\psi_0}{kT} + \sinh^{-1} \left(\frac{q\psi_0}{kT\kappa} \right) \quad (1.10)$$

with

$$\kappa := \frac{2q^2 N_s (K_a K_b)^{1/2}}{kT C_L}, \quad (1.11)$$

where C_L is the constant capacitance of the double layer, i.e., C_L gives the relation $\sigma_0 = \psi_0 C_L$ between σ_0 and ψ_0 . Values reported in the literature are $N_s = 5 \cdot 10^{14} \text{ cm}^{-2}$ and $C_L = 20 \mu\text{Fcm}^{-2}$ for SiO_2 (Bergveld and Sibbald, 1988). In the case of an SiO_2 surface, the values of κ and pI are $\kappa = 0.14$ and $\text{pI} = 2.2$ (Bergveld and Sibbald, 1988). Finally, the net surface charge can be obtained from the equilibrium potential by multiplication by C_L . For a more detailed description see (Bousse et al., 1983; Harame et al., 1987).

1.4.2 Screening and Biomolecules

The modeling of the electrostatics of biomolecules such as proteins and DNA is not only essential for the simulation of nanowire field-effect sensors, but it is its own important research area. Hence it is not surprising that many approaches of different kinds have been developed, but it is astonishing that none of the methods is significantly better than the rest, each having its own advantages and disadvantages (Alexov et al., 2011; Kukic and Nielsen, 2010; Lu et al., 2008).

In the following, the three main types of biomolecule models are presented. Firstly, a Monte-Carlo algorithm for charged biomolecules at charged surfaces is discussed (Bulyha and Heitzinger, 2011). It is the first of its kind to include charged biomolecules and has been used for sensor simulation (Baumgartner et al., 2011a). The main advantage of the Monte-Carlo approach is that it takes into account the finite size of the ions. Secondly, continuum models are based on the Poisson-Boltzmann equation (PBE), a three-dimensional partial differential equation and one of the main equations in computational chemistry. Thirdly, empirical models have been developed and we give an overview on the PROPKA algorithm, which is one of the most used (Li et al., 2005), also for biosensor simulations (De Vico et al., 2011, 2010).

1.4.2.1 The Metropolis-Monte-Carlo Method

Recently, a Metropolis-Monte-Carlo (MMC) algorithm was developed for the simulation of biomolecules and free ions in the constant-voltage ensemble (Bulyha and Heitzinger, 2011). Here we give an overview on the method which is used for simulations in Chapter 4.

The simulation box is shown in Fig. 1.5. The biomolecules such as PNA (peptide nucleic acid), single-stranded DNA (ssDNA), or double-stranded DNA (dsDNA), are fixed at the bottom of the box. The length of the oligomers and their linkers can be adjusted to the desired length. The DNA and PNA oligomers are modeled as cylinders, where the partial charges of the phosphate groups of the backbone are situated on the cylinder surface on a helix while the free ions are

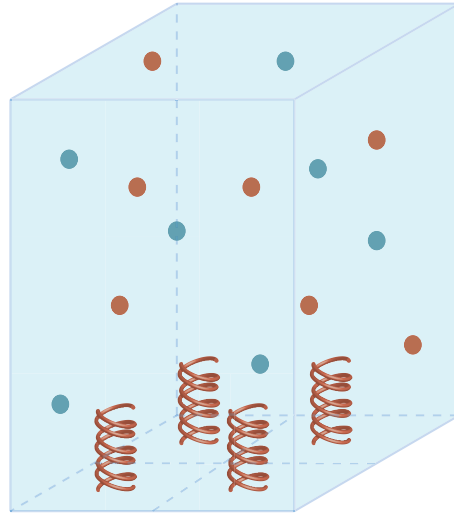


Figure 1.5: The simulation domain of a constant-voltage Metropolis-Monte-Carlo simulation. Here it contains 2×2 biomolecules at the bottom of the cell. The molecules can be rotated with respect to the surface (Bulyha and Heitzinger, 2011).

excluded. The points where the linkers are attached to the bottom of the box are arranged in an equidistant grid.

The reason for including many biomolecules in a single simulation box is computational. In order to be able to simulate electrolytes with realistic, low ionic concentrations and realistic concentrations of immobilized biomolecules, the simulation domain is quite small compared to the number of free ions; the small number of ions in the box leads to bad statistics in the Monte-Carlo simulation. Hence a larger simulation domain with a grid of molecules provides a sufficient number of ions and leads to much improved statistics.

Each oligomer is bound to the surface by a linker and the biomolecules together with their linkers are simulated as impenetrable cylinders with two hemispheres of the same radius on the top and at the bottom. In the case of PNA oligomers, the cylinders are uncharged, and in the case of ssDNA and dsDNA oligomers, they carry the charges of the phosphate groups of the backbone on their outside. The sizes correspond to the B-DNA conformation of DNA. The oligomers can additionally be rotated with respect to the surface.

The electrolyte in the simulation box is usually Na^+Cl^- . The ions are modeled as charged hard spheres and water is modeled as a continuous medium without structure.

The top and the bottom of the simulation box are impenetrable walls with given charge densities so that the electric field can be controlled. The bottom of the box carries the surface charge as calculated from the site-dissociation model in Section 1.4.1.

In order to calculate the ion concentration profile, a 3d MMC method must be used in the constant-voltage ensemble because of the voltage drop across the simulation box in sensor application. The constant-voltage ensemble (Kiyohara and Asaka, 2007) can be considered as an extension of the grand-canonical ensemble.

A simulation in the MMC constant-voltage ensemble starts with a random state of the system, i.e., the locations of all ions are random. A new state of the system is generated by randomly adding or deleting a pair of ions, changing the position of an ion while avoiding overlaps, and by transferring a random amount of charge between the walls. Then the potential energy is calculated for each state of the system. The interactions between all pairs of charge types, i.e., the ion-ion, the ion-biomolecule, the ion-plate, the biomolecule-plate, and the plate-plate interactions, are included in this calculation and the long-range contributions of the Coulomb forces are taken into account via integration over infinitely many periodically repeated cells. If the movement of a charge reduces the energy of the system, the new state is unconditionally accepted, while otherwise the movement is allowed only with a certain probability that depends exponentially on the energy difference.

Finally, the surface-charge density γ and the dipole-moment density ζ are calculated as integrals over the charge concentration in the simulation cell (Heitzinger et al., 2010b).

1.4.2.2 The Poisson-Boltzmann Equation

The most-common and well-established continuum model for the description of ionic concentrations and the electrostatic interactions is the Poisson-Boltzmann equation (Lu et al., 2008). It is one of the most important equations in computational chemistry and is often used to calculate ionic concentrations around molecules and the applications considered here at surfaces (Talasaz et al., 2006). The domain Ω is partitioned into two parts: the subdomain Ω_m of the molecule and the subdomain Ω_s of the solvent. Both regions are modeled by the nonlinear Poisson-Boltzmann equation

$$-\nabla \cdot (\varepsilon \nabla u) - \sum_{j=1}^K c_j q_j e^{-\xi q_j u} = \sum_{i=1}^N p_i \delta(x - x_i) \quad \text{in } \Omega_s, \quad (1.12a)$$

$$-\nabla \cdot (\varepsilon \nabla u) = \sum_{i=1}^N p_i \delta(x - x_i) \quad \text{in } \Omega_m, \quad (1.12b)$$

where ε is again the permittivity, c_j is the bulk concentration of free ion species j with charge q_j , p_i is a charge at x_i in Ω_m , and $\xi = 1/(kT)$, where k is the Boltzmann constant and T is the temperature.

On the interface between the two subdomains Ω_m and Ω_s , continuity equations for the potential u and the dielectric displacement (i.e., the permittivity times the normal derivative),

$$[u] = 0, \quad (1.13)$$

$$\left[\varepsilon \frac{\partial u}{\partial n} \right] = 0, \quad (1.14)$$

where $[.]$ denotes the difference of the limits in Ω_m and in Ω_s analogously to equations (1.2).

A leading special case of the PBE is the PBE for a symmetric, 1 : 1 electrolyte (Holst et al., 2012). With $K = 2$, the bulk concentration $c_j = c$, and $q_j = (-1)^j q$, equation (1.12a) simplifies to

$$-\nabla \cdot (\varepsilon \nabla u) + 2cq \sinh(\xi qu) = \sum_{i=1}^N p_i \delta(x - x_i). \quad (1.15)$$

This equation can be solved by various numerical methods such as the finite-difference method, the finite-volume method, or the boundary-element method (Lu et al., 2008). Nowadays several PBE solvers such as DelPhi (Honig and Nicholls, 1995), GRASP (Nicholls et al., 1991), MEAD (Bashford and Gerwert, 1992), UHBD (Davis et al., 1991), PBEQ (Im et al., 1998), APBS (Baker et al., 2000; Holst et al., 2000), and AFMPB (Lu et al., 2010a), are available for biochemistry and biophysics.

A stochastic version of the Poisson-Boltzmann equation was also used to quantify fluctuations in nanowire field-effect biosensors (Heitzinger et al., 2010a).

1.4.2.3 PROPKA

An empirical method for the calculation of protein charges and pK_a values is the FORTRAN program PROPKA (Bas et al., 2008; Li et al., 2005; Olsson et al., 2011; Rostkowski et al., 2011). This method uses the structure of proteins from PDB files to compare it with empirical data. An initial guess for the pK_a value pK_a^{water} of a titrable group in water is perturbed by the change $\Delta pK_a^{\text{water} \rightarrow \text{protein}}$ of the pK_a value due to the protein, i.e., the pK_a value is

$$pK_a = pK_a^{\text{water}} + \Delta pK_a^{\text{water} \rightarrow \text{protein}} \quad (1.16)$$

according to (Søndergaard et al., 2011). Here pK_a^{water} is obtained empirically and is well-known, while $\Delta pK_a^{\text{water} \rightarrow \text{protein}}$ is calculated by PROPKA.

From comparison with empirical data and investigations of the structure of the proteins in PDB files, the main contributions to $\Delta pK_a^{\text{water} \rightarrow \text{protein}}$ have been detected and approximated. In PROPKA3.1, these contributions are

$$\Delta pK_a^{\text{water} \rightarrow \text{protein}} = \Delta pK_a^{\text{desolv}} + \Delta pK_a^{\text{HB}} + \Delta pK_a^{\text{RE}} + \Delta pK_a^{\text{QQ}}, \quad (1.17)$$

where $\Delta pK_a^{\text{desolv}}$ describes the desolvation effects, ΔpK_a^{HB} describes the hydrogen-bond interactions, ΔpK_a^{RE} describes the contribution due to electrostatic reorganization energies, and ΔpK_a^{QQ} describes the Coulombic interactions. The Coulomb contribution due to charge-charge interactions is described for the protein residue i and a charge j from a charged or ionizable group as

$$\Delta pK_{a,i}^{\text{QQ}} = \frac{244\sigma_{ij}}{\epsilon r_{ij}} w^{\text{QQ}}(r_{ij}), \quad (1.18a)$$

$$w^{\text{QQ}}(r_{ij}) = \begin{cases} \frac{r_{ij}}{r_{\min}} & \text{if } r_{ij} \leq r_{\min}, \\ \frac{r_{ij} - r_{\min}}{r_{\max} - r_{\min}} & \text{if } r_{\min} \leq r_{ij} \leq r_{\max}, \\ 0 & \text{if } r_{ij} \geq r_{\max}, \end{cases} \quad (1.18b)$$

$$\sigma_{ij} = \begin{cases} -1 & \text{if } (i \in \text{acids and } j \in \text{bases}) \\ & \text{or } (i \in \text{bases and } pK_{a,i} < pK_{a,j}), \\ +1 & \text{if } (i \in \text{bases and } j \in \text{acids}) \\ & \text{or } (i \in \text{acids and } pK_{a,i} > pK_{a,j}), \\ 0 & \text{else,} \end{cases} \quad (1.18c)$$

where 244 is the Coulomb's-law coefficient in pK_a units, ϵ is the dielectric constant, and σ gives the direction of the pK_a shift. Furthermore r_{ij} is the distance between the charge centers and w is a weight function.

Short-distance contributions $\Delta pK_{a,i}^{HB}$ from hydrogen bonds or contributions $\Delta pK_{a,i}^{RE}$ from reversed hydrogen bonds are modeled as

$$\Delta pK_{a,i}^{HB} = \begin{cases} c^{HB} w^{HB}(r_{ij}) \cos \theta & \text{if } \theta \geq 90^\circ, \\ 0 & \text{else,} \end{cases} \quad (1.19a)$$

$$w^{HB}(r_{ij}) = \begin{cases} 1 & \text{if } r_{ij} \leq r_{min}, \\ \frac{r_{ij} - r_{min}}{r_{max} - r_{min}} & \text{if } r_{min} \leq r_{ij} \leq r_{max}, \\ 0 & \text{if } r_{ij} \geq r_{max}, \end{cases} \quad (1.19b)$$

where c^{HB} is a fitted constant, w is a weight function, and θ is the angle between the hydrogen bond and the hydrogen acceptor. Furthermore r_{ij} is the hydrogen-bond distance.

The desolvation effect due to nearby, non-hydrogen atoms ($k = 1, \dots, N$) with volume V_k is calculated as

$$\Delta pK_{a,i}^{desolv} = c \sum_{k=1}^N \frac{V_k}{r_{ik}^4}, \quad (1.20)$$

where c is an empirically determined constant and where the center of the atom k is a distance r_{ik} away from the center of residue i .

The charge of the molecule is the sum of the charges of the single amino acids $\sum q_i$. The charge q_i of the amino acid i can be calculated as (De Vico et al., 2010)

$$q_i = \frac{10^{pK_{a,i} - \text{pH}}}{1 + 10^{pK_{a,i} - \text{pH}}}. \quad (1.21)$$

1.4.3 Gas Sensors

Just for completeness we want to mention that the homogenization method is also applicable for gas sensors. Here no molecules are attached at the nanowire surface. Instead, reactions at the nanowire surface happen which can be computed from the solutions of systems of ODEs that govern the chemical reactions. In the case of SnO_2 based sensors in the presence of oxygen and a reducing gas such as CO, the chemisorption and ionization at the surface can be described by the system

$$\begin{aligned} \frac{dN_O}{dt} &= k_1([S] - N_O - N_S)[O_2]^{1/2} - k_{-1}N_O - \frac{dN_S}{dt}, \\ \frac{dN_S}{dt} &= k_2 n_s N_O - k_{-2}N_S, \end{aligned}$$

where N_O denotes the neutral-adsorbed-oxygen density, N_S is the ionized-oxygen density, and the k_i are the rate constants of the surface processes, while $[S]$ is the local adsorption-site density and $[O_2]$ is the oxygen concentration (Fort et al., 2006). Furthermore the electron concentration n_s corresponds to the surface-charge density $M_\gamma(V)$ and the dipole-moment density $M_\alpha(V)$ vanishes in the case of gas sensors since the distance from the surface is zero. Of course, there are many more systems of ODEs that are relevant for the modeling of gas sensors.

1.4.4 Comparison of Boundary-Layer Models

In summary, many approaches for the simulation of the partial charges of molecules, and in particular of DNA and proteins, have been developed. The main advantage of empirical models is the very fast prediction of pK_a values and charges with simulation times in the seconds range. Since these methods contain parameters that have been fitted to a sample data set, they are expected to work reliably only for molecules similar to the sample set. Hence more physically motivated methods are desirable, but come at a computational cost. In any case, empirical methods provide good approximations for many proteins and other biomolecules.

The simulation of DNA is facilitated by its comparatively simple and periodic structure. The structure of the biomolecules also plays a crucial role for the pK_a value and the partial charge, e.g., proteins have different charges if they are folded or unfolded. Hence it is often not possible to model and simulate the charging state of molecules accurately within feasible time or with feasible computational resources.

Hence this area continues to be one of active research and it is highly relevant for the quantitative understanding of affinity based sensors.

Using the methods summarized here, the charge concentration in boundary layers as they occur in nanowire field-effect sensors can be simulated. Furthermore, a transport model for the charges in the semiconducting nanowire is needed in order to simulate the whole sensor system. This is discussed in the next section.

1.5 The Charge Transport in the Nanowire

A realistic model for the charge transport through the nanowire transducer must be three-dimensional because of the real-world boundary conditions, namely the location of the source, drain, and backgate contacts (Elfström et al., 2007; Elfström and Linnros, 2008; Nair and Alam, 2007; Stern et al., 2007a).

In this section, we present a continuum model for charge transport through nanowires. Various models for particle transport in semiconductors have been developed focusing on different aspects; the two main approaches are the Boltzmann equation, equations derived thereof such as the drift-diffusion-Poisson system and diffusion-type equations (Heitzinger and Ringhofer, 2011), and Monte-Carlo methods. For the purpose of the simulation of field-effect sensors, continuum models are well-suited. The important aspect in field-effect sensors is the boundary layer and minute changes therein, and not so much advanced effects of charge transport in nanoscale structures. Hence the drift-diffusion-Poisson system is chosen to be the model for the charge transport in the nanowire.

1.5.1 The Drift-Diffusion-Poisson System

The charge transport in the semiconducting nanowire can be calculated by special models for confined structures (Ben Abdallah et al., 2001, 2006; Heitzinger and Ringhofer, 2011). In this work, the charge-transport equations in the nanowire that yield the carrier concentrations n and p is the drift-diffusion-Poisson system which is discussed in the following. As stated in

Section 1.3, the electric potential V is the solution of the Poisson equation

$$-\nabla \cdot (\varepsilon(x)\nabla V(x)) = \rho(x) \quad (1.22)$$

for the electric potential V , where $\rho(x)$ is the charge concentration and $x \in \Omega \subset \mathbb{R}^3$. When modeling semiconducting materials, the charge concentration includes the charge carriers, i.e., the electron concentration n and the hole concentration p . Furthermore, the doping concentration C_{dop} of the semiconductor is also part of the charge concentration. In detail the charge concentration for semiconductors is defined as

$$\rho_{\text{semi}}(x) := q(p(x) - n(x) + C_{\text{dop}}(x)), \quad (1.23)$$

where q is the elementary charge.

The concentrations n and p of the charge carriers are the solutions of the drift-diffusion equations

$$\nabla \cdot J_n = R, \quad (1.24a)$$

$$\nabla \cdot J_p = -R, \quad (1.24b)$$

$$J_n = D_n \nabla n - \mu_n n \nabla V, \quad (1.24c)$$

$$J_p = -D_p \nabla p - \mu_p p \nabla V, \quad (1.24d)$$

where D_n and D_p are the electron and hole diffusion coefficients, μ_n and μ_p are their mobilities, J_n and J_p are their current densities, and R denotes the recombination rate (Markowich et al., 1990; Selberherr, 1984). An important model for the recombination rate is the Shockley-Read-Hall recombination rate

$$R_{\text{SRH}} := \frac{np - n_i^2}{\tau_p(n + n_i) + \tau_n(p + n_i)}, \quad (1.25)$$

where n_i denotes the intrinsic charge concentration and τ_n and τ_p are the relaxation times of the electrons and holes, respectively. Furthermore, we assume that the Einstein relations $D_n = U_T \mu_n$ and $D_p = U_T \mu_p$ hold, where U_T is the thermal voltage.

In general the drift-diffusion-Poisson system is solved by the Scharfetter-Gummel iteration scheme which allows us to solve the charge of the boundary layer (the microscopic part of the model) and the charge transport (the macroscopic part of the model) in a self-consistent manner.

1.5.2 The Liquid

The equation for the aqueous solution outside the boundary layer (the boundary layer charges are already included in the surface charge density and the dipole moment density) is the Poisson-Boltzmann model

$$-\nabla \cdot (A \nabla V) = \sum_{\sigma} \sigma \eta e^{-\sigma \xi (V - \Phi)},$$

where η is the ionic concentration, the constant ξ is defined as $\xi := q/(kT)$ in terms of the Boltzmann constant k and the temperature T , and Φ is the Fermi level. The right-hand side is a sum over the valences σ of all ion species; for example, the index set $\sigma \in \{-1, +1\}$ corresponds to a 1:1 electrolyte such as Na^+Cl^- . In this case, the equation simplifies to

$$-\nabla \cdot (A \nabla V) = -2\eta \sinh(\xi(V - \Phi)).$$

1.5.3 Self-Consistent Simulation of Sensor Systems

We have now all parts for a self-consistent model of NWFETs. We consider the typical structure of a nanowire sensor as depicted in Fig. 1.6.

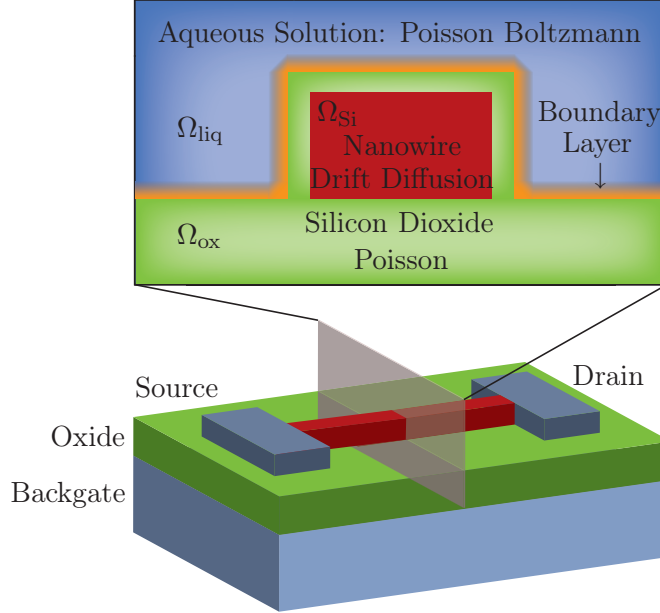


Figure 1.6: Schematic diagram of the nanowire sensor; the different materials and the corresponding equations, used in the simulations, are indicated.

Here, the silicon nanowire is covered by a thin, dielectric layer of silicon dioxide and surrounded by the aqueous solution containing the target molecules. Hence the simulation domain Ω can be partitioned into three subdomains Ω_{Si} , Ω_{ox} , and Ω_{liq} corresponding to these three materials. At the interface Γ between the nanowire surface and the liquid, the charge concentration exhibits a fast varying spatial structure which leads to the multiscale problem discussed in Section 1.3. To simplify notation, the x -axis is always normal to the smooth interface Γ located at $x = 0$.

The equation for the electric potential is now the homogenized Poisson equation

$$-\nabla \cdot (\varepsilon(x, y, z) \nabla V(x, y, z)) = \begin{cases} \rho(x, y, z) & \text{in } \Omega_{\text{Si}} \cup \Omega_{\text{ox}}, \\ 0 & \text{in } \Omega_{\text{blayer}}, \\ -2\eta \sinh(\xi(V - \Phi)) & \text{in } \Omega_{\text{liq}} \end{cases} \quad (1.26a)$$

$$V(0+, y, z) - V(0-, y, z) = \frac{\zeta(y, z)}{\varepsilon(0+)} \quad \text{on } \Gamma, \quad (1.26b)$$

$$\varepsilon_{\text{liq}} \partial_x V(0+, y, z) - \varepsilon_{\text{ox}} \partial_x V(0-, y, z) = -\gamma(y, z) \quad \text{on } \Gamma, \quad (1.26c)$$

where $0+$ denotes the limit at the interface in the outside of the nanowire, while $0-$ is the limit in the inside. The cumulative effect of the fast varying charge concentration in the surface layer is now given by the macroscopic dipole-moment density ζ and the macroscopic surface-charge density γ ; they are calculated by the models in Section 1.4.

After modeling the charges in the boundary layer, we now turn to the charge concentration ρ in the remaining materials. In the semiconductor, i.e., in Ω_{Si} , the Poisson equation is

$$-\nabla \cdot (\varepsilon_{\text{Si}} \nabla V) = \rho_{\text{semi}}(n, p), \quad (1.27)$$

where $\rho_{\text{semi}}(n, p)$ is given by the drift-diffusion equations in Section 1.5.1.

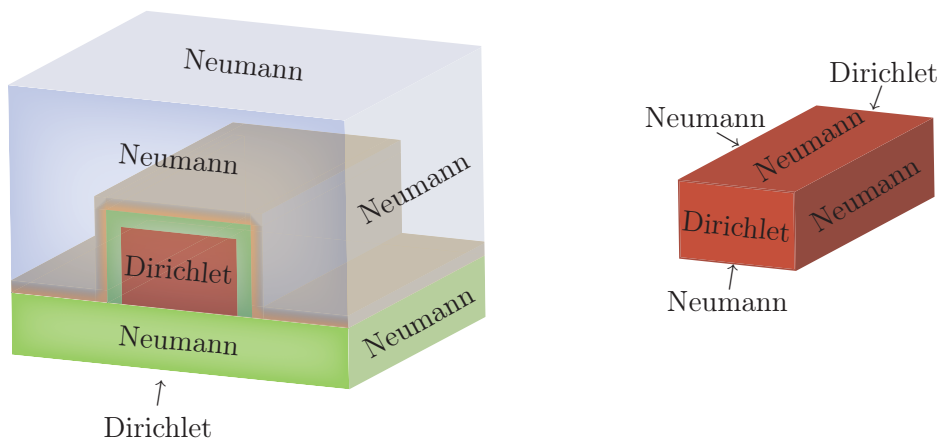


Figure 1.7: On the left-hand side the boundary conditions for the electric potential are indicated. The potential satisfies Dirichlet conditions for Ohmic contacts at the source and at the drain as well as Dirichlet conditions for the applied voltage at the backgate. Everywhere else, the potential at the boundary is described by Neumann conditions. For the drift-diffusion-Poisson system we need additional boundary conditions at the nanowire. The electron and hole concentrations satisfy Dirichlet conditions at the source and the drain. Everywhere else Neumann conditions hold.

The aqueous solution Ω_{liq} is described by the Poisson-Boltzmann equation already discussed in Section 1.4.2.2. The charge concentration on the right-hand side is a hyperbolic sine (in the case of 1:1 electrolyte) with the bulk ionic concentration as a factor.

At the source, drain, and backgate contacts, Dirichlet boundary conditions, as depicted in Fig. 1.7, hold, as well as at the electrode in the liquid if there is one (Lu et al., 2010b). Zero Neumann boundary conditions, i.e., vanishing electric fields, are used everywhere else. The inclusion of backgate contacts is crucial, since the operating regime of the sensor can be adjusted and optimized in this way (see Chapter 4) (Baumgartner et al., 2011a,c). We denote the boundary conditions at the silicon nanowire as $\partial\Omega_{D,\text{Si}}$ for the Dirichlet boundary and $\partial\Omega_{N,\text{Si}}$ for the Neumann boundary. The notation for the remaining Dirichlet boundary is $\partial\Omega_D$ and for the remaining Neumann boundary $\partial\Omega_N$.

Summarized, we have to solve the boundary-value problem

$$\begin{aligned}
-\nabla \cdot (\varepsilon_{\text{Si}} \nabla V) &= q(p - n + C_{\text{dop}}) && \text{in } \Omega_{\text{Si}}, && (1.28a) \\
-\nabla \cdot (\varepsilon_{\text{ox}} \nabla V) &= 0 && \text{in } \Omega_{\text{ox}}, && (1.28b) \\
-\nabla \cdot (\varepsilon_{\text{liq}} \nabla V) &= 0 && \text{in } \Omega_{\text{blayer}}, && (1.28c) \\
-\nabla \cdot (\varepsilon_{\text{liq}} \nabla V) &= -2\eta \sinh(\xi(V - \Phi)) && \text{in } \Omega_{\text{liq}}, && (1.28d) \\
V(x+) - V(x-) &= \alpha && \text{on } \Gamma, && (1.28e) \\
\varepsilon_{\text{liq}} \partial_x V(x+) - \varepsilon_{\text{ox}} \partial_x V(x-) &= \beta && \text{on } \Gamma, && (1.28f) \\
\nabla \cdot J_n &= \frac{np - n_i^2}{\tau_p(n + n_i) + \tau_n(p + n_i)} && \text{in } \Omega_{\text{Si}}, && (1.28g) \\
\nabla \cdot J_p &= -\frac{np - n_i^2}{\tau_p(n + n_i) + \tau_n(p + n_i)} && \text{in } \Omega_{\text{Si}}, && (1.28h) \\
J_n &= D_n \nabla n - \mu_n n \nabla V && \text{in } \Omega_{\text{Si}}, && (1.28i) \\
J_p &= -D_p \nabla p - \mu_p p \nabla V && \text{in } \Omega_{\text{Si}}, && (1.28j) \\
V &= V_D = V_{\text{applied}} + U_T \ln\left(\frac{n_D}{n_i}\right) && \text{on } \partial\Omega_{D,\text{Si}}, && (1.28k) \\
V &= V_{\text{applied}} && \text{on } \partial\Omega_D, && (1.28l) \\
n &= n_D = \frac{1}{2} \left(C_{\text{dop}} + \sqrt{C_{\text{dop}}^2 + 4n_i^2} \right) && \text{on } \partial\Omega_{D,\text{Si}}, && (1.28m) \\
p &= p_D = \frac{1}{2} \left(-C_{\text{dop}} + \sqrt{C_{\text{dop}}^2 + 4n_i^2} \right) && \text{on } \partial\Omega_{D,\text{Si}}, && (1.28n) \\
\nabla_\nu V &= 0 && \text{on } \partial\Omega_N, && (1.28o) \\
\nabla_\nu n = 0, \quad \nabla_\nu p &= 0 && \text{on } \partial\Omega_{N,\text{Si}}. && (1.28p)
\end{aligned}$$

for the electrical potential V , the electron density n , and the hole density p . The nanowire sensors governed by this system of equations are biosensors (Li et al., 2006; Stern et al., 2007a, 2008, 2010; Tian et al., 2010; Zheng et al., 2005) as well as gas sensors (Brunet et al., 2012; Griessler et al., 2011; Huang et al., 2010; Köck et al., 2009; Tischner et al., 2009; Zima et al., 2010).

The values of α and β can be stored in look-up tables depending on the surface potential. Then the whole sensor can be simulated self-consistently using an enhanced Scharfetter-Gummel iteration scheme so that no computational penalty is paid compared to solving the classical drift-diffusion-Poisson system (Baumgartner and Heitzinger, 2012a).

1.6 Summary

Nanowire sensors have been demonstrated experimentally in recent years, and they are a technology that is currently being developed. Nanowires are extremely well-suited for sensing purposes due to their single-crystalline structure and their high surface-to-volume ratio.

Quantitative understanding of this new technology is crucial for the rational design and the optimization of various devices. The boundary layer containing the biomolecules at the nanowire transducer is responsible for sensitivity and selectivity. Therefore the boundary layer and its

effect on the transducer are the crucial aspects of these field-effect sensors. Regarding modeling and simulation, these two aspects are novel compared to the well studied area of semiconductor devices and new intriguing questions arise. Hence the modeling and simulation of field-effect sensors goes beyond the modeling and simulation of semiconductor transistors.

This becomes obvious after a look on the system of equations describing the nanowire field-effect sensor.

The boundary layer must be modeled as realistically as possible. A mathematical method to achieve this in face of the multiscale aspect of the problem is to homogenize the partial differential equations that model the system. This allows us to simulate large structure while including effects on the microscopic length scale, i.e., the length scale of single molecules in the boundary layer.

The screening of the partial charges of the biomolecules in the boundary layer can be simulated by continuum models such as the Poisson–Boltzmann equation and by atomistic models such as Metropolis-Monte-Carlo algorithms while calculating the partial charges by a model such as PROPKA.

Since a solution for the drift-diffusion equations exists and is unique around thermal equilibrium we are going to prove this also for our system of equations including the jump conditions in Chapter 2.

Although the homogenization method reduces the computation cost, the linear systems after discretization are still large. To avoid this issue a parallel algorithm is presented in Chapter 3.

Using this self-consistent model, all relevant physical and geometrical properties can be included in the simulations. This makes it possible to provide realistic simulations and to predict sensitivity, see Chapter 4.

Analysis of the Model Equations Existence and Local Uniqueness

THE ANALYSIS of the model equations (1.28) described in Section 1.5.3 consists of an existence and a local uniqueness result.

Before we start with the discretization of the mathematical model and the simulations, it should be clear if a solution exists at all and if it is unique. Only then, the numerics can work. To get an indication for how far our analysis can go let us take a look at our system of equations.

It is important to note that our model (1.28) is self-consistent; more precisely, the system of equations has the structure

$$V = V(n, p, \alpha, \beta), \tag{2.1}$$

$$n = n(V, p), \tag{2.2}$$

$$p = p(V, n), \tag{2.3}$$

$$\alpha = M_\alpha(V), \tag{2.4}$$

$$\beta = M_\beta(V), \tag{2.5}$$

where n and p are the solutions of the drift-diffusion equations. From the drift-diffusion-Poisson system we know that we have an existence of a solution and a unique solution around thermal equilibrium (Buet and Dellacherie, 2010; Ghani and Masmoudi, 2010; Markowich, 1986; Markowich et al., 1990). Hence the best result we can get for our system is, as for the drift-diffusion equations, existence of a solution and a unique solution around an equilibrium. In fact we can show these properties, which is the aim of this chapter.

Therefore the values α and β of the interface conditions are given by microscopic models M_α and M_β for the surface-charge density and the dipole-moment density of the boundary layer as

discussed in Section 1.4. They generally depend on the electrostatic potential and usually on the electrostatic potential close to the boundary layer. The multiscale problem is also extensively discussed in earlier work by (Heitzinger et al., 2010b; Ringhofer and Heitzinger, 2008).

In the following we describe the system (1.28) in Slotboom variables which is necessary for the analysis of these equations. Then, in Section 2.3, the existence of solutions of semilinear elliptic problems with interface conditions is shown. Based on the lemmata in this section, the existence of solutions of the model equations is proved in Section 2.4. Furthermore, in Section 2.5, we show local uniqueness of the solution around the equilibrium state, i.e., when the applied voltages are small enough.

2.1 Slotboom Variables

The drift-diffusion-Poisson system can be written in Slotboom variables u and v , which are defined as

$$n =: n_i e^{V/U_T} u, \quad (2.6)$$

$$p =: n_i e^{-V/U_T} v. \quad (2.7)$$

Then, system (1.24a) becomes

$$-\nabla \cdot (A \nabla V) = q n_i (e^{-V/U_T} v - e^{V/U_T} u) + q C_{\text{dop}}, \quad (2.8)$$

$$U_T n_i \nabla \cdot (\mu_n e^{V/U_T} \nabla u) = n_i \frac{uv - 1}{\tau_p (e^{V/U_T} u + 1) + \tau_n (e^{-V/U_T} v + 1)}, \quad (2.9)$$

$$U_T n_i \nabla \cdot (\mu_p e^{-V/U_T} \nabla v) = n_i \frac{uv - 1}{\tau_p (e^{V/U_T} u + 1) + \tau_n (e^{-V/U_T} v + 1)}. \quad (2.10)$$

where the permittivity ε is now treated as a coefficient function A and the corresponding Dirichlet boundary conditions are

$$V|_{\partial\Omega_D} = V_D, \quad u|_{\partial\Omega_{D,\text{Si}}} = u_D, \quad v|_{\partial\Omega_{D,\text{Si}}} = v_D \quad (2.11)$$

as in Section 1.5.3. For details about the boundary conditions at the Ohmic contacts the reader is referred to (Markowich et al., 1990). The zero Neumann conditions

$$\nabla_\nu V|_{\partial\Omega_N} = 0, \quad \nabla_\nu u|_{\partial\Omega_{N,\text{Si}}} = 0, \quad \nabla_\nu v|_{\partial\Omega_{N,\text{Si}}} = 0 \quad (2.12)$$

hold on the Neumann part of the boundary (see Section 1.5.3).

In summary, the boundary-value problem (1.28) in Slotboom variables is the boundary-value

problem

$$-\nabla \cdot (A\nabla V) = qC_{\text{dop}} - qn_i(e^{V/U_T}u - e^{-V/U_T}v) \quad \text{in } \Omega_{\text{Si}}, \quad (2.13a)$$

$$-\nabla \cdot (A\nabla V) = 0 \quad \text{in } \Omega_{\text{ox}}, \quad (2.13b)$$

$$-\nabla \cdot (A\nabla V) = -2\eta \sinh(\xi(V - \Phi)) \quad \text{in } \Omega_{\text{liq}}, \quad (2.13c)$$

$$V(x+) - V(x-) = \alpha \quad \text{on } \Gamma, \quad (2.13d)$$

$$A(0+)\partial_x V(x+) - A(0-)\partial_x V(x-) = \beta \quad \text{on } \Gamma, \quad (2.13e)$$

$$U_T n_i \nabla \cdot (\mu_n e^{V/U_T} \nabla u) = n_i \frac{uv-1}{\tau_p(e^{V/U_T}u+1)+\tau_n(e^{-V/U_T}v+1)} \quad \text{in } \Omega_{\text{Si}}, \quad (2.13f)$$

$$U_T n_i \nabla \cdot (\mu_p e^{-V/U_T} \nabla v) = n_i \frac{uv-1}{\tau_p(e^{V/U_T}u+1)+\tau_n(e^{-V/U_T}v+1)} \quad \text{in } \Omega_{\text{Si}}, \quad (2.13g)$$

$$\alpha = M_\alpha(V) \quad \text{on } \Gamma, \quad (2.13h)$$

$$\beta = M_\beta(V) \quad \text{on } \Gamma, \quad (2.13i)$$

$$V = V_D \quad \text{on } \partial\Omega_D, \quad (2.13j)$$

$$u = u_D, \quad v = v_D \quad \text{on } \partial\Omega_{D,\text{Si}}, \quad (2.13k)$$

$$\nabla_\nu V = 0 \quad \text{on } \partial\Omega_N, \quad (2.13l)$$

$$\nabla_\nu u = 0, \quad \nabla_\nu v = 0 \quad \text{on } \partial\Omega_{N,\text{Si}}. \quad (2.13m)$$

2.2 Existence Theorem

In order to state the existence result, the coefficients and boundary conditions in the boundary-value problem (2.13) have to satisfy the following assumptions.

Assumptions 2.2.1.

(i) The bounded domain $\Omega \subset \mathbb{R}^3$ has a C^2 Dirichlet boundary $\partial\Omega_D$, the Neumann boundary $\partial\Omega_N$ consists of C^2 segments, and the Lebesgue measure of the Dirichlet boundary $\partial\Omega_D$ is nonzero.

The C^2 hypersurface $\Gamma \subset \Omega$ splits the domain Ω into two nonempty domains Ω^+ and Ω^- so that $\text{meas}(\Gamma \cap \partial\Omega) = 0$ and $\Gamma \cap \partial\Omega \subset \partial\Omega_N$ hold.

(ii) The coefficient functions A , μ_n , and μ_p are uniformly elliptic and bounded with $A|_{\Omega^+} \in C^1(\Omega^+, \mathbb{R}^{3 \times 3})$, $A|_{\Omega^-} \in C^1(\Omega^-, \mathbb{R}^{3 \times 3})$, and $\mu_n, \mu_p \in C^1(\Omega_{\text{Si}}, \mathbb{R}^{3 \times 3})$.

For the data, the inclusions $f \in L^\infty(\Omega)$, $V_D \in H^{1/2}(\partial\Omega_D) \cap L^\infty(\Gamma)$, and $u_D, v_D \in H^{1/2}(\partial\Omega_D)$ hold.

(iii) The doping concentration $C_{\text{dop}}(x)$ is bounded above and below and we define

$$\underline{C} := \inf_{x \in \Omega} C_{\text{dop}}(x) \leq C(x) \leq \sup_{x \in \Omega} C_{\text{dop}}(x) =: \overline{C}.$$

(iv) There is a constant $K \geq 1$ satisfying

$$\frac{1}{K} \leq u_D(x), v_D(x) \leq K \quad \forall x \in \partial\Omega_D.$$

- (v) The microscopic models M_α and M_β depend continuously in $H^1(\Omega)$ on the potential V , and for every potential V in $H^1(\Omega) \cap L^\infty(\Omega)$, the inclusions $\alpha(y) = M_\alpha(V) \in H^{1/2}(\Gamma) \cap L^\infty(\Gamma)$ and $\beta(y) = M_\beta(V) \in L^\infty(\Gamma)$ hold.

Using these assumptions, we can state the existence result.

Theorem 2.2.2 (Existence).

Under Assumptions 2.2.1, there exists a solution

$$(V, u, v, \alpha, \beta) \in (H^1(\Omega \setminus \Gamma) \cap L^\infty(\Omega \setminus \Gamma)) \times (H^1(\Omega_{\text{Si}}) \cap L^\infty(\Omega_{\text{Si}}))^2 \times (H^1(\Gamma) \cap L^\infty(\Gamma))^2$$

of the boundary-value problem (2.13) and it satisfies the L^∞ -estimate

$$\begin{aligned} \frac{1}{K} &\leq u(x) \leq K && \text{in } \Omega_{\text{Si}}, \\ \frac{1}{K} &\leq v(x) \leq K && \text{in } \Omega_{\text{Si}}, \\ \underline{V} &\leq V(x) \leq \bar{V} && \text{in } \Omega, \end{aligned}$$

where

$$\begin{aligned} \underline{V} &:= \min \left(\inf_{\partial\Omega_D} V_D, \Phi - \sup_{\Omega} V_L, U_T \ln \left(\frac{1}{2Kn_i} \left(\underline{C} + \sqrt{\underline{C}^2 + 4n_i^2} \right) \right) - \sup_{\Omega} V_L \right), \\ \bar{V} &:= \max \left(\sup_{\partial\Omega_D} V_D, \Phi - \inf_{\Omega} V_L, U_T \ln \left(\frac{K}{2n_i} \left(\bar{C} + \sqrt{\bar{C}^2 + 4n_i^2} \right) \right) - \inf_{\Omega} V_L \right) \end{aligned}$$

and where V_L is the solution of the linear equation in Lemma 2.3.1, for which the estimate

$$\|V_L\|_{H^1(\Omega)} \leq C(\|\beta\|_{L^2(\Gamma)} + \|V_D\|_{H^{1/2}(\partial\Omega)} + \|\alpha\|_{H^{1/2}(\Gamma)}).$$

holds.

The existence of solutions will be shown by applying the Schauder fixed-point theorem similarly to (Markowich et al., 1990) for the drift-diffusion equations. It is also known that solutions of the nonlinear Poisson-Boltzmann equation exist. The main issue of our model is how to treat the different equations on a single domain and how the interface conditions (1.2b) and (1.2c) influence estimates of the solutions. As stated in Section 1.3, the interface conditions are jumps in the potential V and in the field $-\partial_x V$. The size of the jumps depends on the values of α and β ; large values of α or β result in large absolute values of the potential.

The influence of the interface conditions on semilinear elliptic problems will be discussed in the following section. Based on the lemmata in the following section, the existence result will be proved in Section 2.4.

2.3 Semilinear problems including interface conditions

In the proof of the existence result, we will need two lemmata. The first one is concerned with linear elliptic problems with jumps of the form (1.2) and the second one yields the existence and

uniqueness of a solution of semilinear elliptic problems including jumps. An a-priori estimate is provided as well.

In the following, $\Gamma \subset \mathbb{R}^d$ will be a C^2 hypersurface in the domain Ω which splits the domain and its boundary into two parts Ω^+ and Ω^- . Here, for the sake of notational simplicity, we denote the one-dimensional coordinate orthogonal to Γ by x and the remaining $(d-1)$ -dimensional coordinates by y . Consequently, the notation $u(0+, y)$ means the limit within Ω^+ and $u(0-, y)$ is the corresponding limit within Ω^- . Furthermore, the jump conditions α and β depend only on the spatial variable y and not on the potential V as it arises in the iterative structure of the proof of Theorem 2.2.2. The Dirichlet part of the boundary is denoted by $\partial\Omega_D$ and the Neumann part by $\partial\Omega_N$.

Lemma 2.3.1 (Elliptic boundary-value problems with interface conditions).

Assume that $\Omega \subset \mathbb{R}^d$ is a bounded domain with a C^2 boundary split into two nonempty domains Ω^+ and Ω^- by the C^2 hypersurface Γ so that $\text{meas}(\Gamma \cap \partial\Omega) = 0$. Suppose that A with $A|_{\Omega^+} \in C^1(\Omega^+, \mathbb{R}^{d \times d})$ and $A|_{\Omega^-} \in C^1(\Omega^-, \mathbb{R}^{d \times d})$ is uniformly elliptic and that $\alpha \in H^{1/2}(\Gamma)$, $\beta \in L^2(\Gamma)$, $f \in L^2(\Omega)$, and $u_D \in H^{1/2}(\partial\Omega_D)$ hold. Suppose further that $\partial\Omega \cap \Gamma \subset \partial\Omega_N$ holds or that the jump α is compatible with the Dirichlet boundary conditions u_D , i.e., $u_D(0+) - u_D(0-) = \alpha$ holds on $\partial\Omega_D$.

Then the boundary-value problem with interface conditions

$$\begin{aligned} -\nabla \cdot (A(x)\nabla u) &= f && \text{in } \Omega \setminus \Gamma, \\ u(0+, y) - u(0-, y) &= \alpha && \text{on } \Gamma, \\ A(0+)\partial_x u(0+, y) - A(0-)\partial_x u(0-, y) &= \beta && \text{on } \Gamma, \\ \nabla_\nu u &= 0 && \text{on } \partial\Omega_N, \\ u &= u_D && \text{on } \partial\Omega_D \end{aligned}$$

has a unique solution $u \in L^2(\Omega)$ and $u|_{\Omega^+} \in H^1(\Omega^+)$ and $u|_{\Omega^-} \in H^1(\Omega^-)$ hold. Furthermore, the estimate

$$\|u\|_{H^1(\Omega^+)} + \|u\|_{H^1(\Omega^-)} \leq C(\|f\|_{L^2(\Omega)} + \|\beta\|_{L^2(\Gamma)} + \|u_D\|_{H^{1/2}(\partial\Omega)} + \|\alpha\|_{H^{1/2}(\Gamma)})$$

holds.

Proof. We extend $\alpha \in H^{1/2}(\Gamma)$ to $\bar{\alpha} \in L^2(\bar{\Omega})$ so that $\bar{\alpha}|_\Gamma = \alpha$, $\bar{\alpha}|_{\Omega^-} = 0$, $\bar{\alpha}|_{\Gamma \cup \Omega^+} \in H^1(\Gamma \cup \Omega^+)$, $\bar{\alpha}|_{\partial\Omega_D} = 0$, and $(\nabla_\nu \bar{\alpha})|_{\partial\Omega_N} = 0$. Such an extension $\bar{\alpha}$ can always be found by solving, e.g., the Laplace equation, since the boundary conditions are smooth enough. Similarly, we extend $u_D \in H^{1/2}(\partial\Omega)$ to $\bar{u}_D \in H^1(\Omega)$. We define

$$w := u - \bar{u}_D - \bar{\alpha} \tag{2.14}$$

so that the first interface condition becomes $w(0+) - w(0-) = 0$ and the Dirichlet boundary conditions become homogeneous.

Multiplication by test functions v with $v|_{\Omega^+} \in H^1(\Omega^+)$, $v|_{\Omega^-} \in H^1(\Omega^-)$, and $v|_{\partial\Omega} = 0$ and integration by parts on Ω^+ and Ω^- yields the weak formulation for $w \in H_0^1(\Omega)$ as

$$\langle A\nabla w, \nabla v \rangle = \langle f, v \rangle + \int_\Gamma \beta v ds - \langle A\nabla(\bar{u}_D + \bar{\alpha}), \nabla v \rangle, \tag{2.15}$$

where $\langle \cdot, \cdot \rangle$ denotes the scalar product $\langle f, g \rangle := \int_{\Omega^+} fg + \int_{\Omega^-} fg$ and where we have used the identity

$$\int_{\Gamma} A(0+) \partial_x u(0+, y) v dy - \int_{\Gamma} A(0-) \partial_x u(0-, y) v dy = \int_{\Gamma} \beta v dy. \quad (2.16)$$

Since the right-hand side of the weak formulation is a bounded functional, the Lax-Milgram Theorem yields the assertion.

The extensions \bar{u}_D and $\bar{\alpha}$ are not unique. Therefore the uniqueness of the solution u must be shown as well. Suppose u_1 and u_2 are two solutions. We define $u := u_1 - u_2$ and find that u solves the homogeneous problem

$$-\nabla \cdot (A(x) \nabla u) = 0 \quad \text{in } \Omega \setminus \Gamma, \quad (2.17)$$

$$u(0+, y) - u(0-, y) = 0 \quad \text{on } \Gamma, \quad (2.18)$$

$$A(0+) \partial_x u(0+, y) - A(0-) \partial_x u(0-, y) = 0 \quad \text{on } \Gamma, \quad (2.19)$$

$$\nabla_{\nu} u = 0 \quad \text{on } \partial\Omega_N, \quad (2.20)$$

$$u = 0 \quad \text{on } \partial\Omega_D \quad (2.21)$$

and hence the maximum principle (see (Protter and Weinberger, 1967)) yields $u = u_1 - u_2 = 0$ almost everywhere.

Finally, we show the estimate. The definition of w yields

$$\|u\|_{H^1(\Omega^+)} \leq \|w\|_{H^1(\Omega^+)} + \|\bar{u}_D\|_{H^1(\Omega^+)} + \|\bar{\alpha}\|_{H^1(\Omega^+)}, \quad (2.22)$$

$$\|u\|_{H^1(\Omega^-)} \leq \|w\|_{H^1(\Omega^-)} + \|\bar{u}_D\|_{H^1(\Omega^-)} + \|\bar{\alpha}\|_{H^1(\Omega^-)}. \quad (2.23)$$

Substituting $v = w$ in the weak formulation and using the uniform ellipticity of A , we obtain

$$\begin{aligned} \|w\|_{H^1(\Omega^+)} + \|w\|_{H^1(\Omega^-)} &\leq C(\|f\|_{L^2(\Omega^+)} + \|f\|_{L^2(\Omega^-)} + \|\beta\|_{L^2(\Gamma)} \\ &\quad + \|\bar{u}_D\|_{H^1(\Omega^+)} + \|\bar{\alpha}\|_{H^1(\Omega^+)} + \|\bar{u}_D\|_{H^1(\Omega^-)} + \|\bar{\alpha}\|_{H^1(\Omega^-)}). \end{aligned} \quad (2.24)$$

Combining these inequalities and using the inequality $\|\bar{\phi}\|_{H^1(\Omega)} \leq C\|\phi\|_{H^{1/2}(\partial\Omega)}$ (Ding, 1996) yields the asserted estimate. (Note that C denotes a general constant.) \square

The estimate allows a physical interpretation. The value β corresponds to the presence of charges; therefore f and β are present in the estimate analogously in the same norm as $\|f\|_{L^2(\Omega)}$ and $\|\beta\|_{L^2(\Gamma)}$, respectively. The value α corresponds to a dipole moment and results in a shift or jump of the potential; this is similar to a Dirichlet boundary condition and hence α and u_D appear as $\|\alpha\|_{H^{1/2}(\Gamma)}$ and $\|u_D\|_{H^{1/2}(\partial\Omega)}$ in the same norm. This means that the terms on the right-hand side of the estimate are consistent with the physical meaning of the problem.

If in Lemma 2.3.1 the data α , β , f , and u_D are bounded, then the solution u is bounded as well, i.e., $u \in L^\infty(\Omega)$ (see, e.g., (Caffarelli and Cabré, 1995)).

Having treated the linear problem with interface conditions, we now consider the semilinear

problem with interface conditions

$$-\nabla \cdot (A(x)\nabla u) + g(x, u) = f \quad \text{in } \Omega \setminus \Gamma, \quad (2.25a)$$

$$u(0+, y) - u(0-, y) = \alpha \quad \text{on } \Gamma, \quad (2.25b)$$

$$A(0+)\partial_x u(0+, y) - A(0-)\partial_x u(0-, y) = \beta \quad \text{on } \Gamma, \quad (2.25c)$$

$$\nabla_\nu u = 0 \quad \text{on } \partial\Omega_N, \quad (2.25d)$$

$$u = u_D \quad \text{on } \partial\Omega_D. \quad (2.25e)$$

We split the solution u into the solution u_L of a linear problem and the solution u_N of a nonlinear problem so that

$$u = u_L + u_N, \quad (2.26)$$

where u_L is the solution of the problem in Lemma 2.3.1 and u_N is the solution of the boundary-value problem

$$-\nabla \cdot (A(x)\nabla u_N) + g(x, u_L + u_N) = 0 \quad \text{in } \Omega, \quad (2.27a)$$

$$\nabla_\nu u_N = 0 \quad \text{on } \partial\Omega_N, \quad (2.27b)$$

$$u_N = u_D \quad \text{on } \partial\Omega_D, \quad (2.27c)$$

which is treated in the following lemma. The use of the Leray-Schauder fixed-point theorem is similar to (Markowich et al., 1990).

Lemma 2.3.2 (Semilinear elliptic boundary-value problems with interface conditions).

Suppose that Ω , Γ , A , f , u_D , α , and β are as in Lemma 2.3.1 and additionally that f , u_D , α , and β are bounded. Suppose further

(i) that the function $g(x, u) \in C^1(\Omega \times \mathbb{R})$ is monotonically increasing in u for all $x \in \Omega$,

(ii) that there exist functions $g(u)$ and $\tilde{g}(u)$ so that

$$g(u) \leq g(x, u) \leq \tilde{g}(u) \quad \forall x \in \Omega \quad \forall u,$$

(iii) and that the algebraic equations $g(\tilde{u}) = 0$ and $\tilde{g}(\underline{u}) = 0$ have solutions.

Then there exists a unique solution $u = u_L + u_N$ of the semilinear elliptic boundary-value problem with interface conditions (2.3.1) and $u_N \in H^1(\Omega) \cap L^\infty(\Omega)$ holds. Furthermore, the solution u_N satisfies the estimate

$$\kappa \leq u_N(x) \leq \lambda \quad \forall x \in \overline{\Omega},$$

where

$$\tilde{\kappa} := \arg \max_z (g(x, z + \sup_\Omega u_L) \leq 0 \quad \forall x \in \Omega),$$

$$\kappa := \min(\tilde{\kappa}, \inf_{\partial\Omega} u_D),$$

$$\tilde{\lambda} := \arg \min_z (g(x, z + \inf_\Omega u_L) \geq 0 \quad \forall x \in \Omega),$$

$$\lambda := \max(\tilde{\lambda}, \sup_{\partial\Omega} u_D).$$

Proof. 1. To show the existence and uniqueness, we use a fixed-point theorem and a maximum principle. First, for the uniqueness of the solution, we assume that there are two weak solutions $u_1, u_2 \in H^1(\Omega) \cap L^\infty(\Omega)$. We set $w := u_1 - u_2$ and find

$$-\nabla \cdot (A(x)\nabla w) + g(x, u_1) - g(x, u_2) = 0 \quad \text{in } \Omega, \quad (2.28)$$

$$\nabla_\nu w = 0 \quad \text{on } \partial\Omega_N, \quad (2.29)$$

$$w = 0 \quad \text{on } \partial\Omega_D \quad (2.30)$$

with

$$-\nabla \cdot (A(x)\nabla w) + g(x, u_1) - g(x, u_2) = -\nabla \cdot (A(x)\nabla w) + \partial_w g(x, \hat{w}(x))w = 0 \quad (2.31)$$

using the mean-value theorem to find $\hat{w}(x)$. Since $\partial_w g(x, \hat{w}(x)) \geq 0$ by assumption, we can use the maximum principle to conclude that $w = 0$ a.e. Hence the two solutions are identical a.e.

2. To show the estimate $\kappa \leq u_N \leq \lambda$, we use a cut-off argument similar to (Jerome, 1985; Markowich, 1986). Suppose that u_N is a solution. We start by defining

$$\underline{u} := (u_N - \kappa)^- = \min(u_N - \kappa, 0), \quad (2.32)$$

$$\bar{u} := (u_N - \lambda)^+ = \max(u_N - \lambda, 0). \quad (2.33)$$

Clearly $\underline{u}, \bar{u} \in H_0^1(\Omega)$, since $u_N \in H^1(\Omega)$. The weak formulation of the problem (2.27) is

$$\langle A\nabla u_N, \nabla v \rangle + \langle g(x, u_L + u_N), v \rangle = 0 \quad \forall v \in H^1(\Omega) \quad (2.34)$$

and we will be able to use \underline{u} and \bar{u} as test functions in this equation.

Next, we estimate g on the support of \underline{u} and \bar{u} . The support of \underline{u} is $\text{supp } \underline{u} = \{x \in \bar{\Omega} \mid u_N(x) \leq \kappa\}$ and the support of \bar{u} is $\text{supp } \bar{u} = \{x \in \bar{\Omega} \mid u_N(x) \geq \lambda\}$. By the definitions of $\tilde{\kappa}$ and $\tilde{\lambda}$ and the monotonicity of g , we obtain

$$g(x, u_N + u_L) \leq g(x, \tilde{\kappa}) \leq 0 \quad \forall x \in \text{supp } \underline{u}, \quad (2.35)$$

$$g(x, u_N + u_L) \geq g(x, \tilde{\lambda}) \geq 0 \quad \forall x \in \text{supp } \bar{u}. \quad (2.36)$$

Due to the last two inequalities, the fact that $\underline{u} \leq 0$ and $\bar{u} \geq 0$ in $\bar{\Omega}$, and using the uniform ellipticity of A with constant C , we deduce from the weak formulation that

$$0 \geq \langle A\nabla u_N, \nabla \underline{u} \rangle = \langle A\nabla(u_N - \kappa), \nabla \underline{u} \rangle = \langle A\nabla(u_N - \kappa)^-, \nabla \underline{u} \rangle = \langle A\nabla \underline{u}, \nabla \underline{u} \rangle \quad (2.37)$$

$$\geq C \|\nabla \underline{u}\|_{L^2(\Omega)}^2 \geq 0 \quad (2.38)$$

and analogously

$$0 \geq \langle A\nabla u_N, \nabla \bar{u} \rangle = \langle A\nabla(u_N - \lambda), \nabla \bar{u} \rangle = \langle A\nabla(u_N - \lambda)^+, \nabla \bar{u} \rangle = \langle A\nabla \bar{u}, \nabla \bar{u} \rangle \quad (2.39)$$

$$\geq C \|\nabla \bar{u}\|_{L^2(\Omega)}^2 \geq 0. \quad (2.40)$$

Therefore $\|\nabla \underline{u}\|_{L^2(\Omega)} = 0$ and $\|\nabla \bar{u}\|_{L^2(\Omega)} = 0$ hold. Using the Poincaré inequalities $\|\underline{u}\|_{L^2} \leq C \|\nabla \underline{u}\|_{L^2}$ and $\|\bar{u}\|_{L^2} \leq C \|\nabla \bar{u}\|_{L^2}$, we find $\underline{u} = 0$ and $\bar{u} = 0$ a.e., which yields the asserted estimate.

3. To prove the existence of a solution, we define the cut function

$$v^K(x) := \begin{cases} K, & \text{if } K \leq v(x), \\ v(x), & \text{if } -K \leq v(x) \leq K, \\ -K, & \text{if } v(x) \leq -K \end{cases} \quad (2.41)$$

for $v \in L^2(\Omega)$. Obviously, we have $v^K \in L^\infty(\Omega)$. Since u_N is bounded by the estimate in the previous step, K can be chosen large enough so that $u_N = u_N^K$.

Next, we define the operator

$$M : L^2(\Omega) \times [0, 1] \rightarrow L^2(\Omega) \quad (2.42)$$

by $M(v, \sigma) = w$, where w is the solution of the boundary-value problem

$$-\nabla \cdot (A\nabla w) + \sigma g(x, u_L + v^K) = 0 \quad \text{in } \Omega, \quad (2.43)$$

$$w = \sigma u_D \quad \text{on } \partial\Omega_D, \quad (2.44)$$

$$\nabla_\nu w = 0 \quad \text{on } \partial\Omega_N. \quad (2.45)$$

Every fixed point of $M(\cdot, 1)$ is a solution of the semilinear problem (2.27). Due to the estimate shown in the previous step, K can be chosen large enough so that $-K \leq w \leq K$ holds a.e. in Ω for every fixed point $w = M(w, 1)$.

To apply the Leray-Schauder fixed-point theorem (Appendix B, Theorem B.1), the compactness of M must be shown. The continuity of M follows from the continuity of the cut function, the continuous dependence of $\sigma g(x, u_L + v^K)$ on $(v, \sigma) \in L^2(\Omega) \times [0, 1]$, and the continuous dependence of the H^1 solutions of elliptic equations on $L^2(\Omega)$ right-hand sides and H^1 boundary data. Furthermore, the range of M is bounded with respect to the H^1 norm, since w is the solution of a linear elliptic equation with the inhomogeneity $g(x, u_L + v^K)$ that is bounded because g is bounded as a function of x and both u_L and v^K are bounded, i.e., the inequality

$$\|w\|_{H^1(\Omega)} \leq C(\|\sigma g(\cdot, u_L + v^K)\|_{L^2(\Omega)} + \|\sigma u_D\|_{H^{1/2}(\partial\Omega)}) \quad (2.46)$$

$$\leq C(|\Omega|^{1/2} \sup_{x \in \Omega} |g(x, u_L + K)| + \|u_D\|_{H^{1/2}(\partial\Omega)}), \quad (2.47)$$

holds. We know that $H^1(\Omega)$ is compactly embedded in $L^2(\Omega)$ due to the Rellich-Kondrachov compactness theorem (Appendix B, Theorem B.3). Since the range of M is bounded, the operator M is compact.

Finally, the Leray-Schauder fixed-point theorem (Appendix B, Theorem B.1) yields the existence of a fixed point w of $M(\cdot, 1)$ and hence the existence of a solution u_N of the original boundary-value problem. \square

2.4 Proof of the Existence Theorem 2.2.2

The following proof of Theorem 2.2.2 is based on the Schauder fixed-point theorem and the estimates are deduced from a maximum principle (see Lemma 2.3.2). The main idea of the proof follows (Markowich, 1986), while the emphasis is on the different fixed-point map and the different estimates.

1. We start by defining the map $G : N \rightarrow N$, which will be shown to satisfy the assumptions of the fixed-point theorem, where

$$N := \left\{ (V, u, v, \alpha, \beta) \in L^2(\Omega) \times L^2(\Omega_{\text{Si}})^2 \times L^2(\Gamma)^2 \mid \underline{V} \leq V(x) \leq \overline{V} \text{ a.e. in } \Omega, \right. \\ \left. \frac{1}{K} \leq u(x), v(x) \leq K \text{ a.e. in } \Omega_{\text{Si}}, \quad \alpha, \beta \text{ bounded a.e. on } \Gamma \right\} \quad (2.48)$$

and $(V_1, u_1, v_1, \alpha_1, \beta_1) = G((V_0, u_0, v_0, \alpha_0, \beta_0))$ as follows.

(i) Solve the boundary-value problem with interface conditions

$$-\nabla \cdot (A \nabla V_1) = \begin{cases} qC_{\text{dop}} - qn_i(e^{V_1/U_T} u_0 - e^{-V_1/U_T} v_0) & \text{in } \Omega_{\text{Si}}, \\ 0 & \text{in } \Omega_{\text{ox}}, \\ -2\eta \sinh(\xi(V_1 - \Phi)) & \text{in } \Omega_{\text{liq}}, \end{cases} \quad (2.49a)$$

$$V_1(0+, y) - V_1(0-, y) = \alpha_0(y) \quad \text{on } \Gamma, \quad (2.49b)$$

$$A(0+)\partial_x V_1(0+, y) - A(0-)\partial_x V_1(0-, y) = \beta_0(y) \quad \text{on } \Gamma, \quad (2.49c)$$

$$V_1 = V_D \quad \text{on } \partial\Omega_D, \quad (2.49d)$$

$$\nabla_\nu V_1 = 0 \quad \text{on } \partial\Omega_N \quad (2.49e)$$

for V_1 .

(ii) Solve the elliptic boundary-value problem

$$U_T n_i \nabla \cdot (\mu_n e^{V_1/U_T} \nabla u_1) - n_i \frac{u_1 v_0 - 1}{\tau_p(e^{V_1/U_T} u_0 + 1) + \tau_n(e^{-V_1/U_T} v_0 + 1)} = 0 \quad \text{in } \Omega_{\text{Si}}, \quad (2.50a)$$

$$u_1 = u_D \quad \text{on } \partial\Omega_D, \quad (2.50b)$$

$$\nabla_\nu u_1 = 0 \quad \text{on } \partial\Omega_N \quad (2.50c)$$

for u_1 .

(iii) Solve the elliptic problem

$$U_T n_i \nabla \cdot (\mu_p e^{-V_1/U_T} \nabla v_1) - n_i \frac{u_0 v_1 - 1}{\tau_p(e^{V_1/U_T} u_0 + 1) + \tau_n(e^{-V_1/U_T} v_0 + 1)} = 0 \quad \text{in } \Omega_{\text{Si}}, \quad (2.51a)$$

$$v_1 = v_D \quad \text{on } \partial\Omega_D, \quad (2.51b)$$

$$\nabla_\nu v_1 = 0 \quad \text{on } \partial\Omega_N \quad (2.51c)$$

for v_1 .

(iv) Update the surface-charge density and dipole-moment density according to the microscopic model as

$$\alpha_1(y) := M_\alpha(V_1), \quad (2.52a)$$

$$\beta_1(y) := M_\beta(V_1). \quad (2.52b)$$

We show that these three boundary-value problems have unique solutions and that $(V_1, u_1, v_1, \alpha_1, \beta_1) \in N$ so that the map G is well-defined. The three problems above can be written in the general form considered in Lemma 2.3.2 and the first problem (2.49) includes interface conditions. The coefficient A in the lemma equals either A , $\mu_n e^{V_1/U_T}$, or $\mu_p e^{-V_1/U_T}$ and hence the equations are uniformly elliptic. In all three cases, $g(x, w)$ is a monotone increasing function of w provided that u_0 and v_0 are positive.

Choose $(V, u_0, v_0, \alpha_0, \beta_0) \in N$. Lemma 2.3.2 shows that the first problem (2.49) in the definition of G has a unique solution V_1 . To get the estimates, we first set

$$\underline{g}(V_1) := \min(2\eta \sinh(\xi(V_1 - \Phi)), qn_i(\frac{1}{K}e^{V_1/U_T} - Ke^{-V_1/U_T}) - q\overline{C}), \quad (2.53)$$

$$\tilde{g}(V_1) := \max(2\eta \sinh(\xi(V_1 - \Phi)), qn_i(Ke^{V_1/U_T} - \frac{1}{K}e^{-V_1/U_T}) - q\underline{C}) \quad (2.54)$$

and both \underline{g} and \tilde{g} satisfy the requirements of Lemma 2.3.2. Solving the two algebraic equations

$$\tilde{g}(\tilde{\kappa} + \sup_{\Omega} V_L) = 0, \quad (2.55)$$

$$\underline{g}(\tilde{\lambda} + \inf_{\Omega} V_L) = 0, \quad (2.56)$$

where V_L is the solution of the linear boundary-value problem of Lemma 2.3.1, yields

$$\tilde{\kappa} + \sup_{\Omega} V_L = \min\left(\Phi, U_T \ln\left(\frac{1}{2Kn_i}\left(\underline{C} + \sqrt{\underline{C}^2 + 4n_i^2}\right)\right)\right), \quad (2.57)$$

$$\tilde{\lambda} + \inf_{\Omega} V_L = \max\left(\Phi, U_T \ln\left(\frac{K}{2n_i}\left(\overline{C} + \sqrt{\overline{C}^2 + 4n_i^2}\right)\right)\right). \quad (2.58)$$

Hence we obtain the estimate

$$V(x) \geq \min\left(\inf_{\partial\Omega_D} V_D, \Phi - \sup_{\Omega} V_L, U_T \ln\left(\frac{1}{2Kn_i}\left(\underline{C} + \sqrt{\underline{C}^2 + 4n_i^2}\right)\right) - \sup_{\Omega} V_L\right), \quad (2.59)$$

$$V(x) \leq \max\left(\sup_{\partial\Omega_D} V_D, \Phi - \inf_{\Omega} V_L, U_T \ln\left(\frac{K}{2n_i}\left(\overline{C} + \sqrt{\overline{C}^2 + 4n_i^2}\right)\right) - \inf_{\Omega} V_L\right) \quad (2.60)$$

for all $x \in \Omega$ from Lemma 2.3.2.

Next, we apply Lemma 2.3.2 to the second problem (2.50) to find a unique solution u_1 . Here we choose

$$\underline{g}(u_1) := \frac{\frac{1}{K}u_1 - 1}{\tau_p(Ke^{\overline{V}/U_T} + 1) + \tau_n(Ke^{-\overline{V}/U_T} + 1)}, \quad (2.61)$$

$$\tilde{g}(u_1) := \frac{Ku_1 - 1}{\tau_p(\frac{1}{K}e^{\underline{V}/U_T} + 1) + \tau_n(\frac{1}{K}e^{-\underline{V}/U_T} + 1)}. \quad (2.62)$$

The equation $\underline{g}(\tilde{u}_1) = 0$ yields $\tilde{u}_1 = K$ and the equation $\tilde{g}(\underline{u}_1) = 0$ yields $\underline{u}_1 = 1/K$.

The third problem (2.51) is treated analogously and we find unique solutions u_1 and v_1 with the estimates $1/K \leq u_1(x) \leq K$ and $1/K \leq v_1 \leq K$ on Ω_{Si} . Hence G maps N into itself. Note that N is a closed and convex subset of $L^2(\Omega) \times L^2(\Omega_{Si})^2 \times L^2(\Gamma)^2$.

2. We now show that G is continuous. The continuous dependence of the solution V_1 of the first problem (2.49) in the definition of G on the data is obtained from the estimate in Lemma 2.3.2 and the continuity of the right-hand side in (2.49a). The second problem (2.50) and the third problem (2.51) in the definition of G are special cases of the first. In the fourth problem (2.52), α_1 and β_1 depend continuously on α_0 and β_0 due to the continuous dependence of V_1 and the continuity of M_α and M_β . Therefore G is continuous.

3. The continuous dependence of $(V_1, u_1, v_1, \alpha_1, \beta_1)$ on the data of the three problems (2.49), (2.50), and (2.51) implies that there is a positive and continuous function F such that

$$\begin{aligned} & \|V_1\|_{H^1(\Omega)} + \|u_1\|_{H^1(\Omega_{\text{Si}})} + \|v_1\|_{H^1(\Omega_{\text{Si}})} \\ & \leq F(\|C_{\text{dop}}\|_{L^2(\Omega)}, \|V_D\|_{H^1(\partial\Omega)}, \|u_D\|_{H^1(\partial\Omega_{\text{Si}})}, \|v_D\|_{H^1(\partial\Omega_{\text{Si}})}, \|\alpha_0\|_{H^{1/2}(\Gamma)}, \|\beta_0\|_{L^2(\Gamma)}). \end{aligned} \quad (2.63)$$

Hence we find for $(V_0, u_0, v_0, \alpha_0, \beta_0) \in N$ that the inequality

$$\|V_1\|_{H^1(\Omega)} + \|u_1\|_{H^1(\Omega_{\text{Si}})} + \|v_1\|_{H^1(\Omega_{\text{Si}})} \leq C \quad (2.64)$$

holds for a constant C . Furthermore, $\|\alpha_1\|_{H^1(\Gamma)}$ and $\|\beta_1\|_{H^1(\Gamma)}$ are bounded due to the assumptions on M_α and M_β .

This yields that the image $G(N)$, consisting of all $(V_1, u_1, v_1, \alpha_1, \beta_1)$, is bounded as a subset of $H^1(\Omega) \times H^1(\Omega_{\text{Si}})^2 \times H^1(\Gamma)^2$. Now the Rellich-Kondrachov compactness theorem (Appendix B, Theorem B.3) implies that the image $G(N)$ is precompact in $L^2(\Omega) \times L^2(\Omega_{\text{Si}})^2 \times L^2(\Gamma)^2$.

4. In summary, all the assumptions of the Schauder fixed-point theorem (Appendix B, Theorem B.2) are satisfied and hence we obtain the existence of a fixed-point of G , i.e., the existence of a weak solution of the original problem.

2.5 Local Uniqueness Theorem

In general, the solution in Theorem 2.2.2 is not unique. Recalling the derivation of the drift-diffusion equations from the Boltzmann transport equation, it is clear that the drift-diffusion equations implicitly assume that the particle velocities are distributed according to a Maxwellian distribution, i.e., they are in thermal equilibrium. However, large applied voltages and correspondingly large currents result in fast particles for which Maxwellian distributions centered at $v = 0$ are certainly not adequate.

Uniqueness of the solution therefore holds only in a neighborhood around thermal equilibrium with respect to the Dirichlet boundary conditions. Thermal equilibrium is the solution where the fluxes J_n and J_p in the semiconductor vanish, where the fluxes of the ions and molecules into and out of the boundary layer at the sensor surface vanish as well, i.e., the surface reactions have reached the equilibrium state, and where the voltages $U \in \mathbb{R}^k$, that are applied at each of the k contacts that constitute $\partial\Omega_D$, are equal to the Fermi level.

The equilibrium potential is called V_e and the equilibrium surface densities are called α_e and β_e ;

the equilibrium potential is then the solution of the equilibrium boundary-value problem

$$-\nabla \cdot (A\nabla V_e) = qC_{\text{dop}} - qn_i(e^{V_e/U_T} - e^{-V_e/U_T}) \quad \text{in } \Omega_{\text{Si}}, \quad (2.65a)$$

$$-\nabla \cdot (A\nabla V_e) = 0 \quad \text{in } \Omega_{\text{ox}}, \quad (2.65b)$$

$$-\nabla \cdot (A\nabla V_e) = -2\eta \sinh(\xi(V_e - \Phi)) \quad \text{in } \Omega_{\text{liq}}, \quad (2.65c)$$

$$V_e(0+, y) - V_e(0-, y) = \alpha_e \quad \text{on } \Gamma, \quad (2.65d)$$

$$A(0+)\partial_x V_e(0+, y) - A(0-)\partial_x V_e(0-, y) = \beta_e \quad \text{on } \Gamma, \quad (2.65e)$$

$$V_e = V_D(0) \quad \text{on } \partial\Omega_D, \quad (2.65f)$$

$$\nabla_\nu V_e = 0 \quad \text{on } \partial\Omega_N \quad (2.65g)$$

and it exists uniquely due to Lemma 2.3.2.

In order to state the uniqueness result, we need the following assumptions on the data.

Assumptions 2.5.1.

- (i) The recombination rate R has the form $R = F(x, V, u, v)(uv - 1)$, where $F(x, \dots) \in C^2(\mathbb{R} \times \mathbb{R}_+^2)$ holds for all $x \in \Omega$ and where the derivatives $\partial_{(V, u, v)}^\kappa F(\cdot, V, u, v)$ are in $L^\infty(\Omega)$ uniformly for all (V, u, v) in bounded subsets of $\mathbb{R} \times \mathbb{R}_+^2$ and for all multiindices κ with $|\kappa| \leq 2$.

Furthermore, there are constants $\underline{\omega}$ and $\bar{\omega}$ such that either $0 < \underline{\omega} \leq F(x, V_e(x), 1, 1) \leq \bar{\omega}$ or $F(x, V_e(x), 1, 1) = 0$ holds for all $x \in \Omega$.

- (ii) The Dirichlet data (V_D, u_D, v_D) are a Lipschitz-continuously differentiable map of U from \mathbb{R}^k into $H^2(\Omega) \times H^2(\Omega_{\text{Si}})^2$ and $u_D(0) = v_D(0) = 1$ holds in Ω_{Si} .

- (iii) The solution u of the boundary-value problem $-\nabla \cdot (A\nabla u) = f$ in Ω , $u = 0$ on $\partial\Omega_D$, and $\nabla_\nu u = 0$ on $\partial\Omega_N$, satisfies the inequality

$$\|u\|_{W^{2,q}(\Omega)} \leq C\|f\|_{L^q(\Omega)}$$

for all $f \in L^q(\Omega)$ with $q = 2$ and $q = 3/2$. This is actually a condition on the boundary segments $\partial\Omega_D$ and $\partial\Omega_N$; it excludes boundaries where Dirichlet and Neumann segments meet under angles larger than $\pi/2$.

- (iv) The Fréchet derivatives M'_α and M'_β of the interface models M_α and M_β with respect to V exist, they are in $H^{1/2}(\Gamma)$ and $L^2(\Gamma)$, respectively, and they satisfy the inequality

$$\|M'_\alpha(V)\|_{H^{1/2}(\Gamma)} + \|M'_\beta(V)\|_{L^2(\Gamma)} \leq C\|V\|_{H^2(\Omega)}$$

in a neighborhood of the equilibrium potential V_e with a sufficiently small constant C .

The following theorem yields the local uniqueness of the solution of (2.13). The proof is based on the implicit-function theorem.

Theorem 2.5.2 (Local uniqueness).

Under Assumptions 2.2.1 and 2.5.1, there exists a sufficiently small $\sigma \in \mathbb{R}$ with $|U| < \sigma$ such that the problem in Theorem 2.2.2 has a locally unique solution

$$(V^*(U), u^*(U), v^*(U), \alpha^*(U), \beta^*(U)) \in H^2(\Omega) \times H^2(\Omega_{\text{Si}})^2 \times H^{1/2}(\Gamma) \times L^2(\Gamma).$$

The solution satisfies

$$(V^*(0), u^*(0), v^*(0), \alpha^*(0), \beta^*(0)) = (V_e, 1, 1, \alpha_e, \beta_e)$$

and it depends continuously differentiably on U as a map from $\{U \in \mathbb{R}^k \mid |U| < \sigma\}$ into $H^2(\Omega) \times H^2(\Omega_{\text{Si}})^2 \times H^{1/2}(\Gamma) \times L^2(\Gamma)$.

Proof. 1. We start with the substitution $\tilde{V} := V - V_D(U)$, $\tilde{u} := u - u_D(U)$, and $\tilde{v} := v - v_D(U)$. For notational simplicity, we denote \tilde{V} , \tilde{u} , and \tilde{v} again by V , u , and v . After the substitution, the system (2.13) becomes

$$\begin{aligned} -\nabla \cdot (A\nabla(V + V_D)) & & & \\ & = qC_{\text{dop}} - qn_i(e^{(V+V_D)/U_T}u - e^{-(V+V_D)/U_T}v) & \text{in } \Omega_{\text{Si}}, \\ -\nabla \cdot (A\nabla(V + V_D)) & = 0 & \text{in } \Omega_{\text{ox}}, \\ -\nabla \cdot (A\nabla(V + V_D)) & = -2\eta \sinh(\xi(V + V_D - \Phi)) & \text{in } \Omega_{\text{liq}}, \\ V(0+, y) - V(0-, y) & = \alpha & \text{on } \Gamma, \\ A(0+)\partial_x V(0+, y) - A(0-)\partial_x V(0-, y) & = \beta & \text{on } \Gamma, \\ U_T n_i \nabla \cdot (\mu_n e^{(V+V_D)/U_T} \nabla(u + u_D)) & & \\ & = F(x, V + V_D, u + u_D, v + v_D)((u + u_D)(v + v_D) - 1) & \text{in } \Omega_{\text{Si}}, \\ U_T n_i \nabla \cdot (\mu_p e^{-(V+V_D)/U_T} \nabla(v + v_D)) & & \\ & = F(x, V + V_D, u + u_D, v + v_D)((u + u_D)(v + v_D) - 1) & \text{in } \Omega_{\text{Si}}, \\ & \alpha = M_\alpha(V) & \text{on } \Gamma, \\ & \beta = M_\beta(V) & \text{on } \Gamma, \\ & V = 0 & \text{on } \partial\Omega_D, \\ & u = v = 0 & \text{on } \partial\Omega_{D,\text{Si}}, \\ & \nabla_\nu V = 0 & \text{on } \partial\Omega_N, \\ & \nabla_\nu u = \nabla_\nu v = 0 & \text{on } \partial\Omega_{N,\text{Si}}. \end{aligned}$$

We write this boundary-value problem as the operator equation

$$G(V, u, v, \alpha, \beta, U) = 0, \tag{2.66}$$

where the map

$$G : B \times S_{\sigma_1}(0) \rightarrow L^2(\Omega) \times L^2(\Omega_{\text{Si}})^2 \times H^{1/2}(\Gamma) \times L^2(\Gamma) \tag{2.67}$$

is given by the boundary-value problem above. Here B is an open subset of $H^2_\partial(\Omega \setminus \Gamma) \times H^2_\partial(\Omega_{\text{Si}})^2 \times H^{1/2}(\Gamma) \times L^2(\Gamma)$ with

$$H^2_\partial(\Omega) := \{\phi \in H^2(\Omega) \mid \nabla_\nu \phi = 0 \text{ on } \partial\Omega_N, \quad \phi = 0 \text{ on } \partial\Omega_D\} \tag{2.68}$$

and the sphere $S_{\sigma_1}(0)$ with radius σ_1 and center 0 is a subset of \mathbb{R}^k . The domain must be chosen such that $u = \tilde{u} + u_D > 0$ and $v = \tilde{v} + v_D > 0$ for all $(V, u, v, \alpha, \beta) \in B$ and for all $U \in S_{\sigma_1}(0)$, because u and v are positive and the recombination rate R is defined only for positive u and v .

Since $u_D(0) = 1$ (this is the boundary condition for $U = 0$ of the equilibrium solution), we have to ensure that $\|\tilde{u}\|_{L^\infty(\Omega_{\text{Si}})}$ is small enough so that u is positive. To ensure this, we choose B bounded and small enough; if $\|\tilde{u}\|_{H^2(\Omega_{\text{Si}})}$ is small enough, this indeed implies that $\|\tilde{u}\|_{L^\infty(\Omega_{\text{Si}})}$ is small enough due to the inequality $\|u\|_{L^\infty(U)} \leq C\|u\|_{H^2(U)}$ for all $f \in H^2(U)$. The same argument ensures that v is positive if B is bounded and small enough.

Since $G(V, u, v, \alpha, \beta, U) \in L^2(\Omega) \times L^2(\Omega_{\text{Si}})^2 \times H^{1/2}(\Gamma) \times L^2(\Gamma)$ implies that $(V, u, v, \alpha, \beta) \in B$ and $U \in S_{\sigma_1}(U)$ and since products of functions in B are in $L^2(\Omega)$ due to the inequality $\|uv\|_{L^2(U)} \leq C\|u\|_{H^1(U)}\|v\|_{H^1(U)}$ for all u and $v \in H^1(U)$, the map G , as stated in (2.67), is well-defined.

2. The equilibrium solution $(V_e - V_D(0), 0, 0, \alpha_e, \beta_e, 0)$ is obviously a solution of the equation $G = 0$. To apply the implicit-function theorem, the Fréchet derivative

$$D_{(V,u,v,\alpha,\beta)}G(V_e - V_D(0), 0, 0, \alpha_e, \beta_e, 0) \quad (2.69)$$

must have a bounded inverse. To find the inverse of the Fréchet derivative, we solve the equation

$$D_{(V,u,v,\alpha,\beta)}G(V_e - V_D(0), 0, 0, \alpha_e, \beta_e, 0)(a_1, a_2, a_3, a_4, a_5) = (g_1, g_2, g_3, g_4, g_5) \quad (2.70)$$

for a_i , where $(g_1, g_2, g_3, g_4, g_5) \in L^2(\Omega) \times L^2(\Omega_{\text{Si}})^2 \times H^{1/2}(\Gamma) \times L^2(\Gamma)$. This equation is equivalent to the boundary-value problem

$$\begin{aligned} -\nabla \cdot (A\nabla a_1) &= -qn_i \left(\frac{e^{V_e/U_T} + e^{-V_e/U_T}}{U_T} \right) a_1 \\ &\quad + e^{-V_e/U_T} a_2 - e^{V_e/U_T} a_3 + g_1 \quad \text{in } \Omega_{\text{Si}}, \end{aligned} \quad (2.71a)$$

$$-\nabla \cdot (A\nabla a_1) = g_1 \quad \text{in } \Omega_{\text{ox}}, \quad (2.71b)$$

$$-\nabla \cdot (A\nabla a_1) = -2\eta\beta \sinh(\xi(V_e - \Phi))a_1 + g_1 \quad \text{in } \Omega_{\text{liq}}, \quad (2.71c)$$

$$a_1(0+, y) - a_1(0-, y) = a_4 \quad \text{on } \Gamma, \quad (2.71d)$$

$$A(0+)\partial_x a_1(0+, y) - A(0-)\partial_x a_1(0-, y) = a_5 \quad \text{on } \Gamma, \quad (2.71e)$$

$$n_i \nabla \cdot (\mu_n e^{V_e/U_T} \nabla a_2) = \omega(x)a_2 + \omega(x)a_3 + g_2 \quad \text{in } \Omega_{\text{Si}}, \quad (2.71f)$$

$$n_i \nabla \cdot (\mu_p e^{-V_e/U_T} \nabla a_3) = \omega(x)a_2 + \omega(x)a_3 + g_3 \quad \text{in } \Omega_{\text{Si}}, \quad (2.71g)$$

$$a_4 = M'_\alpha(V_e)a_1 + g_4 \quad \text{on } \Gamma, \quad (2.71h)$$

$$a_5 = M'_\beta(V_e)a_1 + g_5 \quad \text{on } \Gamma, \quad (2.71i)$$

$$a_1 = 0 \quad \text{on } \partial\Omega_D, \quad (2.71j)$$

$$a_2 = a_3 = 0 \quad \text{on } \partial\Omega_{D,\text{Si}}, \quad (2.71k)$$

$$\nabla_\nu a_1 = 0 \quad \text{on } \partial\Omega_N, \quad (2.71l)$$

$$\nabla_\nu a_2 = \nabla_\nu a_3 = 0 \quad \text{on } \partial\Omega_{N,\text{Si}}, \quad (2.71m)$$

where $\omega(x) := F(x, V_e(x), 1, 1)$ and either $0 < \underline{\omega} \leq f(x) \leq \bar{\omega}$ or $\omega = 0$ holds in Ω_{Si} due to the assumptions on the recombination rate.

In the case $\omega = 0$ in Ω , the equations (2.71f) and (2.71g) are decoupled from the first equation and from each other. Hence the existence of a unique solution and the boundedness of the inverse are seen immediately.

In the case $0 < \underline{\omega} \leq f(x) \leq \bar{\omega}$ in Ω_{Si} , the unique existence of the solutions a_2 and a_3 of the equations (2.71f) and (2.71g) are shown as in the proof of Theorem 3.3.1 in (Markowich, 1986).

In both cases, the estimate

$$\|a_2\|_{H^2(\Omega_{\text{Si}})} + \|a_3\|_{H^2(\Omega_{\text{Si}})} \leq C(\|g_2\|_{L^2(\Omega_{\text{Si}})} + \|g_3\|_{L^2(\Omega_{\text{Si}})}) \quad (2.72)$$

holds.

3. By substituting a_2 and a_3 into (2.71a), we find the estimate

$$\begin{aligned} \|a_1\|_{H^2(\Omega)} \leq C_1(\|g_1\|_{L^2(\Omega)} + \|g_2\|_{L^2(\Omega_{\text{Si}})} + \|g_3\|_{L^2(\Omega_{\text{Si}})} + \|g_4\|_{H^{1/2}(\Gamma)} + \|g_5\|_{L^2(\Gamma)} \\ + \|a_4\|_{H^{1/2}(\Gamma)} + \|a_5\|_{L^2(\Gamma)}) \end{aligned} \quad (2.73)$$

using Lemma 2.3.1. Equations (2.71h) and (2.71i) and assumption 2.5.1(iv) on M_α and M_γ yields the existence of a sufficiently small constant C_2 such that the inequality

$$\|a_4\|_{H^{1/2}(\Gamma)} + \|a_5\|_{L^2(\Gamma)} \leq C_2\|a_1\|_{H^2(\Omega)} + \|g_4\|_{H^{1/2}(\Gamma)} + \|g_5\|_{L^2(\Gamma)} \quad (2.74)$$

holds. For sufficiently small C_2 , i.e., if $C_1C_2 < 1$, the last two inequalities yield

$$\begin{aligned} (1 - C_1C_2)\|a_1\|_{H^2(\Omega)} \leq C_1(\|g_1\|_{L^2(\Omega)} + \|g_2\|_{L^2(\Omega_{\text{Si}})} + \|g_3\|_{L^2(\Omega_{\text{Si}})} \\ + 2\|g_4\|_{H^{1/2}(\Gamma)} + 2\|g_5\|_{L^2(\Gamma)}). \end{aligned} \quad (2.75)$$

Hence we have shown that the Fréchet derivative has a bounded inverse, i.e., there is a constant C such that the inequality

$$\|(D_{(V,u,v,\alpha,\beta)}G(V_e - V_D(0), 0, 0, \alpha_e, \beta_e, 0))^{-1}\| \leq C \quad (2.76)$$

holds, where the norm is the operator norm of

$$L^2(\Omega) \times L^2(\Omega_{\text{Si}})^2 \times H^{1/2}(\Gamma) \times L^2(\Gamma) \rightarrow H^2(\Omega \setminus \Gamma) \times H^2(\Omega_{\text{Si}})^2 \times H^{1/2}(\Gamma) \times L^2(\Gamma). \quad (2.77)$$

Finally, the implicit-function theorem (Appendix B, Theorem B.4) yields the assertion. \square

2.6 Summary

The here observed PDE system serves as a model for the self-consistent simulation of field-effect sensors such as bio- and gas sensors and is based on the drift-diffusion equations and the Poisson-Boltzmann equation. Additionally two interface conditions for the electric potential and the electric displacement are implemented. From previous studies it is known that the drift-diffusion equations have a solution which is unique around thermal equilibrium.

We showed that this properties are still valid for the system of equations including the jump conditions. Therefore we firstly proved existence of a solution of elliptic boundary-value problems

with interface conditions and a estimate for the solution of it. Here the jump conditions affect the estimate of the solution comparable to Dirichlet and Neumann boundary conditions.

With this result the existence of a solution of semilinear elliptic boundary-value problems with interface conditions and a estimate for the solution were proved. Using these two lemmata, the Rellich-Kondrachov compactness theorem, and the Leray-Schauder fixed-point theorem the existence of a solution of our system of equations including jump conditions satisfying reasonable assumptions is obtained.

Starting with an equilibrium solution for our system of equations by assuming equilibrium interface conditions we proved uniqueness around this thermal equilibrium by an implicit function theorem. Summarized all properties of the drift-diffusion equations remain valid assuming reasonable conditions for the jumps at the interface.

Since the analysis for our system of equations is now completed we turn to the numerics and especially to the parallelization algorithm based on the FETI method.

A One Level FETI Method

THE FETI (finite element tearing and interconnect) and Neumann-Neumann algorithms are the best known and most tested domain-decomposition methods for elliptic partial differential equations (Toselli and Widlund, 2005). They are suitable for Dirichlet and Neumann boundary-value problems as well as for highly heterogeneous equations, show a high scalability, and are applicable for computations with a large number of processors (Bhardwaj et al., 1999; Klawonn and Widlund, 2001). Consequently many variants (Dostál et al., 2006; Farhat et al., 2001) have been developed for different applications (Avery et al., 2004; Dureisseix and Farhat, 2001; Farhat et al., 2005; Toselli and Klawonn, 2002). In this chapter we extend the field of applications to our system of partial differential equations (1.28). With the extensions developed in this chapter, namely the consideration of a self-consistent system, the inclusion of discontinuities at an interface, and the Poisson-Boltzmann equation in a subdomain, it is possible to simulate NWFET devices, with a geometry as in Fig. 1.6, in parallel.

Therefore, the convergence of the FETI method and the condition-number estimate, are stated in Section 3.2. The extension of the FETI scheme to the model equations is given in Section 3.3. The scheme is based on the one-level FETI method according to the work by *Farhat* and *Roux* (Farhat and Roux, 1991).

Three examples for the method are presented in Section 3.4 to show that simulation of NWFET devices with this algorithm is the best approach. The first example shows the use of constant interface conditions in two spatial dimensions. The second example is the simulation of the half of a nanowire sensor, to show the right implementation of the different materials and the correct implementation even in the cases when the material interfaces are corners. The third example is based on the geometry of a real NWFET device. Only the length scales are chosen to be small to simplify the description. Here we also tested different preconditioners. All the calculations are done fully self consistently by the following algorithm.

3.1 Self-Consistent Loop

We are going to parallelize the system (1.28) numerically. Therefore we use the Scharfetter-Gummel iteration scheme which consists of three steps: the derivation of the electrostatic potential V , of the electron density n , and of the hole density p . The dipole moment density and the surface charge density are included in this scheme by adding the derivation of the boundary layer charge which is dependent on the surface potential. The first iteration with initial values n_0, p_0, α_0 , and β_0 works as follows:

1. Solve the boundary-value problem with interface conditions

$$-\nabla \cdot (\varepsilon \nabla V_1) = \begin{cases} q(p_0 - n_0 + C_{\text{dop}}) & \text{in } \Omega_{\text{Si}}, \\ 0 & \text{in } \Omega_{\text{ox}}, \\ -2\eta \sinh(\xi V_1) & \text{in } \Omega_{\text{liq}}, \end{cases}$$

$$\begin{aligned} V_1(0+, \mathbf{y}) - V_1(0-, \mathbf{y}) &= \alpha_0(\mathbf{y}) && \text{on } \Gamma, \\ \varepsilon(0+) \partial_{x_1} V_1(0+, \mathbf{y}) - \varepsilon(0-) \partial_{x_1} V_1(0-, \mathbf{y}) &= \beta_0(\mathbf{y}) && \text{on } \Gamma, \\ V_1 &= V_D && \text{on } \partial\Omega_D, \\ \nabla_\nu V_1 &= 0 && \text{on } \partial\Omega_N \end{aligned}$$

for V_1 .

2. Solve the elliptic boundary-value problem

$$\begin{aligned} \nabla \cdot (D_n \nabla n_1 - \mu_n n_1 \nabla V) &= \frac{n_1 p_0 - n_i^2}{\tau_p(n_1 + n_i) + \tau_n(p_0 + n_i)} && \text{in } \Omega_{\text{Si}}, \\ n_1 &= n_D && \text{on } \partial\Omega_D, \\ \nabla_\nu n_1 &= 0 && \text{on } \partial\Omega_N \end{aligned}$$

for n_1 . Here the n_1 in the denominator can be replaced by n_0 which makes the discretized system linear.

3. Solve the elliptic boundary-value problem

$$\begin{aligned} \nabla \cdot (D_p \nabla p_1 + \mu_p p_1 \nabla V) &= \frac{n_1 p_1 - n_i^2}{\tau_p(n_1 + n_i) + \tau_n(p_1 + n_i)} && \text{in } \Omega_{\text{Si}}, \\ p_1 &= p_D && \text{on } \partial\Omega_D, \\ \nabla_\nu p_1 &= 0 && \text{on } \partial\Omega_N \end{aligned}$$

for p_1 .

4. Update the surface-charge density and dipole-moment density according to a boundary model

$$\begin{aligned} \alpha_1(\mathbf{y}) &:= M_\alpha(V_1), \\ \beta_1(\mathbf{y}) &:= M_\beta(V_1), \end{aligned}$$

where M_α and M_β are the functions giving the densities according to the surface potentials. In the case of Monte-Carlo simulations, this can be done by generating a look-up table with density values for different surface voltages.

It should be mentioned that we can rewrite all the equations in the self consistent loop, especially the drift-diffusion equations, to the general form

$$\nabla \cdot (c_1(w)\nabla w) + \nabla \cdot (w\mathbf{c}_2(w)) + f(w) = 0, \quad (3.5)$$

where c_1 is a constant and \mathbf{c}_2 is a vector with constant components in both cases $w = n$ and $w = p$. Furthermore f is a linearized version of the recombination rate. Since the FETI method is applicable for equations of this type this shows how it can be applied away from the interface Γ . At the interface Γ , the Lagrangians must be modified because of the interface conditions (1.2b) and (1.2c). The detailed description follows in the next section.

3.2 The FETI algorithm

In order to describe the FETI algorithm, the coefficients and boundary conditions of the problem

$$-\nabla \cdot (\varepsilon(x, y, z)\nabla V(x, y, z)) = \begin{cases} q(p - n + C_{\text{dop}}) & \text{in } \Omega_1, \\ 0 & \text{in } \Omega_2, \end{cases} \quad (3.6a)$$

$$\nabla \cdot (D_n\nabla n - \mu_n n \nabla V) = \frac{np - n_i^2}{\tau_p(n + n_i) + \tau_n(p + n_i)} \quad \text{in } \Omega_1, \quad (3.6b)$$

$$\nabla \cdot (D_p\nabla p + \mu_p p \nabla V) = \frac{np - n_i^2}{\tau_p(n + n_i) + \tau_n(p + n_i)} \quad \text{in } \Omega_1, \quad (3.6c)$$

with the discontinuities

$$V(0+, y, z) - V(0-, y, z) = \alpha(y, z) \quad \text{on } \Gamma, \quad (3.7a)$$

$$\varepsilon_+ \partial_x V(0+, y, z) - \varepsilon_- \partial_x V(0-, y, z) = \beta(y, z) \quad \text{on } \Gamma, \quad (3.7b)$$

must satisfy the following assumptions (cf. Assumptions 2.2.1 or (Baumgartner and Heitzinger, 2012a)).

Assumptions 3.2.1.

(i) The bounded domain $\Omega \subset \mathbb{R}^3$ has a C^2 Dirichlet boundary $\partial\Omega_D$, the Neumann boundary $\partial\Omega_N$ consists of C^2 segments, and the Lebesgue measure of the Dirichlet boundary $\partial\Omega_D$ is nonzero.

The C^2 hypersurface $\Gamma \subset \Omega$ splits the domain Ω into two nonempty domains Ω^+ and Ω^- so that $\text{meas}(\Gamma \cap \partial\Omega) = 0$ and $\Gamma \cap \partial\Omega \subset \partial\Omega_N$ hold.

(ii) The coefficient functions ε , μ_n , and μ_p are uniformly elliptic and bounded with $\varepsilon|_{\Omega^+} \in C^1(\Omega^+, \mathbb{R}^{3 \times 3})$, $\varepsilon|_{\Omega^-} \in C^1(\Omega^-, \mathbb{R}^{3 \times 3})$, and $\mu_n, \mu_p \in C^1(\Omega_{\text{Si}}, \mathbb{R}^{3 \times 3})$.

For the Dirichlet data V_D of the potential $V_D \in H^{1/2}(\partial\Omega_D) \cap L^\infty(\Gamma)$ holds, and for the Dirichlet data of the charge carriers $n_D, p_D \in H^{1/2}(\partial\Omega_D)$ holds.

(iii) The doping concentration C_{dop} as well as the Dirichlet data $n_D(x)$ and $p_D(x)$ for the charge carriers are bounded above and below.

(iv) For the interface conditions, $\alpha \in H^{1/2}(\Gamma) \cap L^\infty(\Gamma)$ and $\beta \in L^\infty(\Gamma)$ hold.

Using these assumptions and similar assumptions as for the local uniqueness, we can state the result of the parallel algorithm that is given in detail in Section 3.3.

Theorem 3.2.2 (FETI algorithm for the drift-diffusion-Poisson system with discontinuities).

Under Assumptions 3.2.1 and Assumptions 2.5.1, the system (3.6–3.7) has a unique solution around thermal equilibrium and can be solved by the one-level FETI algorithm defined in Section 3.3.3 with a preconditioned conjugate gradient method.

Remark 3.2.3. *Using a preconditioner M , a projection P , and the product F of the connectivity matrices with the block-diagonal Schur complement matrix, all as defined in Section 3.3, the condition number of a one-level FETI method usually satisfies*

$$\kappa(PM^{-1}P^T F) \leq C(1 + \log(H/h))^2, \quad (3.8)$$

where h is the maximum size of the finite elements, H is the maximum size of the subdomains, and C is a constant independent of h and H . A proof of the condition-number estimate can be found in (Klawonn and Widlund, 2001; Toselli and Widlund, 2005). Since the jump conditions are inherently included in the FETI algorithm this estimate holds true which is shown for an example in Section 3.4.2.3.

3.3 The Algorithm

To show how the interface conditions are included in the FETI method, we discuss the simpler case of only two subdomains first (see Fig. 1.4). After a brief synopsis of the Schur complement for our purposes, the algorithm for an arbitrary number of domains will be derived in this section.

3.3.1 The Case of Two Subdomains

We start with the variational form of the system (3.6–3.7). Using the definition

$$u \in H_{\Gamma}^1(\Omega) := \{v \in H^1(\Omega) : v(0+, y, z) - v(0-, y, z) = \alpha(y, z) \text{ on } \Gamma\}, \quad (3.9)$$

the variational form of (3.6–3.7) is

$$a(u, v) = f(v) \quad \forall v \in H_{\Gamma}^1(\Omega), \quad (3.10)$$

where

$$a(u, v) := \int_{\Omega} \varepsilon(x) \nabla u \cdot \nabla v dx - \int_{\Gamma} \beta v dy, \quad (3.11a)$$

$$f(v) := \int_{\Omega} f v dx. \quad (3.11b)$$

The energy functionals of the variational problem then are

$$J_1(v_1) = \frac{1}{2} a(v_1, v_1)_{\Omega_1} - f(v_1)_{\Omega_1}, \quad (3.12a)$$

$$J_2(v_2) = \frac{1}{2} a(v_2, v_2)_{\Omega_2} - f(v_2)_{\Omega_2} - \beta(v_2)_{\Gamma} \quad (3.12b)$$

for $v_1, v_2 \in H_\Gamma^1$ where

$$a(u, v)_{\Omega_i} := \int_{\Omega_i} \varepsilon(x) \nabla u \cdot \nabla v dx, \quad (3.13a)$$

$$f(v)_{\Omega_i} := \int_{\Omega_i} f v dx, \quad (3.13b)$$

$$\beta(v)_\Gamma := \int_\Gamma \beta v dy. \quad (3.13c)$$

The additional term (v_2, β) arises from the interface condition (1.2c) for the electric displacement which is due to the extra term in the bilinear form a in (3.11a). Hence the interface condition (1.2c) for the electric displacement is already incorporated, while the condition (1.2b) for the electric potential arises only in H_Γ^1 . To respect the interface condition (1.2b) for the electric potential, we obtain the saddle point of the Lagrangian

$$J^*(v_1, v_2, \mu) = J_1(v_1) + J_2(v_2) + \int_\Gamma \mu(v_1 - v_2 - \alpha) dy. \quad (3.14)$$

We now turn to a finite-element discretization of the problem (3.12), following (Farhat and Roux, 1991). Therefore we define A_1 and A_2 as the stiffness matrices of a_{Ω_1} and a_{Ω_2} , respectively. Furthermore we define f_1 and f_2 as the discretized right-hand sides of the Poisson equation and B_1 and B_2 as the connectivity matrices at the interface Γ with entries in $\{0, 1, -1\}$. Then the problem (3.12) with the interface condition (1.2b) for the electric potential becomes

$$A_1 u_1 = f_1 + B_1^T \lambda, \quad (3.15a)$$

$$A_2 u_2 = f_2 - B_2^T \lambda - B_2^T \beta, \quad (3.15b)$$

$$B_1 u_1 = B_2(u_2 + \alpha), \quad (3.15c)$$

where λ are the Lagrange multipliers. For non-singular A_i , $i \in \{1, 2\}$, this system can be solved according to the original FETI method

$$(B_1 A_1^{-1} B_1^T + B_2 A_2^{-1} B_2^T) \lambda = B_2 A_2^{-1} f_2 - B_1 A_1^{-1} f_1 - B_2 A_2^{-1} B_2^T \beta + B_2 \alpha, \quad (3.16a)$$

$$u_1 = A_1^{-1} (f_1 + B_1^T \lambda), \quad (3.16b)$$

$$u_2 = A_2^{-1} (f_2 - B_2^T \lambda - B_2^T \beta) \quad (3.16c)$$

by first solving equation (3.16a) for the Lagrange multipliers and then substituting into equations (3.16b) and (3.16c).

3.3.2 Schur Complement

For the algorithm in Section 3.3.3 below, it is convenient to use the Schur complement. Consequently we give a brief synopsis for our purposes.

The structure of the stiffness matrices makes it possible to separate the entries for the inner points of the domain and the points at the interface Γ . Hence the stiffness matrices A_i , $i \in \{1, 2\}$, of

the linear systems $A_i u_i = f_i$, $i \in \{1, 2\}$, can be written as

$$A_i = \begin{pmatrix} A_{II}^i & A_{I\Gamma}^i \\ A_{\Gamma I}^i & A_{\Gamma\Gamma}^i \end{pmatrix}. \quad (3.17)$$

These matrices are obtained by splitting the stiffness matrix A of the linear system on the whole domain Ω , where the variables are ordered as $(\Omega_1, \Omega_2, \Gamma)$, i.e.,

$$A = \begin{pmatrix} A_{II}^1 & 0 & A_{I\Gamma}^1 \\ 0 & A_{II}^2 & A_{I\Gamma}^2 \\ A_{\Gamma I}^1 & A_{\Gamma I}^2 & A_{\Gamma\Gamma} \end{pmatrix}, \quad (3.18)$$

where $A_{\Gamma\Gamma} = A_{\Gamma\Gamma}^1 + A_{\Gamma\Gamma}^2$. Similarly, the components of u and f of the whole system can be arranged as

$$u = \begin{pmatrix} u_I^1 \\ u_I^2 \\ u_\Gamma \end{pmatrix} \quad \text{and} \quad f = \begin{pmatrix} f_I^1 \\ f_I^2 \\ f_\Gamma + \beta \end{pmatrix}, \quad (3.19)$$

where $u_\Gamma = u_\Gamma^1 + u_\Gamma^2$ and $f_\Gamma = f_\Gamma^1 + f_\Gamma^2$. To obtain the Schur matrix S of the linear system $Au = f$, we make use of the LU -decomposition of A , i.e.,

$$A = LU = \begin{pmatrix} I & 0 & 0 \\ 0 & I & 0 \\ A_{\Gamma I}^1 A_{II}^1{}^{-1} & A_{\Gamma I}^2 A_{II}^2{}^{-1} & I \end{pmatrix} \begin{pmatrix} A_{II}^1 & 0 & A_{I\Gamma}^1 \\ 0 & A_{II}^2 & A_{I\Gamma}^2 \\ 0 & 0 & S \end{pmatrix}, \quad (3.20)$$

where

$$S = A_{\Gamma\Gamma} - A_{\Gamma I}^1 A_{II}^1{}^{-1} A_{I\Gamma}^1 - A_{\Gamma I}^2 A_{II}^2{}^{-1} A_{I\Gamma}^2. \quad (3.21)$$

By multiplication with L^{-1} , we then obtain the linear system

$$\begin{pmatrix} A_{II}^1 & 0 & A_{I\Gamma}^1 \\ 0 & A_{II}^2 & A_{I\Gamma}^2 \\ 0 & 0 & S \end{pmatrix} u = \begin{pmatrix} f_I^1 \\ f_I^2 \\ g_\Gamma \end{pmatrix}, \quad (3.22)$$

where

$$g_\Gamma = f_\Gamma + \beta - A_{\Gamma I}^1 A_{II}^1{}^{-1} f_I^1 - A_{\Gamma I}^2 A_{II}^2{}^{-1} f_I^2. \quad (3.23)$$

Hence the linear system $Au = f$ can be solved by block Gaussian elimination, solving first

$$S u_\Gamma = g_\Gamma \quad (3.24)$$

and then substituting u_Γ in

$$u_I^i = (A_{II}^i)^{-1} (f_I^i - A_{I\Gamma}^i u_\Gamma). \quad (3.25)$$

In summary, solving the equations (3.16) can be reduced from a linear system involving all discretization points in Ω to a linear system on Γ . Now we are able to prove Theorem 3.2.2 for any number of subdomains.

3.3.3 A One-Level FETI Algorithm for the Drift-Diffusion-Poisson System with Discontinuities

For an arbitrary number N of subdomains, we consider the minimization problem for equation (3.6a) with the discontinuities (3.7). The minimization problem in Schur complement form (Klawonn and Widlund, 2001; Toselli and Widlund, 2005) then reads

$$J(u) := \frac{1}{2} \langle Su, u \rangle - \langle g, u \rangle = \min!, \quad (3.26a)$$

$$Bu = \alpha, \quad (3.26b)$$

where

$$u = \begin{pmatrix} u_1 \\ u_2 \\ \vdots \\ u_N \end{pmatrix}, \quad g = \begin{pmatrix} g_1 \\ g_2 \\ \vdots \\ g_N \end{pmatrix}, \quad S = \begin{pmatrix} S_1 & 0 & \cdots & 0 \\ 0 & S_2 & \ddots & \vdots \\ \vdots & \ddots & \ddots & 0 \\ 0 & \cdots & 0 & S_N \end{pmatrix}, \quad (3.27)$$

where the

$$S_i := A_{\Gamma\Gamma}^i - A_{\Gamma I}^i (A_{II}^i)^{-1} A_{I\Gamma}^i \quad (3.28)$$

are the local Schur complement matrices for $i \in \{1, \dots, N\}$, and B is the connectivity matrix analogous to the connectivity matrices in (3.15). The interface condition for the normal derivative is already incorporated in the vector g as in the last section. Note that the interface condition α is in general not defined at all interfaces with variable u_i , $i \in \{1, \dots, n\}$, i.e., we would usually define

$$\alpha^*(x) := \begin{cases} \alpha(x) & \text{for } x \in \Gamma, \\ 0 & \text{elsewhere.} \end{cases} \quad (3.29)$$

For the sake of simplicity, however, we call this variable again α .

The saddle-point formulation of (3.26) is to find (u, λ) such that

$$Su + B^T \lambda = g, \quad (3.30a)$$

$$Bu = \alpha. \quad (3.30b)$$

In the case of insufficient boundary conditions or floating subdomains, we must also consider matrices R_i , $i \in \{1, \dots, N\}$, of the null-space elements of S with

$$R := \begin{pmatrix} R_1 & 0 & \cdots & 0 \\ 0 & R_2 & \ddots & \vdots \\ \vdots & \ddots & \ddots & 0 \\ 0 & \cdots & 0 & R_N \end{pmatrix} \quad (3.31)$$

and $\text{range}(R) = \ker(S)$. Hence equation (3.30a) becomes

$$u = S^\dagger(g - B^T \lambda) - R\gamma, \quad \text{if } g - B^T \lambda \perp \ker(S), \quad (3.32)$$

where S^\dagger is the pseudoinverse of S . To solve this equation, λ has to be computed first and then γ . If we now substitute this equation into (3.30b), we obtain

$$BS^\dagger B^T \lambda = BS^\dagger g - BR\gamma - \alpha \quad (3.33)$$

and hence (Toselli and Widlund, 2005, p. 146 ff.) we can rewrite the system (3.30) as

$$F\lambda + G\gamma = d, \quad (3.34a)$$

$$G^T \lambda = e, \quad (3.34b)$$

where $F := BS^\dagger B^T$, $G := BR$, $d := BS^\dagger g - \alpha$, and $e := R^T g$. Here the second equation arises from the condition $g - B^T \lambda \perp \ker(S)$. This system can be solved by using a projection

$$P^T := I - G(G^T QG)^{-1} G^T Q \quad (3.35)$$

from $\text{range}(B)$ onto the subspace of Lagrange multipliers which are orthogonal to $\text{range}(G)$ using a scaling matrix Q . The matrix Q can be chosen, e.g., as the Dirichlet preconditioner defined in Klawonn and Rheinbach (2010). This turns (3.34) into the system

$$P^T F \lambda = P^T d, \quad (3.36)$$

$$G^T \lambda = e, \quad (3.37)$$

which can be solved by the following standard preconditioned conjugate-gradient method

Initialize the first Lagrange multiplier and the first residuum	
$\lambda_0 =$	$QG(G^T QG)^{-1}e + \mu, \quad \mu \in \text{range}(P)$
$r_0 =$	$d - F\lambda_0$
For $k = 1, 2, \dots$ until convergence	
Project :	$q_{k-1} = P^T r_{k-1}$
Precondition :	$z_{k-1} = M^{-1} q_{k-1}$
Project :	$y_{k-1} = P z_{k-1}$
$\beta_1 = 0$ and	$\beta_k = \langle y_{k-1}, q_{k-1} \rangle / \langle y_{k-2}, q_{k-2} \rangle$
$p_1 = y_0$ and	$p_k = y_{k-1} + \beta_k p_{k-1}$
	$\alpha_k = \langle y_{k-1}, q_{k-1} \rangle / \langle p_k, F p_k \rangle$
	$\lambda_k = \lambda_{k-1} + \alpha_k p_k$
	$r_k = r_{k-1} - \alpha_k F p_k$

as also stated in (Toselli and Widlund, 2005, p. 149) and which is used for the simulations in Section 3.4.

In every step of (1)-(3) in the self-consistent loop we have to use the CG method. Hence it is of interest to keep the number of iterations in every CG computation small, which can be improved by using a preconditioner M , i.e., we have to solve the equations

$$PM^{-1}P^T F \lambda = PM^{-1}P^T d, \quad (3.38a)$$

$$G^T \lambda = e. \quad (3.38b)$$

For heterogeneous systems it is recommended to use the Dirichlet preconditioner

$$M^{-1} = B_D S B_D^T \quad (3.39)$$

or the lumped preconditioner

$$M^{-1} = B_D A_{\Gamma\Gamma} B_D^T \quad (3.40)$$

where B_D is the connectivity matrix B multiplied with a scaling matrix D including the permittivity ε or the multiplicity of the boxes involved in the degrees of freedom at the interface for redundant Lagrange multipliers and the Dirichlet preconditioner

$$M^{-1} = (B D^{-1} B^T)^{-1} B D^{-1} S D^{-1} B^T (B D^{-1} B^T)^{-1} \quad (3.41)$$

for non-redundant Lagrange multipliers as defined in (Klawonn and Rheinbach, 2010). The iteration count of the Dirichlet preconditioner for non-redundant Lagrange multipliers is given in Section 3.4.2.2 and a comparison of these preconditioners can be found in (Rixen and Farhat, 1999).

Since the jumps in the potential and in the electrical displacement are inherently incorporated in this one-level FETI method, i.e., they arise as additional terms on the right-hand sides, the standard condition number estimate

$$\kappa(P M^{-1} P^T F) \leq C(1 + \log(H/h))^2 \quad (3.42)$$

for one-level FETI methods with Dirichlet preconditioner M holds (Klawonn and Rheinbach, 2010; Klawonn and Widlund, 2001), which concludes the proof of Theorem 3.2.2.

3.4 Numerical Results

In this section, three numerical examples for the FETI method developed in the previous section are given. The first example is two dimensional and the domain consists of 8 subdomains arranged in a 2 times 4 grid, where constant interface conditions separate the four subdomains on each side of the interface. On one side, the drift-diffusion-Poisson system is solved on the four subdomains and on the other side, the Poisson equation with a vanishing right-hand side is solved.

The second and third example are realistic examples and show how this method is used for the simulation of a nanowire transistor or nanowire sensor. The simulation domain is three dimensional and the subdomains are arranged according to the geometry of three different materials arising in real-world devices where the second example only simulates a half device and the third example the whole device.

3.4.1 A Two-Dimensional Example

We consider a two-dimensional domain consisting of 8 subdomains as the first example. As depicted in Fig. 3.1, the simulation domain consists of two parts divided by the interface.

Each part is again divided in 4 subdomains. In the green domains, the drift-diffusion-Poisson system is solved and the blue domains are homogenized, i.e., the Poisson equation holds there.

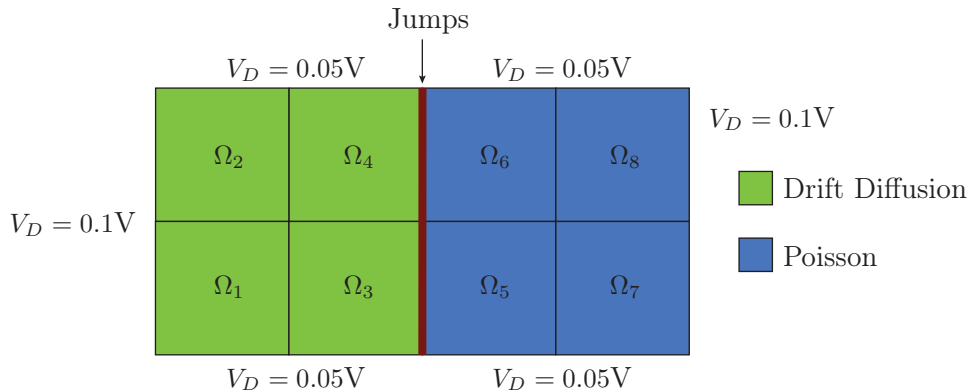


Figure 3.1: 2d simulation domain divided into 8 subdomains. In $\Omega_1, \Omega_2, \Omega_3,$ and Ω_4 , the drift-diffusion-Poisson system holds and in $\Omega_5, \Omega_6, \Omega_7,$ and Ω_8 , the Poisson equation holds. The interface is situated between the subdomains Ω_3 and Ω_4 on the one side and Ω_5 and Ω_6 on the other side. At the interface, jumps in the electric potential and the electric displacement occur. The boundary conditions are Dirichlet conditions.

The interface between the green and the blue domains comprises the homogenized boundary layer, and the interface conditions are given by

$$V(0+, y) - V(0-, y) = 0.01 \quad \text{on } \Gamma, \quad (3.43a)$$

$$\varepsilon_+ \partial_x V(0+, y) - \varepsilon_- \partial_x V(0-, y) = -0.001 \quad \text{on } \Gamma, \quad (3.43b)$$

where the relative permittivities $\varepsilon_+ = 11.9$ and $\varepsilon_- = 80$ multiplied by the vacuum permittivity are chosen as the permittivities of silicon and water, respectively. Furthermore Dirichlet boundary conditions hold as shown in Fig. 3.1.

To verify the correctness of the implementation of the interface conditions, the electric potential at the interface is considered. The jump in the electric potential is shown in Fig. 3.2 and its value is exactly 0.01 as stated in Table 3.1. Furthermore, the 8 subdomains, which are glued together, in every step, by the Lagrange multipliers, are indicated in Fig. 3.2 as well.

V	$V_{10,1}, V_{10,9}$	$V_{10,2}, V_{10,8}$	$V_{10,3}, V_{10,7}$	$V_{10,4}, V_{10,6}$	$V_{10,5}$
In $\Omega_3 \cup \Omega_4$	0.05735	0.05643	0.05513	0.05423	0.05392
In $\Omega_5 \cup \Omega_6$	0.04735	0.04643	0.04513	0.04423	0.04392

Table 3.1: Values of the solution at points on both sides of the interface ($\Omega_3 \cup \Omega_4$ and $\Omega_5 \cup \Omega_6$). The indices denote the x - and y -coordinates of the potential in the discretization grid, i.e., the interface is situated at $x = 10$ and $y \in (1, 9)$. Due to symmetric boundary conditions, the solution is also symmetric with symmetry axis at $y = 5$. The difference is always 0.01 and hence the jump in the potential given by (3.43a) is verified.

In order to verify the jump in the electric displacement as well, we consider the discrete formu-

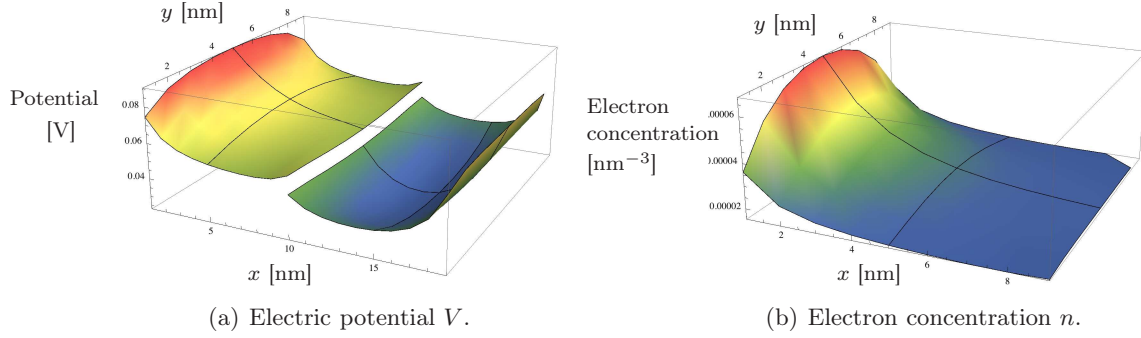


Figure 3.2: (a) Electric potential in all 8 subdomains. (b) Electron density in the 4 subdomains where the drift-diffusion-Poisson system holds.

lation of the normal derivative (Toselli and Widlund, 2005)

$$\lambda^i = A_{\Gamma\Gamma}^i u_{\Gamma}^i + A_{\Gamma\Gamma}^i u_{\Gamma}^i - f_{\Gamma}^i, \quad (3.44)$$

where $A_{\Gamma\Gamma}^i$ and $A_{\Gamma\Gamma}^i$ are the submatrices in the stiffness matrices A_i corresponding to the interface Γ . Similarly, u_{Γ}^i are the discrete solution inside the domains and u_{Γ}^i are the solution on the interface, i.e.,

$$A_i = \begin{pmatrix} A_{II}^i & A_{I\Gamma}^i \\ A_{\Gamma I}^i & A_{\Gamma\Gamma}^i \end{pmatrix}, \quad u_i = \begin{pmatrix} u_I^i \\ u_{\Gamma}^i \end{pmatrix}, \quad (3.45)$$

when the linear system of the finite-element discretization is of the form $A_i u_i = f_i$.

The values of the discrete normal derivatives on the interface computed by (3.44) are shown in Table 3.2.

λ	$\lambda_{10,1}, \lambda_{10,9}$	$\lambda_{10,2}, \lambda_{10,8}$	$\lambda_{10,3}, \lambda_{10,7}$	$\lambda_{10,4}, \lambda_{10,6}$	$\lambda_{10,5}$
In $\Omega_3 \cup \Omega_4$	0.001539	0.001321	0.001262	0.001231	0.001221
In $\Omega_5 \cup \Omega_6$	0.000539	0.000321	0.000262	0.000231	0.000221

Table 3.2: Values of the normal derivative of the solution on both sides of the interface Γ . The indices denote the x - and y -coordinates of the potential in the discretization grid. Due to symmetric boundary conditions, the normal derivative is also symmetric with symmetry axis at $y = 5$. The difference between the normal derivatives satisfies exactly the interface condition for the electric displacement given by (3.43b).

Due to the symmetric boundary conditions and geometry, the values with the same distance from $V_{10,5}$ coincide. The difference between the normal derivatives on both sides is exactly the interface condition $\beta = -0.001$ in (3.43b).

3.4.2 Two 3D Examples

Two examples are chosen to show the implementation of the interface conditions in the calculations of the different materials. Since the interface conditions come from the boundary-layer model they can be assumed to be constant on each grid point on the interface.

The first example describes a half of an NWFET device where we show the jumps at the interface, the correct implementation at the corners of the interface, the jumps in the electrical potential at different cross sections, and the ideal speed-up of this FETI technique.

The second example describes the real geometry, although we use a smaller geometry to keep the explanations simple. Here we show again the jumps in the electrical potential at different cross sections and a comparison of different preconditioners.

Both examples are in 3d and use the Dirichlet and Neumann conditions proposed in Fig. 1.7.

3.4.2.1 A 3D Example – One Half of a Symmetric Device

We are now going to simulate nanowire field-effect sensors. These sensors consist of three materials as shown schematically (not to scale) in Fig. 3.3.

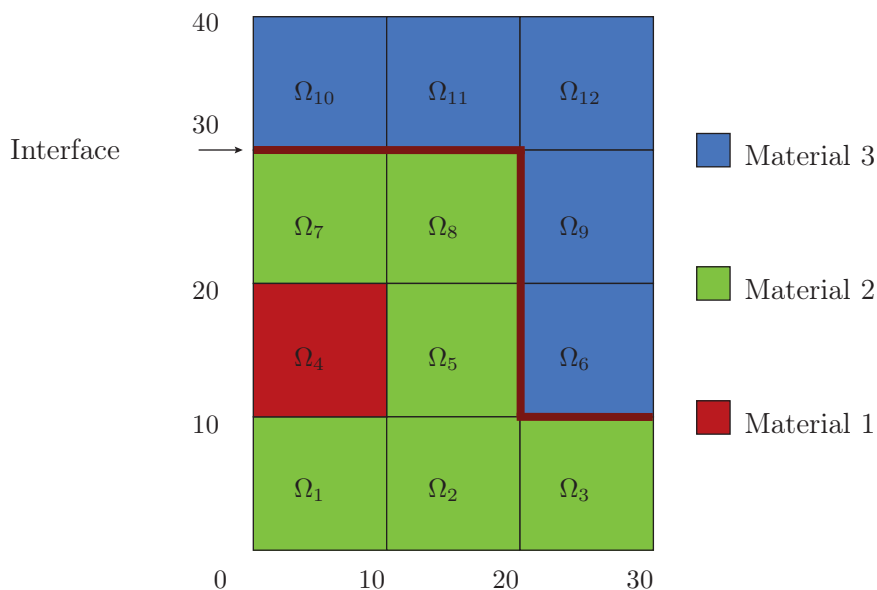


Figure 3.3: A cross section of the simulation domain with the 12 blocks of the FETI algorithm in the x - and y -directions. The interface is indicated as well.

Using the present FETI method together with models for the surface charge concentrations, it is now possible to perform realistic simulations of nanowire bio- and gas sensors such as DNA sensors, cancer-marker sensors, and metal-oxide gas sensors. Here results for a 3d simulation domain with a width of 30, a height of 40, and a length of 20 are shown. The decomposition of the domain in the x - and y -directions is depicted in Fig. 3.3, and in the z -direction the domain is sliced once. Due to the chosen grid spacing of length 1 every block is of size $11 \times 11 \times 11$.

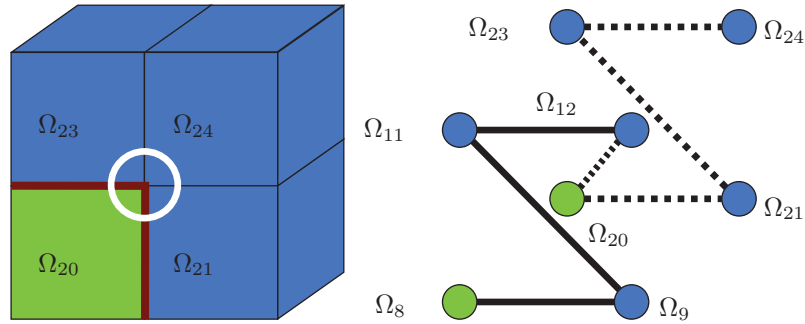


Figure 3.4: Non-redundant connection of 8 blocks at the vertex $(20, 30, 10)$.

Furthermore, different boundary conditions are incorporated: at the top and bottom of the simulation domain and also at the beginning and at the end (in z -direction) of material 1 (the red region) in Fig. 3.3, Dirichlet conditions for ohmic contacts hold, while everywhere else Neumann conditions hold. These boundary conditions correspond to the real-world situation. The points where more than two blocks contribute are glued non-redundantly, e.g., at $(20, 30, 10)$ the connection between the points is as shown in Fig. 3.4.

As in the first example, we verify the correctness of the interface conditions. Therefore the potential V and its normal derivatives were computed at the points $(20, i, 10)$, $i \in [20, 30]$, and are shown in Table 3.3 and Table 3.4. These data verify that the jump conditions

$$V(0+, y, z) - V(0-, y, z) = -0.01 \quad \text{on } \Gamma, \quad (3.46a)$$

$$\varepsilon_+ \partial_x V(0+, y, z) - \varepsilon_- \partial_x V(0-, y, z) = 0.0001 \quad \text{on } \Gamma, \quad (3.46b)$$

hold at each point.

V	$V_{20,20,10}$	$V_{20,21,10}$	$V_{20,22,10}$	$V_{20,23,10}$	$V_{20,24,10}$	$V_{20,25,10}$
$\Omega_8 \cup \Omega_{20}$	0.00223	0.00224	0.00225	0.00228	0.00234	0.00247
$\Omega_9 \cup \Omega_{21}$	-0.00777	-0.00776	-0.00775	-0.00772	-0.00766	-0.00752
	$V_{20,26,10}$	$V_{20,27,10}$	$V_{20,28,10}$	$V_{20,29,10}$	$V_{20,30,10}$	
$\Omega_8 \cup \Omega_{20}$	0.00272	0.00313	0.00380	0.00499	0.00846	
$\Omega_9 \cup \Omega_{21}$	-0.00728	-0.00687	-0.00620	-0.00501	-0.00154	

Table 3.3: Numerical values for the potential V at the surface points $(20, i, 10)$, $i \in (20, 30)$. A jump of the potential of -0.01 is observed for all the points as expected.

The jumps can also be seen in cross sections of the electric potential V . The cross section at $z = 10$ is shown in Fig. 3.5 and the jump in the potential can be clearly seen. The different materials are in the same color as in Fig. 3.3, where the red region corresponds to silicon, the green region corresponds to silicon dioxide, and the blue region corresponds to the aqueous solution or air.

$\lambda [10^{-6}]$	$\lambda_{20,20,10}$	$\lambda [10^{-6}]$			$\lambda_{20,30,10}$
$\Omega_5 \cup \Omega_8 \cup \Omega_{17} \cup \Omega_{20}$	-27.091	$\Omega_8 \cup \Omega_{20}$			-189.4
$\Omega_6 \cup \Omega_9 \cup \Omega_{18} \cup \Omega_{21}$	72.909	$\Omega_9 \cup \Omega_{11} \cup \Omega_{12} \cup \Omega_{21} \cup \Omega_{23} \cup \Omega_{24}$			-89.4
$\lambda [10^{-6}]$	$\lambda_{20,21,10}$	$\lambda_{20,22,10}$	$\lambda_{20,23,10}$	$\lambda_{20,24,10}$	$\lambda_{20,25,10}$
$\Omega_8 \cup \Omega_{20}$	-28.8631	-30.7564	-33.1229	-36.4034	-41.1923
$\Omega_9 \cup \Omega_{21}$	71.1368	69.2436	66.8771	63.5967	58.8077
$\lambda [10^{-6}]$	$\lambda_{20,26,10}$	$\lambda_{20,27,10}$	$\lambda_{20,28,10}$	$\lambda_{20,29,10}$	
$\Omega_8 \cup \Omega_{20}$	-48.3434	-59.1586	-75.7685	-101.9625	
$\Omega_9 \cup \Omega_{21}$	51.6566	40.8414	24.2315	-1.9625	

Table 3.4: Numerical values for the normal derivatives λ of the potential V at the surface points $(20, i, 10)$, $i \in (20, 30)$. A jump of the derivative of 0.0001 V has been obtained for all the points. The magnitude of the derivatives are of 10^{-6} .

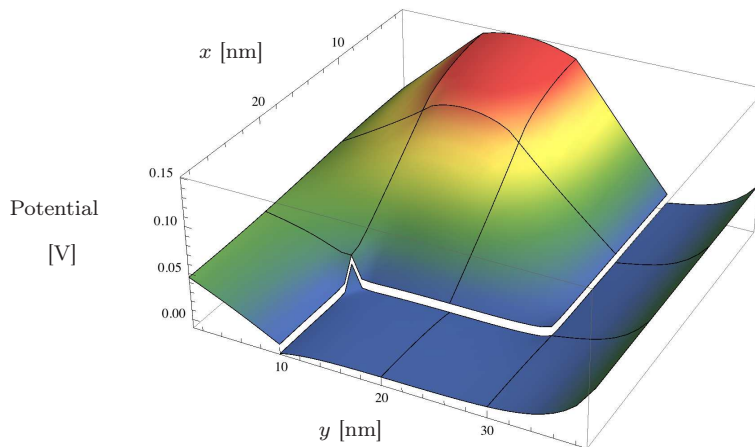


Figure 3.5: Electric potential V in the cross section $z = 10$ nm.

The potential in the silicon region is larger due to the Dirichlet conditions at the beginning and at the end of the nanowire, i.e., at $z = 0$ and $z = 20$, which can also be seen in Fig. 3.6, where a cross section of the simulation domain at $x = 5$ is shown. On the left-hand side of Fig. 3.6, the electric potential is depicted, while the right-hand side shows the corresponding electron density. The electron density, the electric potential, and the interface conditions are calculated self-consistently in an enhanced Scharfetter-Gummel iteration scheme.

The speedup of such 3d simulations with 45 blocks and 720 000 d.o.f. shows an almost ideal behavior as illustrated in Fig. 3.7. The speedup is significant even for 64 processors, although we are simulating on only 45 blocks.

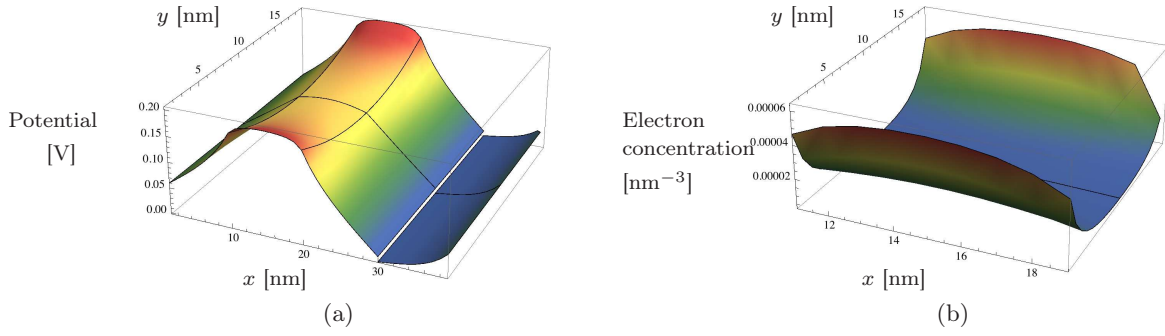


Figure 3.6: (a) Electric potential V in the cross section at $x = 5$. (b) Corresponding electron concentration n in the same cross section.

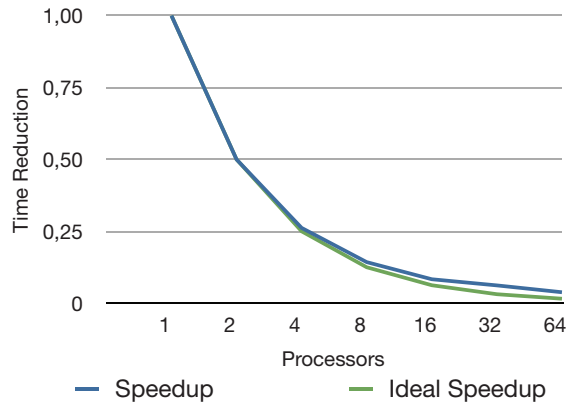


Figure 3.7: Actual speedup vs. ideal speedup of a 3d simulation.

3.4.2.2 A 3D Example – Whole Device

For the following example, with a cross section as shown in Fig. 3.8, we keep the dimensions small and take boxes with the size $10 \times 10 \times 10$ and a total length, in z -direction, of 20. Hence the whole simulation domain consists of 18 blocks. Furthermore we apply 0.01 V backgate voltage, i.e., at $y = 0$, and 0.05 V at the source, i.e., in Ω_{S_i} at $z = 0$. All other constants in the drift-diffusion equations are chosen as in Markowich et al. (1990) where room temperature is assumed.

As aforementioned the jump conditions are defined by the boundary layer model. For the sake of simplicity we neglect this part and take the following constant jump conditions:

$$V(0+, \mathbf{y}) - V(0-, \mathbf{y}) = -0.003, \quad (3.47a)$$

$$\varepsilon_{\text{liq}} \partial_{x_1} V(0+, \mathbf{y}) - \varepsilon_{\text{ox}} \partial_{x_1} V(0-, \mathbf{y}) = 0.00001. \quad (3.47b)$$

At the cross section $z = 10$ in Figure 3.9 we can see the backgate condition on the left, the electrostatic potential of the Poisson drift-diffusion system in the middle and the aqueous solution (dark green). The jump conditions are clearly depicted between the oxide and the aqueous solution.

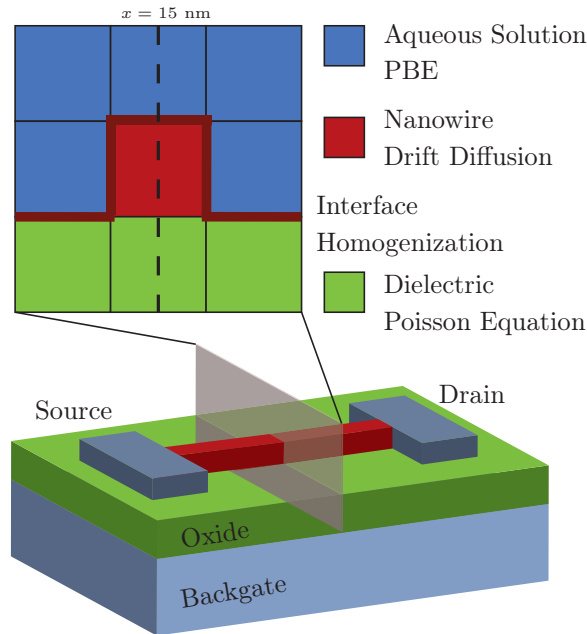


Figure 3.8: Schematic diagram of the NWFET device. The different equations used in the simulations and the cross section $x = 15$ used in the remaining figures are indicated. The blocks for parallelization have a size of $10 \times 10 \times 10 \text{ nm}^3$ (Fig. 2, 3) or $10 \times 10 \times 5 \text{ nm}^3$ (Fig. 4, 5, 6).

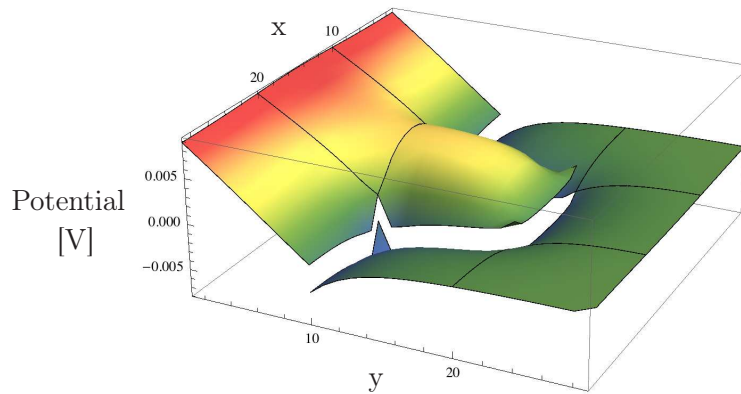


Figure 3.9: Cross section of the electrostatic potential at $z = 10$.

The symmetric structure of the device can be seen at the cross section $y = 15$ in Figure 3.10. Here we have the solution of the Poisson drift-diffusion system and the Poisson equation with vanishing right-hand side in the middle, and the aqueous solution on the left and right of it. Between $12 \leq x \leq 18$ at $z = 0$ the Dirichlet conditions for the source contact hold. Again the jump conditions can be clearly seen.

The same Dirichlet conditions for the source contact are visible at the cross section $x = 15$ in Figure 3.10. Here we have at the left the oxide, in the middle the silicon covered by an oxide layer, and at the right the aqueous solution separated from the oxide by the jump conditions.

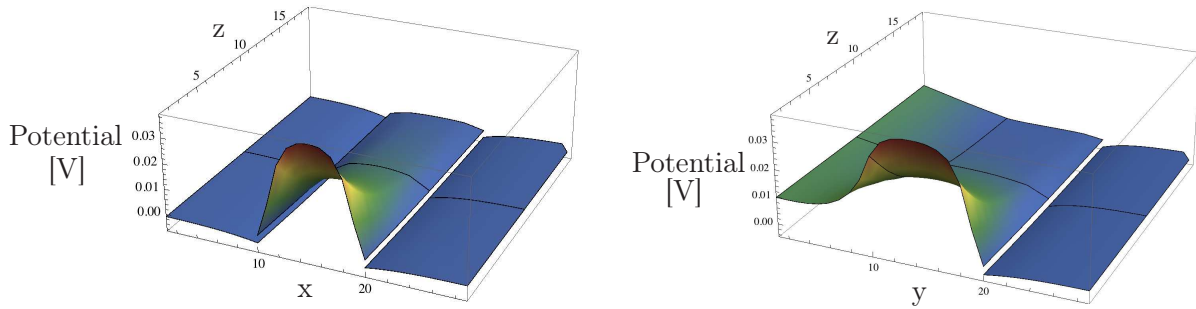


Figure 3.10: Left: Cross section of the electrostatic potential at $y = 15$. Right: Cross section of the electrostatic potential at $x = 15$.

As aforementioned the choice of the preconditioner is important for the reduction of computation time. In our case it is recommended to use the Dirichlet preconditioner. We will show in the following that the condition number estimate is valid for a test problem with jump conditions.

3.4.2.3 Condition Number Estimate

In this subsection we show the iteration number, the smallest, and the largest eigenvalue of a model problem similar to (Toselli and Widlund, 2005, p. 187) with and without jumps. We use the unit cube as domain with $N \times N \times N$ subdomains. The permittivity alternates between 1 and 10^4 and we have homogeneous Dirichlet conditions at the front, left, and bottom side of the cube and homogeneous Neumann conditions everywhere else. On each subdomain we solve the Poisson equation with constant right-hand side and the stopping criterion for the residual is the reduction of the initial residual by 10^{-7} .

Subdomains	Dof/Subdom.	Dof	It.	λ_{\min}	λ_{\max}	It. jumps	$\lambda_{\min}^{\text{jumps}}$	$\lambda_{\max}^{\text{jumps}}$
27	125	2197	9	1	4.16718	14	1	4.61454
125	125	9261	12	1	4.64205	19	1	4.64386
343	125	24389	13	1	4.68298	19	1	4.68597

Table 3.5: Iteration number of the Dirichlet preconditioner for non-redundant Lagrange multipliers with jumps and without jumps.

As seen in Table 3.5 the condition number is nearly constant for fixed H/h and the condition number estimate is valid for this example. Since this example includes all the relevant ingredients for our NWFET simulator the condition estimate holds for our problem.

3.5 Summary

The FETI method of Farhat and Roux has been extended to the nonlinear drift-diffusion-Poisson system including discontinuities, i.e., jumps of the solution and its normal derivative at an

interface. FETI algorithms have been presented for the case of two subdomains and for an arbitrary number of subdomains. In the latter case, the Schur matrix form was presented. A condition-number estimate was given as well.

Three numerical examples have been presented in order to verify the method. Firstly, a 2d problem was presented which verified the correct implementation of the interface conditions numerically. Since the motivation of this work is to use this FETI method for the simulation of nanowire sensors and semiconductor devices in general two 3d examples were given. The subdomains modeled the structure of a real sensor device. The correctness of the 3d algorithm was verified as well.

Since the boundary layer model is chosen, the different physical and geometrical properties of NWFET devices can be tested for their influence on the sensitivity of the sensor. Simulations for two different sensors, a DNA sensor and a PSA sensor, are given in Chapter 4.

Simulation Results

THE SIMULATIONS of two different NWFET sensors, a DNA sensor and a PSA sensor, are presented in the following. In both examples, the simulator is calibrated to real-world measurements of current-voltage characteristics. In the case of the DNA sensor, not all geometric properties are given and hence the geometric properties as well as physical properties are calibrated. In the case of the PSA sensor the geometric properties are given and hence only two physical physical properties of the nanowire, namely the mobility of the charge carriers and the thermal voltage, are adjusted. This is reasonable since the nanowire is not expected to have bulk properties of silicon (see Section 4.2.2). With these adjustments very good agreement is found. The boundary layer models used are the MMC algorithm from Section 1.4.2.1 for the surface charge of DNA and the PROPKA algorithm from Section 1.4.2.3 for the surface charge of PSA. After calibration, we show how sensitivity can be improved by changing different geometric or physical properties of the NWFET sensor.

4.1 DNA Sensor

In this section, we simulate an NWFET-DNA sensor and determine optimal points for sensitivity. To that end, the surface charge density γ and the dipole moment density ζ are computed by Monte-Carlo simulations as described in Section 1.4.2.1 or more detailed in (Bulyha and Heitzinger, 2011). A brief recapitulation of the method in Section 1.4.2.1 is given in Section 4.1.1. The charge concentration, as result from the Monte-Carlo simulations, depends on the surface potential. Hence we use a look-up table with surface charges and dipole moments for different surface potentials. Using the look-up tables, the computation is done self consistently by the loop in Section 4.1.2.

The simulator is calibrated to measured values in Section 4.1.3 and the operating conditions for the optimal sensitivity for different sensor properties are found in Section 4.1.4.

4.1.1 The Boundary Layer Model

The critical issue for the modeling of the sensitivity of NWFET sensors is the screening of the partial charges of the target molecules by the free ions. The biomolecules and their partial charges are fixed at the bottom of the simulation box containing the electrolyte (see Fig. 1.5). In the case of DNA, the strands are modeled as cylinders that exclude free ions and the partial charges of the phosphate groups of the backbone are situated on a helix at the cylinder surface. The biomolecules are arranged in 50 nm high boxes, where the bottom corresponds to the sensor surface. The free ions are Na^+ and Cl^- .

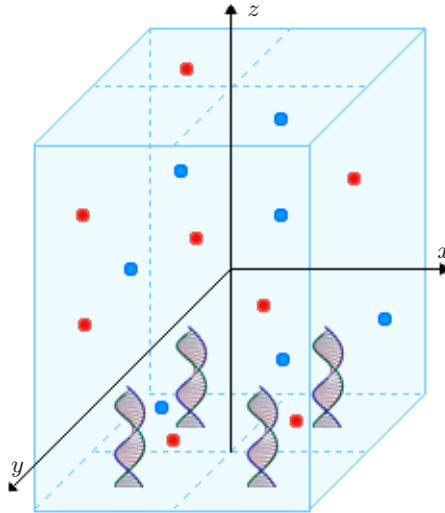


Figure 4.1: The simulation domain of a Monte-Carlo simulation. Here it contains 2×2 biomolecules.

The top and the bottom of the simulation boxes are impenetrable walls with given charge densities, which control the desired electric field determined in the self-consistent loop (see below). Due to the surface charge of silicon oxide in water, the wall at the bottom carries an additional charge density ($-0.2q/\text{nm}^2$ for SiO_2).

The immobilized biomolecules at the bottom wall can be, e.g., PNA (peptide nucleic acid), ssDNA (single-stranded DNA), or dsDNA (double-stranded DNA) oligomers of arbitrary length. If there is a single molecule in the simulation box, it is immobilized at the center of the bottom wall. If the simulation box contains several oligomers, they are arranged in a square grid and each molecule is centered in its grid cell (see Fig. 4.1).

Finally, the surface-charge density γ and the dipole-moment density ζ are calculated from the

integrals

$$\gamma = \int \chi(x, y, z) dx y z, \quad (4.1)$$

$$\zeta = \int x \chi(x, y, z) dx y z, \quad (4.2)$$

where the charge concentration χ is obtained in the MMC simulation.

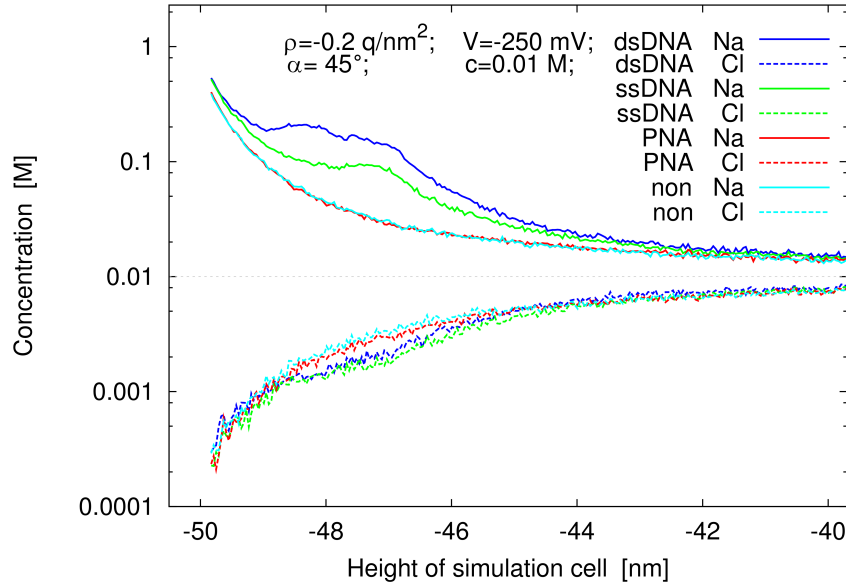


Figure 4.2: Concentration profiles for a 1:1 electrolyte for no molecules, PNA, ssDNA, and dsDNA on a logarithmic scale as a function of distance from the surface (Baumgartner et al., 2011a).

Due to the importance of the biofunctionalized surface layer and the screening by free ions, a numerical example of a MMC simulation is shown here. In this example, nine strands of ssDNA, dsDNA, or PNA are attached to a silicon-oxide surface by 1 nm long linkers at a distance of 8 nm; a non-functionalized surface is simulated as well. The silicon-oxide surface carries a charge density of -0.2 q/nm^2 . The angle of the oligomers with respect to the surface is 45° , the Na^+Cl^- concentration is 0.01 M, the temperature is 300 K, and the applied potential is -250 mV . The resulting concentration profiles are shown in Fig. 4.2.

Based on these concentration profiles, the surface-charge density γ and dipole-moment density ζ are shown in Fig. 4.3 as a function of the applied voltage varying from -250 mV to 250 mV . It is noted that the screening of the surface charge by counter ions is about 50% for a nonfunctionalized surface without an applied voltage, i.e., the oxide charge density $\rho = -0.2 \text{ q/nm}^2$ effectively decreases to $\gamma = -0.1 \text{ q/nm}^2$.

In a working sensor, probe molecules (p) and probe-target complexes (pt) are always present. For example, ssPNA probes can be used to detect ssDNA oligomers, and hence there will be ssPNA probes and ssPNA-ssDNA complexes. Therefore the surface-charge and dipole-moment

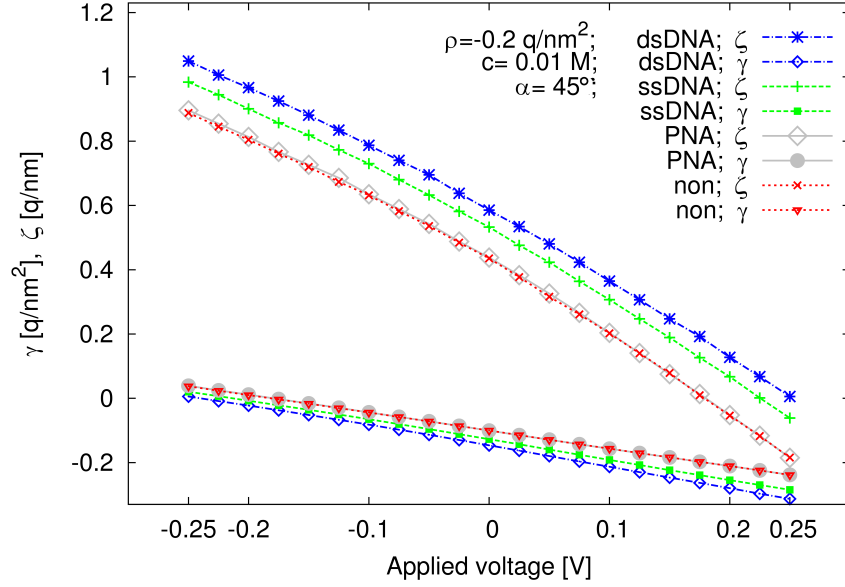


Figure 4.3: Surface-charge density γ and dipole-moment density ζ as a function of applied voltage for no molecules and for 10-mers of PNA, ssDNA, and dsDNA. The angle of the oligomer is $\alpha = 45^\circ$ with respect to the surface, the surface-charge density is $\rho = -0.2 \text{ q/nm}^2$, the ionic bulk concentration is 0.01 M, and the applied potentials varies between -250 mV to 250 mV . The surface-charge and dipole-moment densities are of the same order of magnitude.

densities include in fact two terms, i.e.,

$$\gamma = \kappa\gamma_{pt} + (1 - \kappa)\gamma_p, \quad (4.3)$$

$$\zeta = \kappa\zeta_{pt} + (1 - \kappa)\zeta_p, \quad (4.4)$$

where κ is the binding efficiency. In this thesis, the value $\kappa = 1$ is used corresponding to an optimal binding efficiency. A value of $\kappa \approx 1$ can be obtained experimentally at the probe densities considered here (Peterson et al., 2001).

4.1.2 The Self-Consistent Loop

We are now able to compute the electrostatic potential V and the charge carriers n and p in a self-consistent loop. Initial values n_0 , p_0 , ζ_0 , and γ_0 are chosen and then the following steps in a Scharfetter-Gummel type (Scharfetter and Gummel, 1969) iteration scheme are performed.

1. In iteration $k + 1$, solve the homogenized boundary value problem

$$\begin{aligned}
-\varepsilon_{\text{Si}}\Delta V_{k+1} &= q(C_{\text{dop}} + p_k - n_k) && \text{in } \Omega_{\text{Si}}, \\
-\varepsilon_{\text{ox}}\Delta V_{k+1} &= 0 && \text{in } \Omega_{\text{ox}}, \\
-\varepsilon_{\text{liq}}\Delta V_{k+1} &= 2\eta\xi V_{k+1} && \text{in } \Omega_{\text{liq}}, \\
V_{k+1}(0+) - V_{k+1}(0-) &= \frac{\zeta_k}{\varepsilon(0+)} && \text{on } \Gamma, \\
\varepsilon_{\text{liq}}\nabla V_{k+1}(0+) - \varepsilon_{\text{ox}}\nabla V_{k+1}(0-) &= -\gamma_k && \text{on } \Gamma, \\
V_{k+1} &= V_D && \text{on } \partial\Omega_D, \\
\nabla_\nu V_{k+1} &= 0 && \text{on } \partial\Omega_N
\end{aligned}$$

to obtain the electrostatic potential V_{k+1} .

2. Then solve the boundary-value problem

$$\begin{aligned}
\nabla \cdot (D_n \nabla n_{k+1} - \mu_n n_{k+1} \nabla V_k) &= \frac{n_{k+1} p_k - n_i^2}{\tau_p(n_{k+1} + n_i) + \tau_n(p_k + n_i)} && \text{in } \Omega_{\text{Si}}, \\
n_{k+1} &= n_D && \text{on } \partial\Omega_D, \\
\nabla_\nu n_{k+1} &= 0 && \text{on } \partial\Omega_N
\end{aligned}$$

to obtain the electron concentration n_{k+1} .

3. Then solve the boundary-value problem

$$\begin{aligned}
\nabla \cdot (D_p \nabla p_{k+1} + \mu_p p_{k+1} \nabla V_k) &= \frac{n_{k+1} p_{k+1} - n_i^2}{\tau_p(n_{k+1} + n_i) + \tau_n(p_{k+1} + n_i)} && \text{in } \Omega_{\text{Si}}, \\
p_{k+1} &= p_D && \text{on } \partial\Omega_D, \\
\nabla_\nu p_{k+1} &= 0 && \text{on } \partial\Omega_N
\end{aligned}$$

to obtain the hole concentration p_{k+1} .

4. Get $\zeta_{k+1} = \zeta(V_{k+1})$ and $\gamma_{k+1} = \gamma(V_{k+1})$ from a look-up table computed by the Monte-Carlo simulator.
5. Increase k and go to the first step.

In the fourth step, the surface-charge density and dipole-moment density are computed depending on the electric surface potential. Since the surface charges are small, the fourth step has only a small effect on the number of iterations and hence computation time; good convergence behavior is observed.

Furthermore, solving the boundary-value problems is very fast if the grid points near the interface Γ are numbered suitably (Baumgartner and Heitzinger, 2012a).

4.1.3 Simulator Calibration

Now we are able to compare simulated and measured current-voltage characteristics in order to verify the model. We investigate a 500 nm long n-doped nanowire in the simulation domain shown in Fig. 1.6.

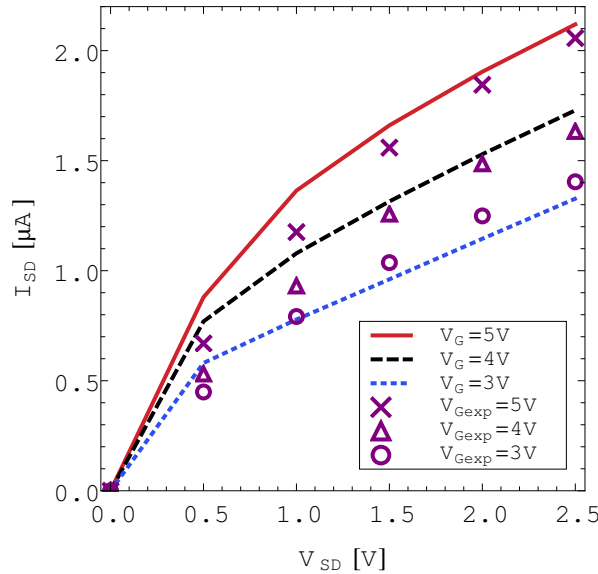


Figure 4.4: Current-voltage characteristics for an n-doped non-functionalized nanowire field-effect biosensor. The solid line corresponds to a back-gate voltage of 5 V, the dashed line to 4 V, and the dotted line to 3 V. The crosses are the corresponding measurements for a back-gate voltage of 5 V, the triangles for 4 V, and the circles for 3 V (Li et al., 2006).

The current-voltage characteristics of this device with a non-functionalized surface is shown in Fig. 4.4 for various back-gate voltages and they are compared with the current-voltage characteristics from experiments (Li et al., 2006). Very good agreement is found although not all geometric parameters are known.

4.1.4 Optimization of Device Parameters

As mentioned above, the Monte-Carlo simulations yield the ionic concentration in the biofunctionalized surface layer. A change from a non-functionalized surface to a surface with DNA strands decreases the current due to the negative partial charges of DNA strands. This is the behavior known from nanowire field-effect transistors (cf. Section 1.2 or (Cui et al., 2001; Patolsky et al., 2007)). The current change in this section is defined as

$$\Delta I_{SD} = \frac{I_n - I_f}{I_f}, \quad (4.5)$$

where I_n and I_f are the currents of the non-functionalized and functionalized device, respectively.

The value of ΔI_{SD} will be used to measure sensitivity in the following. Our aim is to find optimal design parameters by varying device parameters. To that end, the lengths and thicknesses of the nanowire, the gate and source voltages, and the doping concentrations are varied.

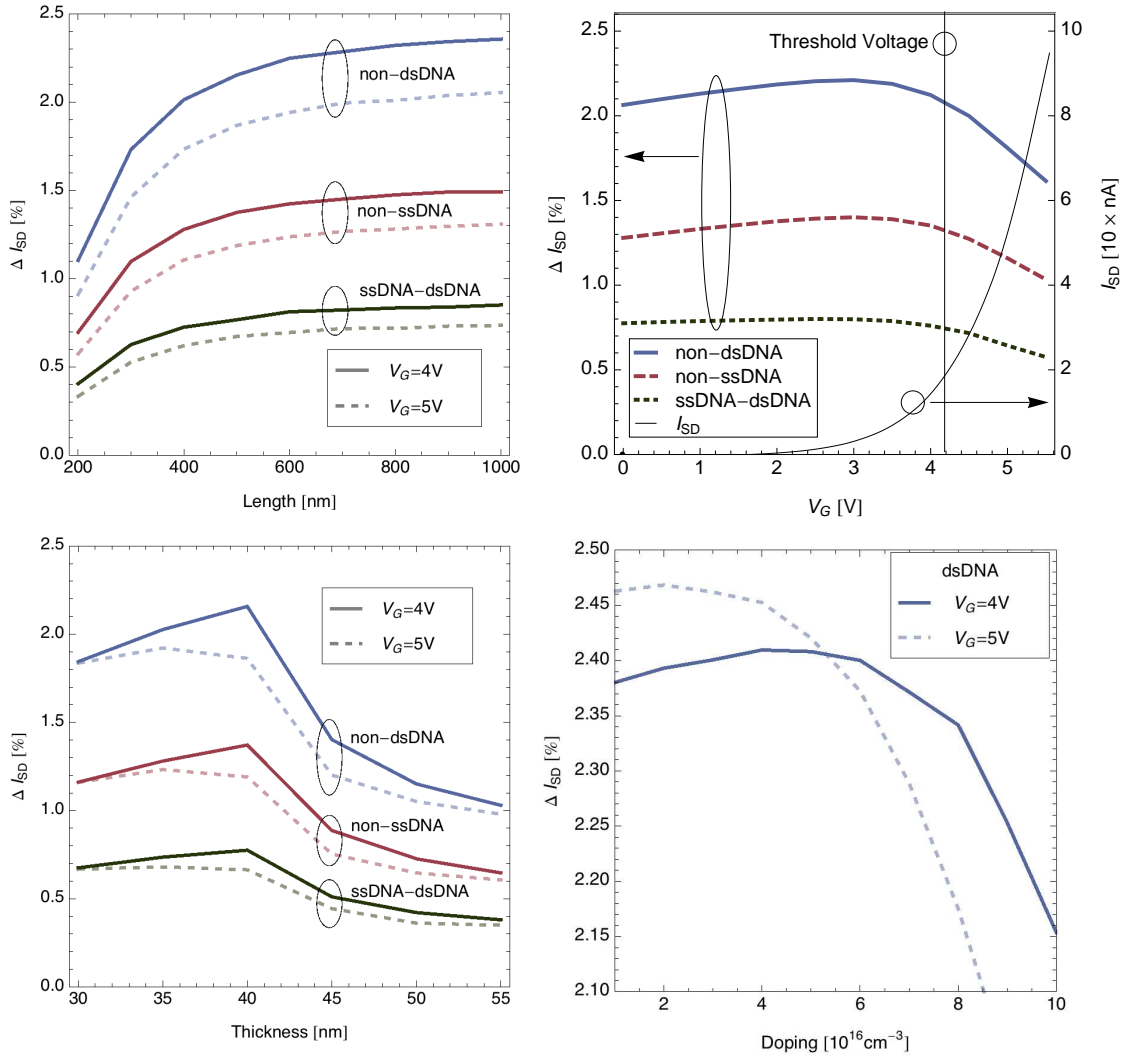


Figure 4.5: Top left: The current change ΔI_{SD} is shown as a function of the length of the nanowire for three situations: the change from non-functionalized to dsDNA (top), the change from non-functionalized to ssDNA (middle), and the change from ssDNA to dsDNA (bottom). The back-gate voltages are 4 V and 5 V and the source/drain voltage is 0.5 V.

Top right: The current change ΔI_{SD} is shown as a function of the gate voltage with the scale on the left-hand side for the same three situations as in Fig. 4.5. The source/drain current I_{SDG} (black, solid line) is shown as a function of the gate voltage as well with the scale on the right-hand side. The threshold voltage is indicated by a vertical black line. The source/drain voltage is 0.1 V.

Bottom left: Current change ΔI_{SD} for gate voltages of 4 V and 5 V for the three situations non-functionalized/dsDNA, non-functionalized/ssDNA, and ssDNA/dsDNA as a function of the nanowire thickness. The source/drain voltage is 0.1 V.

Bottom right: Current change from non-functionalized surface to dsDNA for gate voltages of 4 V and 5 V at a source/drain voltage of 0.5 V as a function of the doping concentration.

Simulations show that increasing the length of the nanowire improves sensitivity due to the reduced influence of the source and drain contacts and the larger influence of the partial charges in the surface layer (see top left of Fig. 4.5). This is comparable to a larger gate structure on top of a FET.

Furthermore it is found that increasing the back-gate voltage results in an increase of sensitivity (see top right of Fig. 4.5). However, when increasing the back-gate voltage above the optimal point, the back-gate voltage dominates the potential (see Fig. 4.6), i.e., the increase of the electric potential is larger away from the functionalized surface and hence the electrons away from the surface are more important than the electrons closer to the surface, which results in a decrease of sensitivity (see top right of Fig. 4.5). Note that in the top right of Fig. 4.5 the source/drain voltage differs from the top left. Below the optimal point, i.e., below a back-gate voltage of 3 V, the sensitivity decays slightly. Additionally, the transfer characteristic shows that the optimal sensitivity is in the sub-threshold regime. Consequently a careful manipulation of the back-gate voltage is recommended.

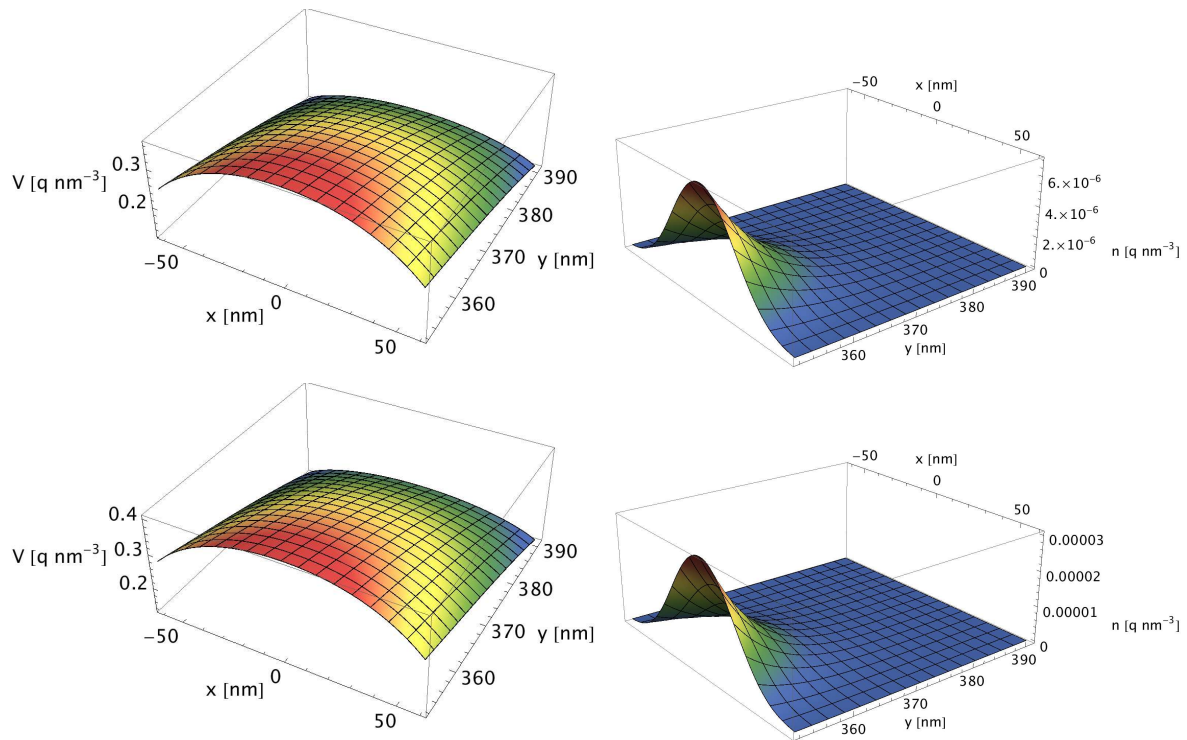


Figure 4.6: Electric potential and electron density in a cross section of the silicon nanowire at $z = 250$ nm. The figures at the top correspond to a back-gate voltage of 4 V and the figures at the bottom correspond to a back-gate voltage of 5 V. The source/drain voltage is 0.1 V.

A similar effect has been found regarding the nanowire thickness. Here an optimal thickness of 40 nm has been obtained and the sensitivity shows a steep decline for thicker semiconductor layers (see bottom left of Fig. 4.5). Again the back-gate voltage plays an important role. The optimal point itself results from the influence of the partial charges of the target molecules which

can control the whole volume of the nanowire at a certain thickness and whose influence decreases when a certain limit is exceeded (cf. (Gao et al., 2010)).

Another parameter affecting the sensitivity is the doping concentration (see bottom right of Fig. 4.5). Here the doping is varied between 10^{16}cm^{-3} and 10^{17}cm^{-3} and the sensitivity ΔI_{SD} shows an arch structure where the optimal point changes with the back-gate voltage. It is noteworthy that the sensitivity remains rather flat below the optimal doping concentration, whereas for doping concentrations above the optimal point a steep decay is observed.

4.2 PSA Sensor

The advantage of the PDE model described in this thesis is that only the boundary layer model needs to be changed when simulating a different sensor. In the case of a PSA sensor we use the very fast PROPKA algorithm explained in Section 1.4.2.3. This simulator is online available and the computation of the charge lasts only seconds. The results of the PROPKA simulator is shown in Section 4.2.1. Here the screening of the PSA charges is not inherently included, as it was for the MMC algorithm. Hence we show a simple screening model which has been already used for the simulation of NWFET devices. Then, after calibration in Section 4.2.2 the sensitivity is tested for different parameters in Section 4.2.2.

4.2.1 Boundary Layer Model

Since the structure of proteins is more difficult to simulate than the structure of DNA, we use a probabilistic method, the PROPKA algorithm explained in Section 1.4.2.3, instead of Monte-Carlo calculations. With this method we can use the structure from PSA from the protein database (see also the left-hand side of Fig. 4.7) to get the protein charge from PROPKA within seconds. The PSA charge obtained by PROPKA is depicted in the right-hand side of Fig. 4.7.

For calibration we compare with measurements at a pH value of 7.4 and hence we obtain a point charge of $-8q$ from the PROPKA simulator. Using a footprint of 10 nm this results in an unscreened surface charge of $-0.8q \cdot \text{nm}^{-2}$.

4.2.1.1 Screening

The liquid surrounding the nanowire is a ionic solution. From ionic solutions it is known that the effective charge of the biomolecules is lowered due to Debye screening (Stern et al., 2007b; Vacic et al., 2011). This screening is exponential, i.e., it follows $\exp(-x/\lambda_D)$ where

$$\lambda_D = \frac{1}{\sqrt{4\pi l_B \sum_i \rho_i z_i^2}}, \quad (4.6)$$

$l_B = 0.7 \text{ nm}$ is the Bjerrum length while ρ_i and z_i are the density and valence of the ion species i .

When we simulate the protein as a point charge, i.e., the charge of the protein is homogeneously

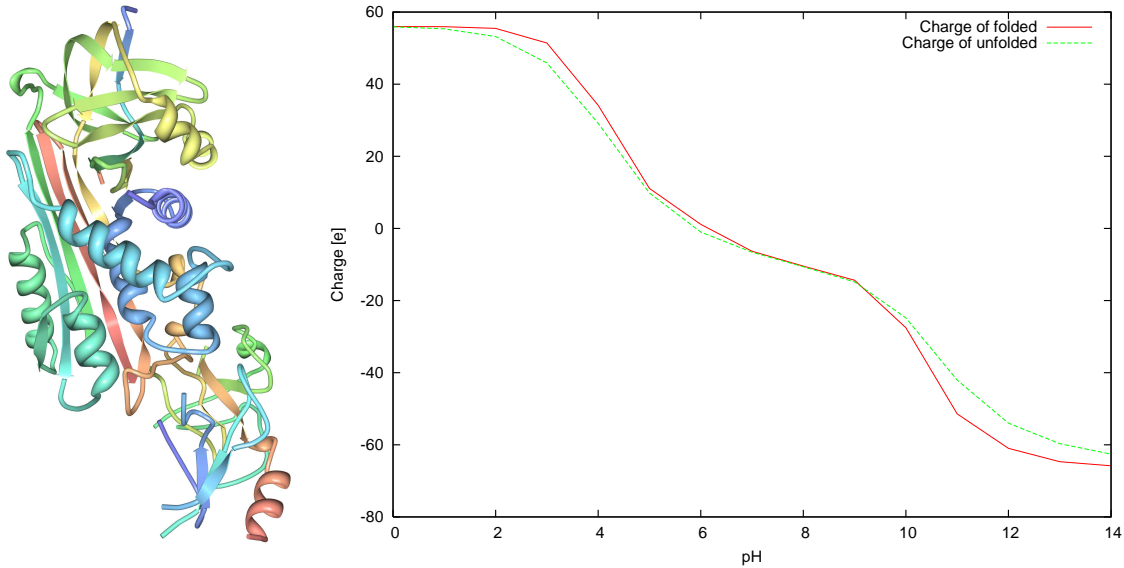


Figure 4.7: Left: Structure of protein 1EZX from the protein database (<http://www.pdb.org/pdb/explore/explore.do?pdbId=1ezx>) with primary citation (Huntington et al., 2000). Right: Charge of protein 1EZX calculated by PROPKA (<http://propka.ki.ku.dk/>) (see Section 1.4.2.3).

distributed, with distance l away from the nanowire surface, we can use the sensitivity factor

$$\Gamma_l \approx 2 \frac{R}{R+l} \left(1 + \sqrt{\frac{R}{R+l}} \exp\left(\frac{l}{\lambda_D}\right) \right)^{-1} \quad (4.7)$$

for a radial nanowire with radius R (Sørensen et al., 2007). This model has been used for the simulation of NWFET sensors in (De Vico et al., 2011). In our case of a rectangular nanowire we get the factor

$$\Gamma_l \approx 2 \left(1 + \exp\left(\frac{l}{\lambda_D}\right) \right)^{-1} \quad (4.8)$$

for the Debye screening. For antibody-antigen sensors this value is $\approx 50\%$ for C-termini functionalized antibodies and $\approx 65\%$ using N-terminal functionalization (Vacic et al., 2011).

4.2.2 Simulator Calibration

The basic geometry for the simulations in Section 4.2.2 and in Section 4.2.3, unless otherwise stated, is depicted in Fig. 4.8. The length of the nanowire is 1000 nm, the doping concentration is -10^{16} cm^{-3} and the source voltage is $V_S = -0.2$.

Since the geometry is fixed, we can calibrate our simulator to measured current-voltage characteristics by only changing the electron and hole mobilities and the thermal voltage. This is physically justified because small silicon nanowires are not expected to have bulk properties, e.g., due to surface-roughness effects.

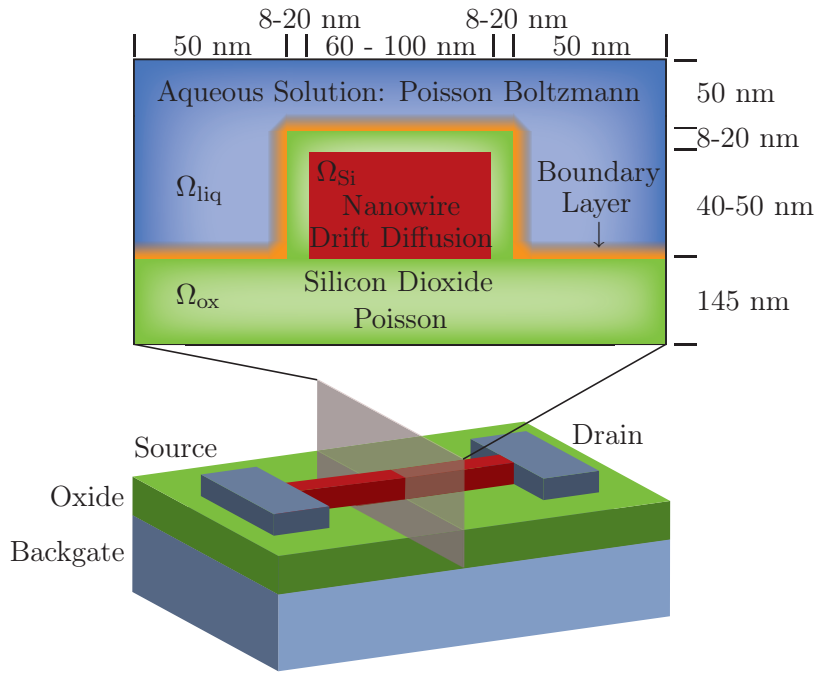


Figure 4.8: Schematic diagram of the NWFET-PSA sensor.

Again we use current-voltage characteristics as the basis for the calibration of our simulator. In the case of the DNA sensor not all geometries were known. Due to the many adjustable parameters it was difficult to find the right physical properties of the DNA sensor. Now, for the PSA sensor nearly all geometries are known; only the thickness of the silicon can vary between 40 nm and 50 nm and the thickness of the silicon dioxide can vary between 8 nm and 20 nm. Once we have fixed the geometry two physical parameters are left to adjust: the mobility (only the mobility of the majority charge carrier is important) and the thermal voltage. The adjusted parameters used in Fig. 4.9 are given in Table 4.1. The best agreement was found for a NWFET device with

	Top Oxide	Nanowire Thickness	Hole Mobility	Thermal Voltage
Top Left	8 nm	50 nm	$100 \text{ cm}^{-2}\text{V}^{-1}\text{s}^{-1}$	0.021 V
Top Right	14 nm	50 nm	$50 \text{ cm}^{-2}\text{V}^{-1}\text{s}^{-1}$	0.023 V
Bottom Left	8 nm	40 nm	$220 \text{ cm}^{-2}\text{V}^{-1}\text{s}^{-1}$	0.021 V
Bottom Right	14 nm	40 nm	$50 \text{ cm}^{-2}\text{V}^{-1}\text{s}^{-1}$	0.023 V

Table 4.1: Parameters used in Fig. 4.9.

8 nm top oxide and a 50 nm thick nanowire as depicted in the top left of Fig. 4.9. Here we used a hole mobility of $100 \text{ cm}^{-2}\text{V}^{-1}\text{s}^{-1}$ and a thermal voltage of 0.021 V. We compared the simulation results to measured current-voltage characteristics for a sensor with a 60 nm and 100 nm wide nanowire. The other simulations are calibrated to the current-voltage characteristic of the device with a 100 nm nanowire but the agreement of the corresponding current-voltage characteristic of a device with the same physical properties with a 60 nm wide nanowire is comparatively bad. We can further validate our calibration by comparison of the sensitivity of such devices with simulations which is shown in Section 4.2.3.

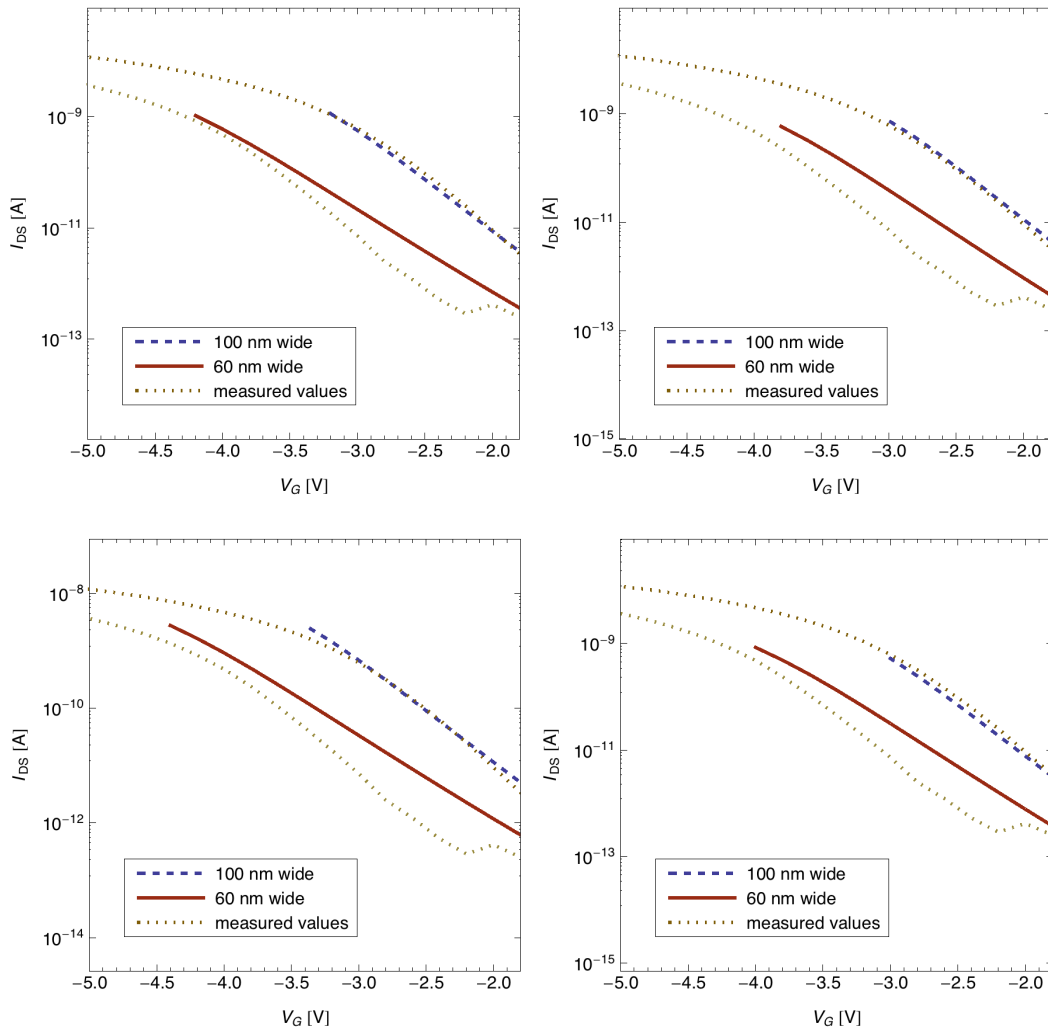


Figure 4.9: Top left: Current-Voltage characteristic for an NWFET device with a 60 nm and a 100 nm wide nanowire with 8 nm top oxide and 50 nm high silicon. The hole mobility is $100 \text{ cm}^2\text{V}^{-1}\text{s}^{-1}$ and the thermal voltage is 0.021 V.

Top right: Current-Voltage characteristic for an NWFET device with a 60 nm and a 100 nm wide nanowire with 14 nm top oxide and 50 nm high silicon. The hole mobility is $50 \text{ cm}^2\text{V}^{-1}\text{s}^{-1}$ and the thermal voltage is 0.023 V.

Bottom left: Current-Voltage characteristic for an NWFET device with a 60 nm and a 100 nm wide nanowire with 8 nm top oxide and 40 nm high silicon. The hole mobility is $220 \text{ cm}^2\text{V}^{-1}\text{s}^{-1}$ and the thermal voltage is 0.021 V.

Bottom right: Current-Voltage characteristic for an NWFET device with a 60 nm and a 100 nm wide nanowire with 14 nm top oxide and 40 nm high silicon. The hole mobility is $50 \text{ cm}^2\text{V}^{-1}\text{s}^{-1}$ and the thermal voltage is 0.023 V.

4.2.3 Sensitivity

If our model is correct, we should have the same increase or decrease of sensitivity when changing device properties. Now we look at the sensitivity of the devices simulated in Fig. 4.9 with the parameters of Table 4.1 for different surface charges. As expected, the best result for sensitivity is achieved with the best result of the current-voltage characteristics. The devices with 14 nm oxide on top have the same decrease when changing from 60 nm wide nanowires to 100 nm wide nanowires, but then the surface charge is higher than the unscreened surface charge of PSA. Hence this cannot be a realistic oxide thickness. For the devices with 8 nm top oxide and a 40 nm thick nanowire the decrease is not realistic and the value for 60 nm wide nanowires is too high.

Hence we will restrict ourselves to the device with 8 nm top oxide, 50 nm thickness of the nanowire, a doping concentration of $100 \text{ cm}^{-2} \text{ V}^{-1} \text{ s}^{-1}$, and a thermal voltage of 0.021 V for which we have the same decrease and correct values for sensitivity for a surface charge of $\gamma = -0.76 \text{ nm}^{-2}$. In the following we observe how the sensitivity is influenced by different physical and geometrical properties.

As aforementioned, the chosen nanowire devices are 60 nm and 100 nm wide and 50 nm high. So one can ask if we can improve the sensitivity by changing the thickness of the nanowire. We cannot compare this to the results depicted in the figures at the bottom of Fig. 4.10 since there a different mobility and a different thermal voltage are used. Changing the thickness of the nanowire shows that the sensitivity depends on both, the thickness and the wideness as seen in the top left of Fig. 4.11. Both nanowire devices show that sensitivity decreases when the thickness becomes too small. Furthermore the sensitivity is improved when we use thicker nanowires except the case in which the gate voltage is too low. But a low gate voltage does not necessarily decrease the sensitivity. In the case of narrow nanowires, we obtain that a low gate voltage increases the sensitivity (see top right of Fig. 4.11). The charge of the PSA oligomer is assumed to be homogeneously distributed and of course devices with 20 nm wide nanowires would have some drawbacks, e.g., problems with the functionalization.

The nanowire length seems to have only a minor influence on the sensitivity. However a small increase is obtained when changing to longer nanowires as depicted in the bottom left of Fig. 4.11. The doping concentration affects the sensitivity only when the doping concentration is chosen to be high (see bottom right of Fig. 4.11). Here we see again a correlation between the decrease of the sensitivity and the magnitude of the gate voltage.

In Fig. 4.12, it becomes obvious that the crucial influence on sensitivity is the gate voltage. Whenever a property is changed such that the gate voltage has more control over the nanowire than the surface charge, the sensitivity decreases. Hence we have decreasing sensitivity for a thicker top oxide and a thinner bulk oxide (top of Fig. 4.12) especially in the case of high negative gate voltage (see also bottom left of Fig. 4.12). However, not every applied voltage to the device turns out to decrease the sensitivity. In the case of the source voltage the sensitivity seems to remain at a certain value as depicted at the bottom right of Fig. 4.12.

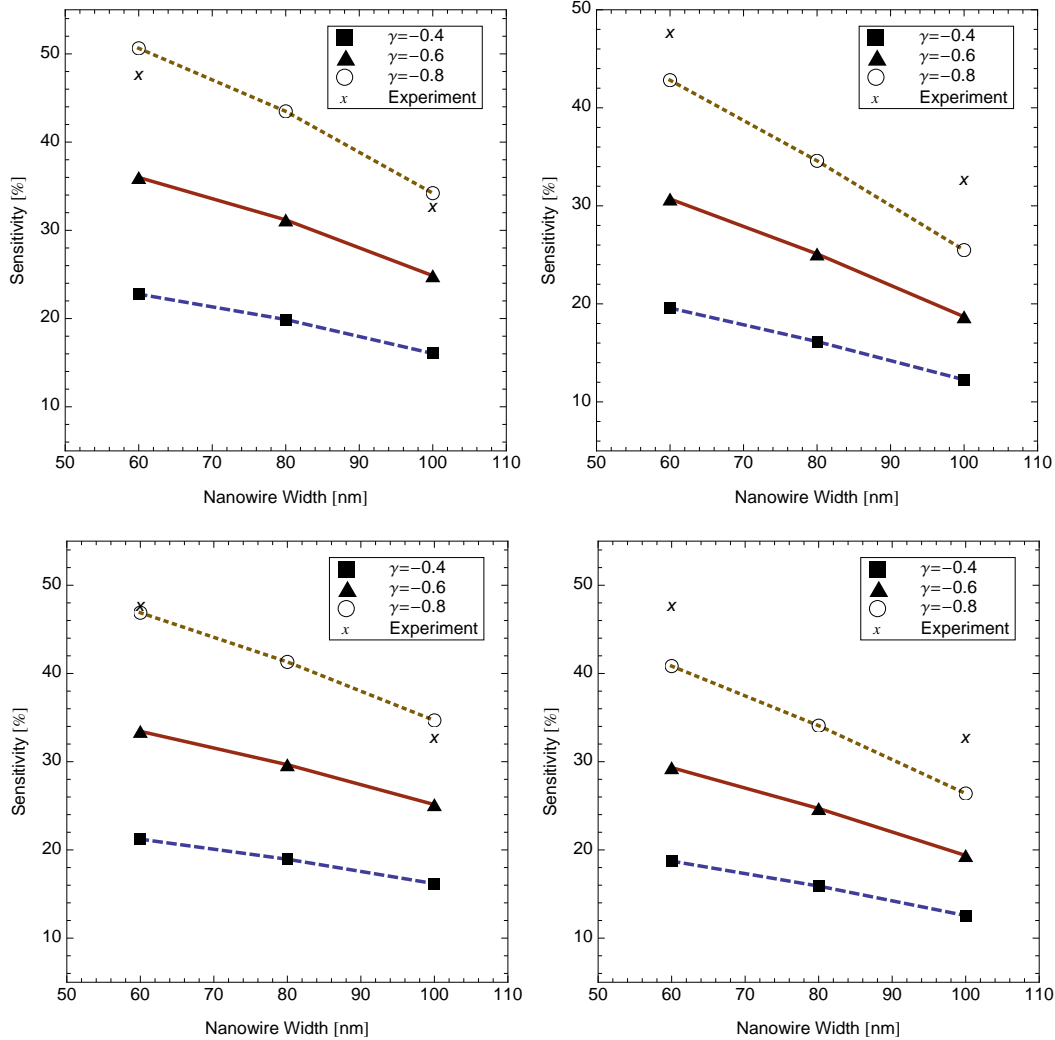


Figure 4.10: All subfigures: The sensitivity is shown for 60 nm, 80 nm, and 100 nm wide nanowires with surface charge $\gamma = -0.4 \text{ q} \cdot \text{nm}^{-2}$, $\gamma = -0.6 \text{ q} \cdot \text{nm}^{-2}$, and $\gamma = -0.8 \text{ q} \cdot \text{nm}^{-2}$. Measured values from an experiment are shown as well.

Top left: Sensitivity of a sensor with the same configuration used in the top left of Fig. 4.9.

Top right: Sensitivity of a sensor with the same configuration used in the top right of Fig. 4.9.

Bottom left: Sensitivity of a sensor with the same configuration used in the bottom left of Fig. 4.9.

Bottom right: Sensitivity of a sensor with the same configuration used in the bottom right of Fig. 4.9.

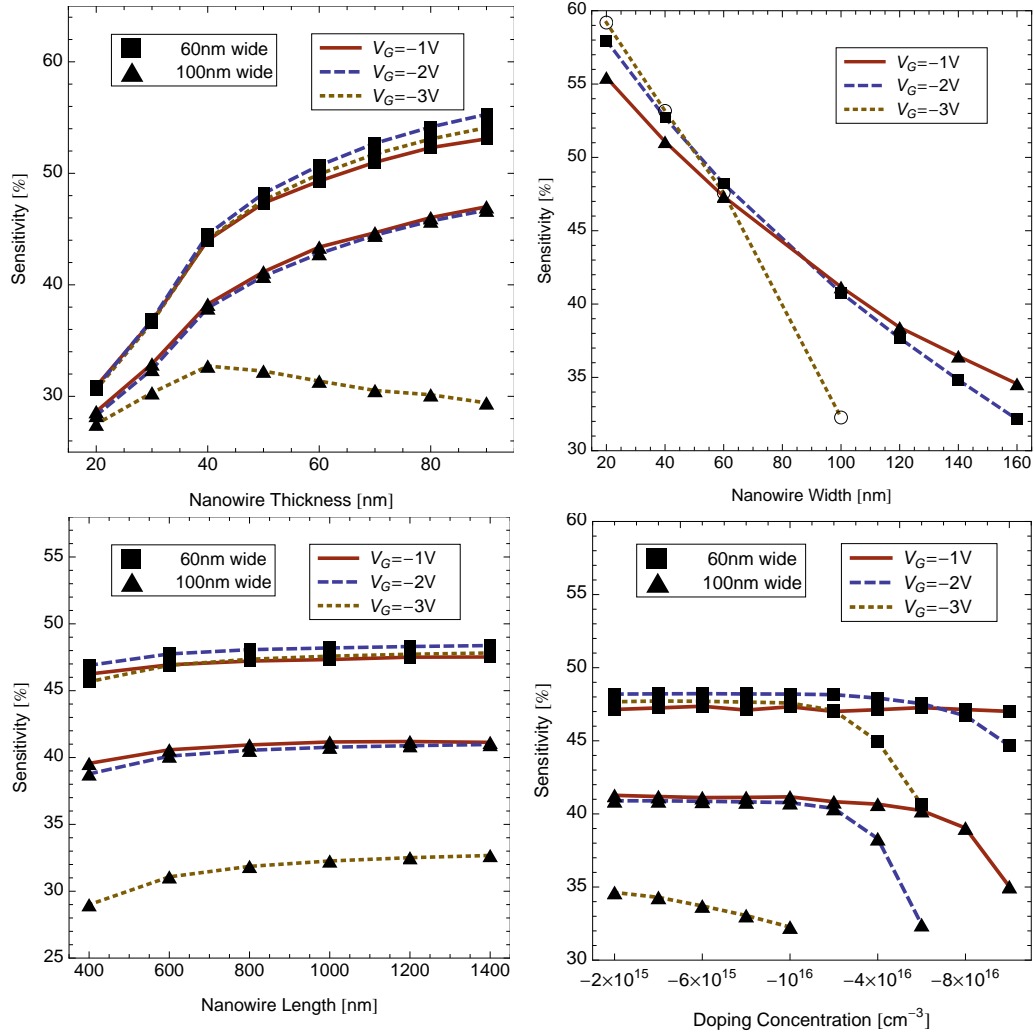


Figure 4.11: Top left: Sensitivity as a function of nanowire thickness for a 60 nm and 100 nm wide nanowire and gate voltages $V_G = -1$ V, $V_G = -2$ V, and $V_G = -3$ V.

Top right: Sensitivity as a function of nanowire width for a sensor with gate voltages of $V_G = -1$ V, $V_G = -2$ V, and $V_G = -3$ V.

Bottom left: Sensitivity as a function of nanowire length for a 60 nm and 100 nm wide nanowire and gate voltages $V_G = -1$ V, $V_G = -2$ V, and $V_G = -3$ V.

Bottom right: Sensitivity as a function of doping concentration for a 60 nm and 100 nm wide nanowire and gate voltages $V_G = -1$ V, $V_G = -2$ V, and $V_G = -3$ V.

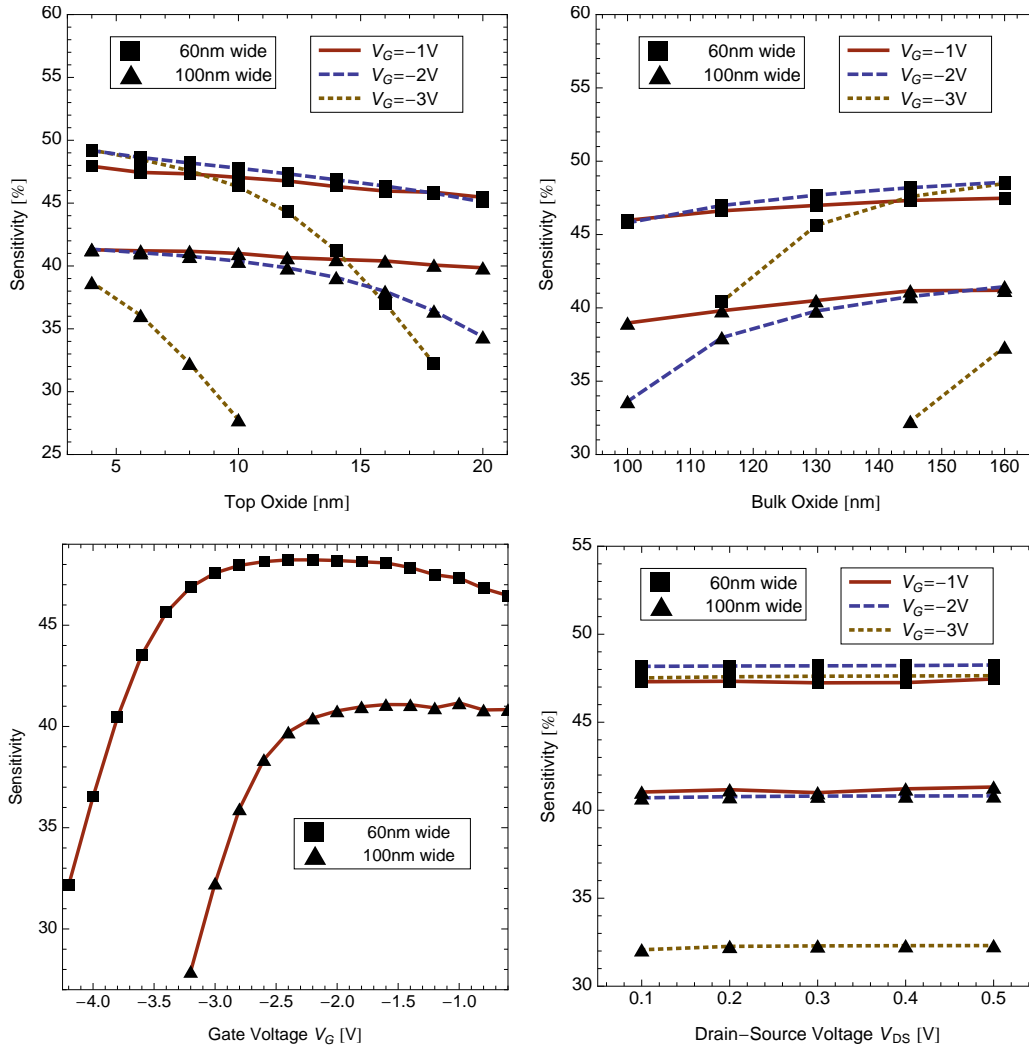


Figure 4.12: Top left: Sensitivity as a function of top oxide for a 60 nm and 100 nm wide nanowire and gate voltages $V_G = -1V$, $V_G = -2V$, and $V_G = -3V$.

Top right: Sensitivity as a function of bulk oxide for a 60 nm and 100 nm wide nanowire and gate voltages $V_G = -1V$, $V_G = -2V$, and $V_G = -3V$.

Bottom left: Sensitivity as a function of gate voltage for a 60 nm and 100 nm wide nanowire.

Bottom right: Sensitivity as a function of drain-source voltage for a 60 nm and 100 nm wide nanowire and gate voltages $V_G = -1V$, $V_G = -2V$, and $V_G = -3V$.

4.3 Summary

In summary, the self-consistent 3d PDE model can reproduce experimental current-voltage characteristics very well. The charge concentration in the surface layer which contains the receptor and target molecules is calculated by a Monte-Carlo algorithm for the DNA sensor and by the PROPKA algorithm for the PSA sensor. A precise theoretical treatment of this surface layer is important, since the free ions in the liquid screen the partial charges of the target molecules in the surface layer. The screening is inherently included in the MMC algorithm and a simple screening model is used for the PROPKA simulator. The model contains no fitting parameter.

We have also performed simulations in order to investigate different device designs regarding maximum sensitivity. Parameters such as the length and thickness of the nanowire transducer, the back-gate voltage, and the doping concentration were investigated for different states of the DNA sensor (non-functionalized, ssDNA, and dsDNA).

Additional informations from experiments are given for the PSA sensor. Again, physical and design properties are studied on their influence on sensitivity.

Optimal device parameters could be identified in all cases. In the simulations of both devices the sensitivity depends strongly on the backgate voltage. The geometry is influencing the sensitivity by the width and the height of the nanowire while the length plays only a minor role.

Chapter 5

Conclusion

THE AIM of this thesis was to describe NWFET sensors by a system of partial differential equations and to develop a 3d parallel simulation code. The system consists of the drift-diffusion-Poisson system, a Poisson-Boltzmann model, and a homogenization method leading to discontinuities (jump conditions) at the sensor surface. These jump conditions describe the surface charge and the dipole moment at the nanowire surface. Hence we can use different boundary layer models for the molecules attached at the surface and the screening from ions in the aqueous solution. Three models are recommended, namely Monte-Carlo simulations, Poisson-Boltzmann calculations, and empirically determined computations.

We have proved that under reasonable assumptions on the jump conditions a solution for our system describing NWFET sensors exists and is locally unique around thermal equilibrium. The proof is based on Schauder fixed-point theorem and the inverse function theorem.

Based on these results we started to discretize the system of PDEs and found that parallelization with the FETI method is the best way to include the jump conditions of the homogenization method. The FETI algorithm has been derived and examples for the correctness of it have been demonstrated. This algorithm is applicable to all semiconducting devices described by the drift-diffusion-Poisson system.

Finally we simulated real devices where we adjusted, without fitting parameters, our model to measured current-voltage characteristics. To investigate the best sensitivity of these devices we used Monte-Carlo simulations and the PROPKA algorithm determining the surface charge and the dipole moment which in turn change the current through the device.

Summarized, we fully investigated a new 3d PDE model for nanowire field-effect biosensors regarding analytical and numerical questions. Furthermore we developed the simulation capability to achieve quantitative understanding of the sensing mechanism of NWFET devices including all necessary geometric and physical properties.

Appendix A

Sobolev Spaces

In the following we give the definitions of the Lebesgue spaces L^p and of the Sobolev spaces H^k . The domain Ω denotes a subset of \mathbb{R}^d . We refer to (Adams, 1975; Grisvard, 1985; Kufner et al., 1977) for details.

Definition A.1 (\mathcal{L}^p spaces). *The \mathcal{L}^p spaces are defined as*

$$\mathcal{L}^p(\Omega) := \left\{ f : \Omega \rightarrow \mathbb{R} : f \text{ Lebesgue measurable, } \int_{\Omega} |f|^p dx < \infty \right\}$$

with norm

$$\|f\|_{\mathcal{L}^p} := \left(\int_{\Omega} |f|^p dx \right)^{1/p}$$

and the \mathcal{L}^∞ space is defined as

$$\mathcal{L}^\infty(\Omega) := \left\{ f : \Omega \rightarrow \mathbb{R} : f \text{ Lebesgue measurable, } \exists \text{ null set } N : f|_{\Omega \setminus N} \text{ is bounded} \right\}$$

with norm

$$\|f\|_{\mathcal{L}^\infty} := \inf_{\text{null sets } N} \sup_{x \in \Omega \setminus N} |f(x)|.$$

The L^p spaces are then the sets of equivalence classes $L^p := \mathcal{L}^p/N$ where N is the kernel regarding $\|\cdot\|_{\mathcal{L}^p}$.

By using a multi-index α with $\alpha = (\alpha_1, \dots, \alpha_d)$ and $|\alpha| = \sum_{i=1}^d \alpha_i$ the partial differentiation of order $|\alpha|$ is defined as

$$D^\alpha u = \frac{\partial^{|\alpha|} u}{\partial x_1^{\alpha_1} \cdots \partial x_d^{\alpha_d}}. \quad (\text{A.1})$$

Definition A.2 (Weak derivative). *Let α be a multi-index and $u \in L^2(\Omega)$. Then $g \in L^2(\Omega)$ is called the weak derivative of u if*

$$\int_{\Omega} g \phi \, dx = (-1)^{|\alpha|} \int_{\Omega} u D^\alpha \phi \, dx, \quad \forall \phi \in \mathcal{D}(\Omega)$$

where

$$\mathcal{D}(\Omega) = \{\phi \in C^\infty(\Omega) : \text{supp}(\phi) \subset \Omega \text{ is compact}\}$$

is the space of test functions. The weak derivative g is called $D^\alpha u$ in the following.

With the weak derivative we can now define the Sobolev spaces.

Definition A.3 (Sobolev spaces). *The space of k -times weakly differentiable functions whose weak derivatives are Lebesgue p -integrable are the Sobolev spaces*

$$W^{k,p}(\Omega) = \{u \in L^p(\Omega) : D^\alpha u \in L^p(\Omega) \text{ for } 0 \leq |\alpha| \leq k\}$$

for $1 \leq p \leq \infty$. The corresponding norms are

$$\|u\|_{W^{k,p}(\Omega)} = \left(\sum_{0 \leq |\alpha| \leq k} \|D^\alpha u\|_{L^p(\Omega)}^p \right)^{1/p}, \quad \text{for } 1 \leq p < \infty \text{ and}$$

$$\|u\|_{W^{k,\infty}(\Omega)} = \max_{0 \leq |\alpha| \leq k} \text{ess sup}_{x \in \Omega} |D^\alpha u|.$$

In the case of $p = 2$ we define $H^k(\Omega) := W^{k,2}(\Omega)$.

Until now, k in $W^{k,p}$ has been always an integer. We can also define the spaces $W^{s,p}$ where s is any positive real number.

Definition A.4 (Sobolev spaces of fractional order). *The Sobolev space $W^{s,p}$, where s is any positive, non-integer real number written as $s = k + \sigma$ where k is a positive integer, is defined as*

$$W^{s,p}(\Omega) = \left\{ u \in W^{k,p}(\Omega) : \int_{\mathbb{R}^d} \int_{\mathbb{R}^d} \frac{|D^\alpha u(x) - D^\alpha u(y)|^p}{|x - y|^{d+\sigma p}} \, dx \, dy < \infty \text{ for } \alpha = k \right\}$$

with norm

$$\|u\|_{W^{s,p}(\Omega)} = (\|u\|_{W^{k,p}(\Omega)}^p + \sum_{\alpha=k} \int_{\mathbb{R}^d} \int_{\mathbb{R}^d} \frac{|D^\alpha u(x) - D^\alpha u(y)|^p}{|x - y|^{d+\sigma p}} \, dx \, dy)^{1/p}.$$

Results from Functional Analysis

For completeness, we state the two Schauder-type fixed-point theorems (see, e.g., (Gilbarg and Trudinger, 1977)), a compactness theorem used in Section 2.3, and the implicit-function theorem for Banach spaces used in Section 2.5 here.

Theorem B.1 (Leray-Schauder fixed-point theorem). *Let T be a compact mapping of a Banach space B into itself, and suppose there exists a constant M such that $\|x\|_B \leq M$ holds for all $x \in B$ and $\sigma \in [0, 1]$ satisfying $x = \sigma T(x)$. Then T has a fixed point.*

Theorem B.2 (Schauder fixed-point theorem). *Suppose X is a Banach space and $K \subset X$ is a convex and closed subset of X . Suppose further that $T : K \rightarrow K$ is a continuous map whose image $T(K)$ is precompact. Then T has a fixed point.*

Theorem B.3 (Rellich-Kondrachov compactness theorem). *Assume U is a bounded open subset of \mathbb{R}^d and ∂U is C^1 . Suppose $1 \leq p < d$. Then $W^{1,p}(U)$ is compactly embedded in $L^q(U)$ for each $1 \leq q < (pd)/(d-p)$.*

Theorem B.4 (Implicit-function theorem for Banach spaces). *Let X , Y , and Z be Banach spaces. Let the function $f : X \times Y \rightarrow Z$ be continuously Fréchet differentiable. If $(x_0, y_0) \in X \times Y$, $f(x_0, y_0) = 0$, and the mapping $y \mapsto D_y f(x_0, y_0)(0, y)$ is a Banach space isomorphism from Y into Z , then there exist neighborhoods U of x_0 and V of y_0 and a Fréchet differentiable function $g : U \rightarrow V$ such that $f(x, g(x)) = 0$ and $f(x, y) = 0$ hold if and only if $y = g(x)$ for all $(x, y) \in U \times V$.*

Bibliography

- Adams R. (1975) *Sobolev spaces*. Academic Press, New York.
- Alexov E., Mehler E., Baker N., Baptista A., Huang Y., Milletti F., Nielsen J., Farrell D., Carstensen T., Olsson M., Shen J., Warwicker J., Williams S., and Word J. (2011) Progress in the prediction of pKa values in proteins. *Proteins Struct. Funct. Bioinf.* **97**(12), 3260–3275. <http://dx.doi.org/10.1002/prot.23189>
- Allen M. and Tildesley D. (1987) *Computer Simulation of Liquids*. Oxford, Oxford, New York.
- Avery P., Rebel G., Lesoinne M., and Farhat C. (2004) A numerically scalable dual-primal substructuring method for the solution of contact problems—Part I: the frictionless case. *Comput. Meth. Appl. Mech. Eng.* **193**(23-26), 2403–2426. <http://dx.doi.org/10.1016/j.cma.2004.01.016>
- Baker N., Holst M., and Wang F. (2000) Adaptive multilevel finite element solution of the Poisson–Boltzmann equation II: Refinement at solvent accessible surfaces in biomolecular systems. *J. Comput. Chem.* **21**(15), 1343–1352. [http://dx.doi.org/10.1002/1096-987X\(20001130\)21:15<1343::AID-JCC2>3.0.CO;2-K](http://dx.doi.org/10.1002/1096-987X(20001130)21:15<1343::AID-JCC2>3.0.CO;2-K)
- Bas D., Rogers D., and Jensen J. (2008) Very fast prediction and rationalization of pKa values for protein–ligand complexes. *Proteins Struct. Funct. Bioinf.* **73**(3), 765–783. <http://dx.doi.org/10.1002/prot.22102>
- Bashford D. and Gerwert K. (1992) Electrostatic calculations of the pKa values of ionizable groups in bacteriorhodopsin. *J. Mol. Biol.* **224**(2), 473–486. [http://dx.doi.org/10.1016/0022-2836\(92\)91009-E](http://dx.doi.org/10.1016/0022-2836(92)91009-E)
- Baumgartner S. and Heitzinger C. (2012a) Existence and local uniqueness for 3d self-consistent multiscale models of field-effect sensors. *Commun. Math. Sci.* **10**(2), 693–716.
- Baumgartner S. and Heitzinger C. (2012b) A one-level FETI method for the drift-diffusion-Poisson system with discontinuities at an interface. *Submitted for publication*, pages 1–23.
- Baumgartner S., Vasicek M., Bulyha A., and Heitzinger C. (2011a) Optimization of nanowire DNA sensor sensitivity using self-consistent simulation. *Nanotechnology* **22**(42), 425503/1–8. <http://dx.doi.org/10.1088/0957-4484/22/42/425503>
- Baumgartner S., Vasicek M., and Heitzinger C. (2011b) Analysis of field-effect biosensors using self-consistent 3D drift-diffusion and Monte-Carlo simulations. *Procedia Engineering* **25**, 407–410. <http://dx.doi.org/10.1016/j.proeng.2011.12.101>
- Baumgartner S., Vasicek M., and Heitzinger C. (2011c) Analysis of field-effect biosensors using self-consistent 3D drift-diffusion and Monte-Carlo simulations. In *Proceedings of European Conference Eurosensors XXV 2011, September 4–7*, pages 1275/1–4, Athens, Greece.
- Baumgartner S., Vasicek M., and Heitzinger C. (2012a) Advanced modeling and simulation of nanowire field-effect sensors. *Submitted for publication*, pages 1–6.

- Baumgartner S., Vasicek M., and Heitzinger C. (2012b) Modeling and simulation of nanowire based field-effect biosensors. In G. Korotcenkov, editor, *Chemical Sensors: Simulation and Modeling*, pages 447–469, *At press*.
- Ben Abdallah N., Degond P., Markowich P., and Schmeiser C. (2001) High field approximations of the spherical harmonics expansion model for semiconductors. *Z. Angew. Math. Phys.* **52**(2), 201–230. <http://dx.doi.org/10.1007/PL00001544>
- Ben Abdallah N., Méhats F., and Vauchelet N. (2006) Diffusive transport of partially quantized particles: existence, uniqueness and long-time behaviour. *Proc. Edinburgh Math. Soc. (2)* **49**(3), 513–549. <http://dx.doi.org/10.1017/S0013091504000987>
- Bensoussan A., Lions J., and Papanicolaou G. (1978) *Asymptotic analysis for periodic structures*, volume 5. North Holland.
- Bergveld P. (1970) Development of an ion-sensitive solid-state device for neurophysiological measurements. *IEEE Trans. Biomed. Eng.* **17**(2), 70–71. <http://dx.doi.org/10.1109/TBME.1970.4502688>
- Bergveld P. and Sibbald A. (1988) *Analytical and biomedical applications of ion-selective field-effect transistors*. Elsevier Amsterdam.
- Bhardwaj M., Day D., Farhat C., Lesoinne M., Pierson K., and Rixen D. (1999) Application of the FETI method to ASCII problems: Scalability results on one thousand processors and discussion of highly heterogeneous problems. Technical Report, Sandia National Labs., Albuquerque, NM (US); Sandia National Labs., Livermore, CA (US). <http://dx.doi.org/10.2172/6127>
- Bohr M., Chau R., Ghani T., and Mistry K. (2007) The high-k solution. *IEEE Spectr.* **44**(10), 29–35. <http://dx.doi.org/10.1109/MSPEC.2007.4337663>
- Bousse L., De Rooij N., and Bergveld P. (1983) Operation of chemically sensitive field-effect sensors as a function of the insulator-electrolyte interface. *IEEE Trans. Electron Devices* **30**(10), 1263–1270. <http://dx.doi.org/10.1109/T-ED.1983.21284>
- Brinkman W., Haggan D., and Troutman W. (1997) A history of the invention of the transistor and where it will lead us. *IEEE J. Solid-State Circuits* **32**(12), 1858–1865. <http://dx.doi.org/10.1109/4.643644>
- Brunet E., Maier T., Mutinati G., Steinhauer S., Köck A., Gspan C., and Grogger W. (2012) Comparison of the gas sensing performance of SnO₂ thin film and SnO₂ nanowire sensors. *Sens. Actuators B* **138**(1), 110–118. <http://dx.doi.org/10.1016/j.snb.2012.02.025>
- Buet C. and Dellacherie S. (2010) On the Chang and Cooper scheme applied to a linear Fokker-Planck equation. *Commun. Math. Sci.* **8**(4), 1079–1090.
- Bulyha A. and Heitzinger C. (2011) An algorithm for three-dimensional Monte-Carlo simulation of charge distribution at biofunctionalized surfaces. *Nanoscale* **3**(4), 1608–1617. <http://dx.doi.org/10.1039/c0nr00791a>
- Caffarelli L. and Cabré X. (1995) *Fully nonlinear elliptic equations*. Oxford University Press.

- Chau R., Datta S., Doczy M., Doyle B., Jin B., Kavalieros J., Majumdar A., Metz M., and Radosavljevic M. (2005) Benchmarking nanotechnology for high-performance and low-power logic transistor applications. *IEEE Trans. Nanotechnol.* **4**(2), 153–158. <http://dx.doi.org/10.1109/TNANO.2004.842073>
- Chen R., Bangsaruntip S., Drouvalakis K., Wong Shi Kam N., Shim M., Li Y., Kim W., Utz P., and Dai H. (2003) Noncovalent functionalization of carbon nanotubes for highly specific electronic biosensors. *Proc. Natl. Acad. Sci.* **100**(9), 4984–4989. <http://dx.doi.org/10.1073/pnas.0837064100>
- Chen R., Choi H., Bangsaruntip S., Yenilmez E., Tang X., Wang Q., Chang Y., and Dai H. (2004) An investigation of the mechanisms of electronic sensing of protein adsorption on carbon nanotube devices. *J. Am. Chem. Soc.* **126**(5), 1563–1568. <http://dx.doi.org/10.1021/ja038702m>
- Cherstvy A. (2011) Electrostatic interactions in biological DNA-related systems. *Phys. Chem. Chem. Phys.* **13**(21), 9942–9968. <http://dx.doi.org/10.1039/c0cp02796k>
- Clark L. and Lyons C. (1962) Electrode systems for continuous monitoring in cardiovascular surgery. *Ann. N.Y. Acad. Sci.* **102**(1), 29–45. <http://dx.doi.org/10.1111/j.1749-6632.1962.tb13623.x>
- Cui Y., Duan X., Hu J., and Lieber C. (2000) Doping and electrical transport in silicon nanowires. *J. Phys. Chem. B* **104**(22), 5213–5216. <http://dx.doi.org/10.1021/jp0009305>
- Cui Y., Wei Q., Park H., and Lieber C. (2001) Nanowire nanosensors for highly sensitive and selective detection of biological and chemical species. *Science* **293**(5533), 1289–1292. <http://dx.doi.org/10.1126/science.1062711>
- Cui Y., Zhong Z., Wang D., Wang W., and Lieber C. (2003) High performance silicon nanowire field effect transistors. *Nano Lett.* **3**(2), 149–152. <http://dx.doi.org/10.1021/nl0258751>
- Davis M., Madura J., Luty B., and McCammon J. (1991) Electrostatics and diffusion of molecules in solution: simulations with the University of Houston Brownian dynamics program. *Comput. Phys. Commun.* **62**(2-3), 187–197. [http://dx.doi.org/10.1016/0010-4655\(91\)90094-2](http://dx.doi.org/10.1016/0010-4655(91)90094-2)
- De Vico L., Iversen L., Sørensen M., Brandbyge M., Nygård J., Martinez K., and Jensen J. (2011) Predicting and rationalizing the effect of surface charge distribution and orientation on nano-wire based FET bio-sensors. *Nanoscale* **3**(9), 3635–3640. <http://dx.doi.org/10.1039/c1nr10316d>
- De Vico L., Sørensen M., Iversen L., Rogers D., Sørensen B., Brandbyge M., Nygård J., Martinez K., and Jensen J. (2010) Quantifying signal changes in nano-wire based biosensors. *Nanoscale* **3**(2), 706–717. <http://dx.doi.org/10.1039/c0nr00442a>
- Ding Z. (1996) A proof of the trace theorem of Sobolev spaces on Lipschitz domains. *Proc. Am. Math. Soc.* **124**(2), 591–600. <http://dx.doi.org/10.1090/S0002-9939-96-03132-2>
- Dostál Z., Horák D., and Kučera R. (2006) Total FETI—an easier implementable variant of the FETI method for numerical solution of elliptic PDE. *Commun. Numer. Methods Eng.* **22**(12), 1155–1162. <http://dx.doi.org/10.1002/cnm.881>

- Dureisseix D. and Farhat C. (2001) A numerically scalable domain decomposition method for the solution of frictionless contact problems. *Int. J. Numer. Methods Eng.* **50**(12), 2643–2666. <http://dx.doi.org/10.1002/nme.140>
- Elfström N., Juhasz R., Sychugov I., Engfeldt T., Karlström A., and Linnros J. (2007) Surface charge sensitivity of silicon nanowires: Size dependence. *Nano Lett.* **7**(9), 2608–2612. <http://dx.doi.org/10.1021/nl0709017>
- Elfström N., Karlström A., and Linnros J. (2008) Silicon nanoribbons for electrical detection of biomolecules. *Nano Lett.* **8**(3), 945–949. <http://dx.doi.org/10.1021/nl080094r>
- Elfström N. and Linnros J. (2008) Biomolecule detection using a silicon nanoribbon: accumulation mode versus inversion mode. *Nanotechnology* **19**(23), 235201/1–5. <http://dx.doi.org/10.1088/0957-4484/19/23/235201>
- Farhat C., Avery P., Tezaur R., and Li J. (2005) FETI-DPH: a dual-primal domain decomposition method for acoustic scattering. *J. Comput. Acoust.* **13**(3), 499–524. <http://dx.doi.org/10.1142/S0218396X05002761>
- Farhat C., Lesoinne M., LeTallec P., Pierson K., and Rixen D. (2001) FETI-DP: a dual-primal unified FETI method—part i: A faster alternative to the two-level FETI method. *Int. J. Numer. Methods Eng.* **50**(7), 1523–1544. <http://dx.doi.org/10.1002/nme.76>
- Farhat C. and Roux F. (1991) A method of finite element tearing and interconnecting and its parallel solution algorithm. *Int. J. Numer. Methods Eng.* **32**(6), 1205–1227. <http://dx.doi.org/10.1002/nme.1620320604>
- Fort A., Rocchi S., Serrano-Santos M., Spinicci R., and Vignoli V. (2006) Surface state model for conductance responses during thermal-modulation of SnO₂-based thick film sensors: Part I—model derivation. *IEEE Trans. Instrum. Meas.* **55**(6), 2102–2106. <http://dx.doi.org/10.1109/TIM.2006.887118>
- Gao X., Zheng G., and Lieber C. (2010) Subthreshold regime has the optimal sensitivity for nanowire FET biosensors. *Nano Lett.* **10**(2), 547–552. <http://dx.doi.org/10.1021/nl9034219>
- Ghani N.E. and Masmoudi N. (2010) Diffusion limit of the Vlasov-Poisson-Fokker-Planck system. *Commun. Math. Sci.* **8**(2), 463–479.
- Gilbarg D. and Trudinger N. (1977) *Elliptic partial differential equations of second order*. Springer Berlin.
- Ginet P., Akiyama S., Takama N., Fujita H., and Kim B. (2011) CMOS-compatible fabrication of top-gated field-effect transistor silicon nanowire-based biosensors. *J. Micromech. Microeng.* **21**, 065008/1–7. <http://dx.doi.org/doi:10.1088/0960-1317/21/6/065008>
- Griessler C., Brunet E., Maier T., Steinhauer S., Köck A., Jordi T., Schrank F., and Schrems M. (2011) Tin oxide nanosensors for highly sensitive toxic gas detection and their 3D system integration. *Microelectron. Eng.* **88**, 1779–1781. <http://dx.doi.org/10.1016/j.mee.2011.02.017>
- Grisvard P. (1985) *Elliptic problems in nonsmooth domains*, volume 24. Pitman Advanced Publishing Program, Boston.

- Hahm J. and Lieber C. (2004) Direct ultrasensitive electrical detection of DNA and DNA sequence variations using nanowire nanosensors. *Nano Lett.* **4**(1), 51–54. <http://dx.doi.org/10.1021/nl034853b>
- Harame D., Bousse L., Shott J., and Meindl J. (1987) Ion-sensing devices with silicon nitride and borosilicate glass insulators. *IEEE Trans. Electron Devices* **34**(8), 1700–1707. <http://dx.doi.org/10.1109/T-ED.1987.23140>
- Heitzinger C., Liu Y., Mauser N.J., Ringhofer C., and Dutton R.W. (2010a) Calculation of fluctuations in boundary layers of nanowire field-effect biosensors. *J. Comput. Theor. Nanosci.* **7**(12), 2574–2580. <http://dx.doi.org/10.1166/jctn.2010.1644>
- Heitzinger C., Mauser N., and Ringhofer C. (2010b) Multiscale modeling of planar and nanowire field-effect biosensors. *SIAM J. Appl. Math.* **70**(5), 1634–1654. <http://dx.doi.org/10.1137/080725027>
- Heitzinger C. and Ringhofer C. (2011) A transport equation for confined structures derived from the Boltzmann equation. *Commun. Math. Sci.* **9**(3), 829–857.
- Holst M., Baker N., and Wang F. (2000) Adaptive multilevel finite element solution of the Poisson–Boltzmann equation I: Algorithms and examples. *J. Comput. Chem.* **21**(15), 1319–1342. [http://dx.doi.org/10.1002/1096-987X\(20001130\)21:15<1319::AID-JCC1>3.0.CO;2-8](http://dx.doi.org/10.1002/1096-987X(20001130)21:15<1319::AID-JCC1>3.0.CO;2-8)
- Holst M., McCammon J., Yu Z., Zhou Y., and Zhu Y. (2012) Adaptive finite element modeling techniques for the Poisson-Boltzmann equation. *Commun. Comput. Phys.* **11**(1), 179–214. <http://dx.doi.org/10.4208/cicp.081009.130611a>
- Honig B. and Nicholls A. (1995) Classical electrostatics in biology and chemistry. *Science* **268**(5214), 1144–1149. <http://dx.doi.org/10.1126/science.7761829>
- Huang H., Ong C., Guo J., White T., Tse M., and Tan O. (2010) Pt surface modification of SnO₂ nanorod arrays for CO and H₂ sensors. *Nanoscale* **2**(7), 1203–1207. <http://dx.doi.org/10.1039/c0nr00159g>
- Huntington J., Read R., and Carrell R. (2000) Structure of a serpin–protease complex shows inhibition by deformation. *Nature* **407**(6806), 923–926. <http://dx.doi.org/10.1038/35038119>
- Im W., Beglov D., and Roux B. (1998) Continuum solvation model: computation of electrostatic forces from numerical solutions to the Poisson-Boltzmann equation. *Comput. Phys. Commun.* **111**(1-3), 59–75. [http://dx.doi.org/10.1016/S0010-4655\(98\)00016-2](http://dx.doi.org/10.1016/S0010-4655(98)00016-2)
- Iwai H. (2009) Roadmap for 22 nm and beyond. *Microelectron. Eng.* **86**(7-9), 1520–1528. <http://dx.doi.org/10.1016/j.mee.2009.03.129>
- Janata J. (1994) Historical review. Twenty years of ion-selective field-effect transistors. *Analyst* **119**(11), 2275–2278. <http://dx.doi.org/10.1039/an9941902275>
- Janata J. (2004) Thirty years of CHEMFETs—a personal view. *Electroanal.* **16**(22), 1831–1835. <http://dx.doi.org/10.1002/elan.200403070>

- Jerome J. (1985) Consistency of semiconductor modeling: An existence/stability analysis for the stationary Van Roosbroeck system. *SIAM J. Appl. Math.* **45**, 565–590.
- Kiyohara K. and Asaka K. (2007) Monte Carlo simulation of electrolytes in the constant voltage ensemble. *J. Chem. Phys.* **126**(21), 214704/1–14. <http://dx.doi.org/10.1063/1.2736371>
- Klawonn A. and Rheinbach O. (2010) Highly scalable parallel domain decomposition methods with an application to biomechanics. *Z. Angew. Math. Mech.* **90**(1), 5–32. <http://dx.doi.org/10.1002/zamm.200900329>
- Klawonn A. and Widlund O. (2001) FETI and Neumann-Neumann iterative substructuring methods: connections and new results. *Commun. Pure Appl. Math.* **54**(1), 57–90. [http://dx.doi.org/10.1002/1097-0312\(200101\)54:1<57::AID-CPA3>3.0.CO;2-D](http://dx.doi.org/10.1002/1097-0312(200101)54:1<57::AID-CPA3>3.0.CO;2-D)
- Köck A., Tischner A., Maier T., Kast M., Edtmaier C., Gspan C., and Kothleitner G. (2009) Atmospheric pressure fabrication of SnO₂-nanowires for highly sensitive CO and CH₄ detection. *Sens. Actuators B* **138**(1), 160–167. <http://dx.doi.org/10.1016/j.snb.2009.02.055>
- Kufner A., John O., and Fučík S. (1977) *Function spaces*. Noordhoff International Publishing, Leyden.
- Kukic P. and Nielsen J. (2010) Electrostatics in proteins and protein–ligand complexes. *Future Med. Chem.* **2**(4), 647–666.
- Li H., Robertson A., and Jensen J. (2005) Very fast empirical prediction and rationalization of protein pK_a values. *Proteins Struct. Funct. Bioinf.* **61**(4), 704–721. <http://dx.doi.org/10.1002/prot.20660>
- Li Y., Qian F., Xiang J., and Lieber C. (2006) Nanowire electronic and optoelectronic devices. *Mater. Today* **9**(10), 18–27. [http://dx.doi.org/10.1016/S1369-7021\(06\)71650-9](http://dx.doi.org/10.1016/S1369-7021(06)71650-9)
- Lieber C. (1998) One-dimensional nanostructures: Chemistry, physics & applications. *Solid State Commun.* **107**(11), 607–616. [http://dx.doi.org/10.1016/S0038-1098\(98\)00209-9](http://dx.doi.org/10.1016/S0038-1098(98)00209-9)
- Lu B., Cheng X., Huang J., and McCammon J. (2010a) AFMPB: an adaptive fast multipole Poisson–Boltzmann solver for calculating electrostatics in biomolecular systems. *Comput. Phys. Commun.* **181**(6), 1150–1160. <http://dx.doi.org/10.1016/j.cpc.2010.02.015>
- Lu B., Zhou Y., Holst M., and McCammon J. (2008) Recent progress in numerical methods for the Poisson–Boltzmann equation in biophysical applications. *Commun. Comput. Phys.* **3**(5), 973–1009.
- Lu M., Hsiao C., Lai W., and Yang Y. (2010b) Probing the sensitivity of nanowire-based biosensors using liquid-gating. *Nanotechnology* **21**(42), 425505/1–5. <http://dx.doi.org/10.1088/0957-4484/21/42/425505>
- Markowich P. (1986) *The Stationary Semiconductor Device Equations*. Springer, Wien.
- Markowich P., Ringhofer C., and Schmeiser C. (1990) *Semiconductor Equations*. Springer, Wien.
- Nair P. and Alam M. (2007) Design considerations of silicon nanowire biosensors. *IEEE Trans. Electron Devices* **54**(12), 3400–3408. <http://dx.doi.org/10.1109/TED.2007.909059>

- Nicholls A., Sharp K., and Honig B. (1991) Protein folding and association: insights from the interfacial and thermodynamic properties of hydrocarbons. *Proteins Struct. Funct. Bioinf.* **11**(4), 281–296. <http://dx.doi.org/10.1002/prot.340110407>
- Olsson M., Søndergaard C., Rostkowski M., and Jensen J. (2011) PROPKA3: consistent treatment of internal and surface residues in empirical pKa predictions. *J. Chem. Theory Comput.* **7**(2), 525–537. <http://dx.doi.org/10.1021/ct100578z>
- Palacios T. (2012) Nanowire electronics comes of age. *Nature* **481**(7380), 152–153. <http://dx.doi.org/10.1038/481152a>
- Patolsky F. and Lieber C. (2005) Nanowire nanosensors. *Mater. Today* **8**(4), 20–28. [http://dx.doi.org/10.1016/S1369-7021\(05\)00791-1](http://dx.doi.org/10.1016/S1369-7021(05)00791-1)
- Patolsky F., Timko B., Zheng G., and Lieber C. (2007) Nanowire-based nanoelectronic devices in the life sciences. *MRS Bull.* **32**(2), 142–149. <http://dx.doi.org/10.1557/mrs2007.47>
- Patolsky F., Zheng G., and Lieber C. (2006a) Fabrication of silicon nanowire devices for ultra-sensitive, label-free, real-time detection of biological and chemical species. *Nat. Protoc.* **1**(4), 1711–1724. <http://dx.doi.org/10.1038/nprot.2006.227>
- Patolsky F., Zheng G., and Lieber C. (2006b) Nanowire-based biosensors. *Anal. Chem.* **78**(13), 4260–4269. <http://dx.doi.org/10.1021/ac069419j>
- Patolsky F., Zheng G., and Lieber C. (2006c) Nanowire sensors for medicine and the life sciences. *Nanomed.* **1**(1), 51–65. <http://dx.doi.org/10.2217/17435889.1.1.51>
- Pavliotis G. and Stuart A. (2007) *Multiscale Methods: Averaging and Homogenization*. Springer, Berlin.
- Peterson A., Heaton R., and Georgiadis R. (2001) The effect of surface probe density on DNA hybridization. *Nucleic Acids Res.* **29**(24), 5163–5168. <http://dx.doi.org/10.1093/nar/29.24.5163>
- Poghossian A., Abouzar M., Amberger F., Mayer D., Han Y., Ingebrandt S., Offenhäusser A., and Schöning M. (2007) Field-effect sensors with charged macromolecules: Characterisation by capacitance–voltage, constant-capacitance, impedance spectroscopy and atomic-force microscopy methods. *Biosens. Bioelectron.* **22**(9–10), 2100–2107. <http://dx.doi.org/10.1016/j.bios.2006.09.014>
- Protter M. and Weinberger H. (1967) *Maximum principles in differential equations*. Springer.
- Ringhofer C. and Heitzinger C. (2008) Multi-scale modeling and simulation of field-effect biosensors. *ECS Trans.* **14**(1), 11–19. <http://dx.doi.org/10.1149/1.2956012>
- Rixen D. and Farhat C. (1999) A simple and efficient extension of a class of substructure based preconditioners to heterogeneous structural mechanics problems. *Int. J. Numer. Methods Eng.* **44**(4), 489–516. [http://dx.doi.org/10.1002/\(SICI\)1097-0207\(19990210\)44:4<489::AID-NME514>3.0.CO;2-Z](http://dx.doi.org/10.1002/(SICI)1097-0207(19990210)44:4<489::AID-NME514>3.0.CO;2-Z)
- Rostkowski M., Olsson M., Søndergaard C., and Jensen J. (2011) Graphical analysis of pH-dependent properties of proteins predicted using PROPKA. *BMC Struct. Biol.* **11**(6), 1–6. <http://dx.doi.org/10.1186/1472-6807-11-6>

- Scharfetter D. and Gummel H. (1969) Large-signal analysis of a silicon read diode oscillator. *IEEE Trans. Electron Devices* **16**(1), 64–77. <http://dx.doi.org/10.1109/T-ED.1969.16566>
- Schöning M. and Poghossian A. (2002) Recent advances in biologically sensitive field-effect transistors (BioFETs). *Analyst* **127**(9), 1137–1151. <http://dx.doi.org/10.1039/b204444g>
- Schöning M. and Poghossian A. (2006) Bio FEDs (field-effect devices): State-of-the-art and new directions. *Electroanal.* **18**(19–20), 1893–1900. <http://dx.doi.org/10.1002/elan.200603609>
- Selberherr S. (1984) *Analysis and Simulation of Semiconductor Devices*. Springer, Wien–New York.
- Søndergaard C., Olsson M., Rostkowski M., and Jensen J. (2011) Improved treatment of ligands and coupling effects in empirical calculation and rationalization of pKa values. *J. Chem. Theory Comput.* **7**(7), 2284–2295. <http://dx.doi.org/10.1021/ct200133y>
- Sørensen M., Mortensen N., and Brandbyge M. (2007) Screening model for nanowire surface-charge sensors in liquid. *Appl. Phys. Lett.* **91**(10), 102105/1–3. <http://dx.doi.org/10.1063/1.2779930>
- Sorgenfrei S., Chiu C., Gonzalez Jr R., Yu Y., Kim P., Nuckolls C., and Shepard K. (2011) Label-free single-molecule detection of DNA-hybridization kinetics with a carbon nanotube field-effect transistor. *Nat. Nanotechnol.* **6**(2), 126–132. <http://dx.doi.org/10.1038/nnano.2010.275>
- Stern E., Klemic J., Routenberg D., Wyrembak P., Turner-Evans D., Hamilton A., LaVan D., Fahmy T., and Reed M. (2007a) Label-free immunodetection with CMOS-compatible semiconducting nanowires. *Nature* **445**(7127), 519–522. <http://dx.doi.org/10.1038/nature05498>
- Stern E., Routenberg D., Vacic A., Rajan N., Criscione J., Park J., Fahmy T., and Reed M. (2011) CMOS compatible nanowires for biosensing. In *Proceedings of the 48th Design Automation Conference*, pages 718–722, ACM. <http://dx.doi.org/10.1145/2024724.2024886>
- Stern E., Steenblock E., Reed M., and Fahmy T. (2008) Label-free electronic detection of the antigen-specific T-cell immune response. *Nano Lett.* **8**(10), 3310–3314. <http://dx.doi.org/10.1021/nl801693k>
- Stern E., Vacic A., Rajan N., Criscione J., Park J., Ilic B., Mooney D., Reed M., and Fahmy T. (2010) Label-free biomarker detection from whole blood. *Nat. Nanotechnol.* **5**(2), 138–142. <http://dx.doi.org/10.1038/nnano.2009.353>
- Stern E., Wagner R., Sigworth F., Breaker R., Fahmy T., and Reed M. (2007b) Importance of the Debye screening length on nanowire field effect transistor sensors. *Nano Lett.* **7**(11), 3405–3409, doi:10.1021/nl071792z. <http://dx.doi.org/10.1021/nl071792z>
- Talasz A.H., Nemat-Gorgani M., Liu Y., Ståhl P., Dutton R.W., Ronaghi M., and Davis R.W. (2006) Prediction of protein orientation upon immobilization on biological and nonbiological surfaces. *Proc. Natl. Acad. Sci.* **103**(40), 14773–14778. <http://dx.doi.org/10.1073/pnas.0605841103>
- Tian B., Cohen-Karni T., Qing Q., Duan X., Xie P., and Lieber C. (2010) Three-dimensional, flexible nanoscale field-effect transistors as localized bioprobes. *Science* **329**(5993), 830–834. <http://dx.doi.org/10.1126/science.1192033>

- Timko B., Cohen-Karni T., Qing Q., Tian B., and Lieber C. (2010) Design and implementation of functional nanoelectronic interfaces with biomolecules, cells, and tissue using nanowire device arrays. *IEEE Trans. Nanotechnol.* **9**(3), 269–280. <http://dx.doi.org/10.1109/TNANO.2009.2031807>
- Tischner A., Köck A., Maier T., Edtmaier C., Gspan C., and Kothleitner G. (2009) Tin oxide nanocrystalline films and nanowires for gas sensing applications. *Microelectron. Eng.* **86**(4-6), 1258–1261. <http://dx.doi.org/10.1016/j.mee.2008.11.084>
- Toselli A. and Klawonn A. (2002) A FETI domain decomposition method for edge element approximations in two dimensions with discontinuous coefficients. *SIAM J. Numer. Anal.* **39**(3), 932–956. <http://dx.doi.org/10.1137/S0036142999361372>
- Toselli A. and Widlund O. (2005) *Domain Decomposition Methods—Algorithms and Theory*, volume 34 of *Springer Series in Computational Mathematics*. Springer Verlag.
- Vacic A., Criscione J.M., Rajan N.K., Stern E., Fahmy T.M., and Reed M.A. (2011) Determination of molecular configuration by debye length modulation. *J. Am. Chem. Soc.* **133**(35), 13886–13889. <http://pubs.acs.org/doi/abs/10.1021/ja205684a>
- Wagner R. and Ellis W. (1964) Vapor-liquid-solid mechanism of single crystal growth. *Appl. Phys. Lett.* **4**(5), 89–90. <http://dx.doi.org/10.1063/1.1753975>
- Wang W., Chen C., Lin K., Fang Y., and Lieber C. (2005) Label-free detection of small-molecule–protein interactions by using nanowire nanosensors. *Proc. Natl. Acad. Sci.* **102**(9), 3208–3212. <http://dx.doi.org/10.1073/pnas.0406368102>
- Xu J., Luo X., and Chen H. (2005) Analytical aspects of FET-based biosensors. *Front. Biosci.* **10**(1), 420–430. <http://dx.doi.org/10.2741/1538>
- Zheng G., Gao X., and Lieber C. (2010) Frequency domain detection of biomolecules using silicon nanowire biosensors. *Nano Lett.* **10**(8), 3179–3183. <http://dx.doi.org/10.1021/nl1020975>
- Zheng G., Patolsky F., Cui Y., Wang W., and Lieber C. (2005) Multiplexed electrical detection of cancer markers with nanowire sensor arrays. *Nat. Biotechnol.* **23**(10), 1294–1301. <http://dx.doi.org/10.1038/nbt1138>
- Zima A., Köck A., and Maier T. (2010) In- and Sb-doped tin oxide nanocrystalline films for selective gas sensing. *Microelectron. Eng.* **87**, 1467–1470. <http://dx.doi.org/10.1016/j.mee.2009.11.103>

Curriculum Vitae

Personal Information

Name Stefan Andreas Baumgartner
Date of Birth April 14th, 1985
Nationality Austria

Education

Since 08/2009 **University of Vienna**
 Doctoral studies in mathematics

10/2005-07/2009 **University of Vienna**
 Diploma studies in mathematics
 Graduation with distinction
 Diploma thesis: Three-Dimensional Modeling of a Nanowire Field-Effect
 Biosensor (BioFET)

09/2004-04/2005 **Compulsory military service**
 'Birago-Kaserne Melk (Pionierbataillon 3)'

09/1999-06/2004 **HTBLuVA St. Pölten**
 Secondary College for Informatics and Business Administration
 Graduation with distinction

Academic employment

- 06/2012-08/2012 **Austrian Institute of Technology**
WWTF (Viennese Science and Technology Fund) project No. MA09-028
- 11/2010 **University of Cambridge**
Internship at the department of applied mathematics and theoretical physics
- 08/2009-05/2012 **Wolfgang Pauli Institute**
PhD program "Differential Equation Models in Science and Engineering"
supported by the Austrian Science Fund
FWF (Austrian Science Fund) project No. P20871-N13

Journal Publications and Book Chapter on Subject of Thesis

- Baumgartner S., Vasicek M., and Heitzinger C. (2012d) Modeling and simulation of nanowire based field-effect biosensors. In G. Korotcenkov, editor, *Chemical Sensors: Simulation and Modeling*, pages 447–469, *At press*.
- Baumgartner S., Vasicek M., and Heitzinger C. (2012c) Advanced modeling and simulation of nanowire field-effect sensors. *Submitted for publication*, pages 1–6.
- Baumgartner S. and Heitzinger C. (2012b) A one-level FETI method for the drift-diffusion-Poisson system with discontinuities at an interface. *Submitted for publication*, pages 1–23.
- Baumgartner S. and Heitzinger C. (2012a) Existence and local uniqueness for 3d self-consistent multiscale models of field-effect sensors. *Commun. Math. Sci.* **10**(2), 693–716.
- Baumgartner S., Vasicek M., and Heitzinger C. (2011b) Analysis of field-effect biosensors using self-consistent 3D drift-diffusion and Monte-Carlo simulations. *Procedia Engineering* **25**, 407–410. <http://dx.doi.org/10.1016/j.proeng.2011.12.101>
- Baumgartner S., Vasicek M., Bulyha A., and Heitzinger C. (2011a) Optimization of nanowire DNA sensor sensitivity using self-consistent simulation. *Nanotechnology* **22**(42), 425503/1–8. <http://dx.doi.org/10.1088/0957-4484/22/42/425503>

Contributions to Conferences and Workshops

- Tulzer G., Baumgartner S., Brunet E., Mutinati G.C., Steinhauer S., Köck A. and Heitzinger C. (2012) Inverse Modeling of CO reactions at SnO₂ nanowire surfaces for selective detection. In *Proceedings of European Conference Eurosensors 2012, September 9–12*, Krakow, Poland.
- Tulzer G., Baumgartner S., Brunet E., Mutinati G.C., Steinhauer S., Köck A. and Heitzinger C. (2012) Inverse Modeling of gas reactions at SnO₂ nanowire surfaces for selective detection. In *Proceedings of Greek Conference Nanotechnology 2012, June 30–July 7*, Thessaloniki, Greece.

Baumgartner S. and Heitzinger C. (2012d) Modeling and simulation of nanowire field-effect transistors. In *Proceedings of German Conference CMAM 2012, July 30–August 3*, Berlin, Germany.

Baumgartner S., Vasicek M., and Heitzinger C. (2012c) Parallel simulation of nanowire field-effect transistors. In *Proceedings of International Conference IWCE 2012, May 22–25*, pages 245–246, Wisconsin-Madison, USA.

Baumgartner S., Vasicek M., and Heitzinger C. (2012b) Self-consistent simulation of nanowire field-effect biosensors. In *Proceedings of Austrian Conference BioNanoMed 2012, March 1–3*, Krems, Austria.

Baumgartner S., Vasicek M., and Heitzinger C. (2012a) Advanced modeling and simulation of nanowire field-effect transistors. In *Proceedings of Austrian Conference Mathmod 2012, February 15–17*, page 56, Vienna, Austria.

Baumgartner S., Vasicek M., and Heitzinger C. (2011b) Analysis of field-effect biosensors using self-consistent 3D drift-diffusion and Monte-Carlo simulations. In *Proceedings of European Conference EuroSensors XXV 2011, September 4–7*, pages 1275/1–4, Athens, Greece.

Baumgartner S., Vasicek M., Bulyha A., Tassotti N., and Heitzinger C. (2011a) Design investigations of nanowire field-effect biosensors using self-consistent 3d drift-diffusion and monte-carlo simulations. In *Proceedings of Greek Conference on Nanosciences & Nanotechnologies 2011, July 12–15*, page 88, Thessaloniki, Greece.

Baumgartner S., Bulyha A., Heitzinger C., and Mauser N.J. (2010) Self-consistent 3D simulations of BioFETs. In *Proceedings of Austrian Conference Nanosens 2010, Dezember 2–3*, Vienna, Austria.

Other Publications

Heitzinger C., Baumgartner S., and Tulzer G. (2012) Mathematische Modelle und Charakterisierung von BioFETs. *VSC Brochure*, page 23.

